# THESIS

**Presented at the University Paul Verlaine of Metz to obtain the title of**
**DOCTOR of University Paul Verlaine of Metz**
Section: **Electronics**

## *Preparation and Characterization of metal oxide semiconductor thin films for the detection of atmospheric pollutant gases*

**By**

## Camelia MATEI GHIMBEU

Sustained in **19th November 2007**, in front of the jury composed of:

| | | |
|---|---|---|
| **M. LUMBRERAS** | Professor at the University Paul Verlaine of Metz | Director |
| **M. SIADAT** | Doctor at the University Paul Verlaine of Metz | Co-Director |
| **N. JAFFREZIC-RENAULT** | Research Director of the CNRS at the University Claude Bernard- Lyon 1 | Reviewer |
| **J. SCHOONMAN** | Professor at the Delft University of Technology (The Netherlands) | Reviewer |
| **J. NICOLAS** | Professor at the University of Liège (Belgium) | Reviewer |
| **D. KOURTICHE** | Professor at the University Henri Poincaré of Nancy | Examiner |

**LASC, 7 Rue Marconi, 57070 Metz**

*Dedic această teză lui Florin, Gabriel şi Cristian*

*Pentru parinţii mei si socrii mei*

# ACKNOWLEDGEMENTS

# TABLE OF CONTENTS

**Table of contents**

**Table of contents**

GENERAL INTRODUCTION

# GENERAL INTRODUCTION

Considering that the atmospheric pollution has increased in the recent years, the detection of harmful and flammable gases is a subject of growing importance in both domestic and industrial environments. The atmospheric pollutants like: $SO_2$, $NO_2$, $O_3$ and particulates matter (PM) have negative effects on human and animal healths. If these pollutants will remain in the same place the problem of the pollution would be easier to solve, but unfortunately, they move hundreds or thousands kilometres from their transmission source inducing as consequence the formation of acid rains, eutrophication and photochemical pollution. All these types of pollutants have a global impact: the greenhouse effect, which is correlated with the global warming, and also the ozone layer (which normally protects us from the UV-rays coming from the sun) destruction.

For human and animal safety and also environmental protection it is necessary to monitor and control such pollutant gases in order to do not exceed a certain admitted concentration in the atmosphere. To replace the heavy, expensive and time consuming analytical systems used to detect pollutant gases, different kind of sensors have been developed, i.e., electrochemical sensors [1] polymer sensors [2], Surface Acoustic Waves (SAW) sensors [3] and Metal Oxide Semiconductor (MOS) sensors [4] etc. The last ones are mainly employed because of their simplicity, small dimensions, good performances and low cost. Unfortunately, they present the disadvantage of a cross-sensitivity for several gases and in addition they work at elevated temperatures. To overcome these problems we have deposited thin films of metal oxide semiconductors (tin oxide, zinc oxide, indium oxide and tungsten oxide) for gas sensor detection. The layers were deposited using a simple and cost-effective deposition technique, i.e., Electrostatic Spray Deposition (ESD) compared with other techniques, which are more or less sophisticated and expensive.

The ESD method was selected for the deposition of the films taking into account the advantages such as: simple and cost-effective set-up, high deposition efficiency, large choice of precursors, and ambient atmosphere operation. Besides, the technique provides an easy control of the surface morphology, from dense to fractal-like porous [5], by varying the deposition parameters such as: temperature, time, flow rate etc. The control of the surface

morphology is of particular interest for gas sensor applications where a porous morphology is desired to increase the adsorption and implicitly the sensor response to a specified gas [6].

The sensor materials are selected according with the literature in order to be sensitive for at least one of the studied gases (hydrogen sulphured ($H_2S$), sulphur dioxide ($SO_2$), and nitrogen dioxide ($NO_2$)). Some of the films are doped with different materials in order to enhance their response to a specified gas. For example, $SnO_2$ is doped with copper oxide in order to increase the $H_2S$ sensitivity while $In_2O_3$ is doped with tin oxide to improve the $NO_2$ response.

After material and dopant selections, the films are deposited on partially Pt-coated alumina varying the deposition parameter. The layer morphology and microstructure are evaluated with different techniques, i.e., Scanning and Transmission Electron Microscopy (SEM and TEM), Energy Dispersive X-ray analysis (EDX), X-ray Diffraction (XRD), and Raman Spectroscopy in order to evaluate the film feature (porosity, adherence, purity, thickness, particle size, defects, of the films). The layer performance in the detection of $H_2S$, $SO_2$, and $NO_2$ are studied as function of the operating temperature and the gas concentration.

This thesis is organized in seven Chapters as follow:

In Chapter I an overview concerning the air pollution is done. The most important pollutant types are described along with their principal negative effects on the environment, people and animal heaths.

Chapter II deals with a brief description of the chemical sensors and their classification. General aspects concerning the gas sensors based on metal oxide semiconductors are more intensively discussed. Hence, the MOS types, the conduction mechanism and the principal factors which affect the MOS performances are presented. The structure of the materials (tin oxide, tungsten oxide, zinc oxide and indium oxide) is also highlighted.

The Chapter III presents the experimental details about the deposition of the films and also the characterization techniques used to study their morphological and their structural properties. The experimental set-up used to deposit the layers and to evaluate the gas sensor performance is described along with the working procedure.

Chapter IV is devoted to the preparation of tin oxide thin films by varying the deposition parameters such as, deposition temperature, time, and flow rate. The film morphology and microstructure is studied with different characterization techniques, in order to find the best process conditions to obtain especially porous films suitable for gas sensor applications. The $SnO_2$ layers are doped with copper oxide and the effect on their morphology, microstructure and the performance in the detection of $H_2S$ are presented in function of the operating temperature and the gas concentration, and the results compared with those obtained for undoped $SnO_2$. The sensor $H_2S$ cross-sensitivity to $SO_2$, and $NO_2$ at the optimum operating temperature is also presented.

In Chapter V the deposition of porous zinc oxide films by varying the flow rate and the deposition time is presented. The film structural and morphological characterization as well as their application as gas sensors for the detection of $H_2S$, $SO_2$, and $NO_2$ are related.

The Chapter VI is dedicated to the preparation of porous indium oxide and Sn-doped-indium oxide films by employing the ESD method, which is a new deposition method for these materials. Different techniques are used to characterize the morphology and the microstructure of the films. The gas sensing performances of undoped $In_2O_3$ and Sn-doped $In_2O_3$ to $H_2S$ detection are presented in function of the temperature and the gas concentration and compared. In addition, the sensor $H_2S$ cross-sensitivity to $SO_2$ and $NO_2$ is highlighted.

In Chapter VII it is presented for the first time the fabrication of porous films of $WO_3$ by changing the deposition parameters with the ESD method. The study of the film morphology and microstructure using different techniques is shown as well. The sensor responses to $H_2S$ and $NO_2$ in function of the operating temperature and the gas concentration is evaluated along with the sensor $H_2S$ cross-sensitivity to $SO_2$ and $NO_2$.
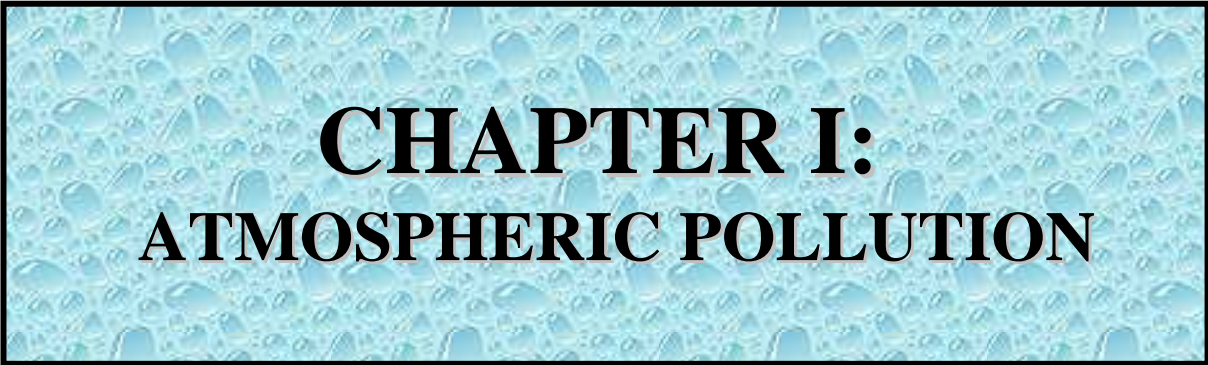
# CHAPTER I:
## ATMOSPHERIC POLLUTION

# I. ATMOSPHERIC POLLUTION

## I.1. INTRODUCTION

On our planet, air is one of the most important natural resources on which all life depends. Over the years, modernisation and progress have led to an increase of air pollution, industries, vehicles and urbanization being the major factors responsible for this. The atmosphere is comprised of permanent gases (which are considered to remain constant) and variable gases (which change their concentrations over a finite period of time). The **permanent** gases of the atmosphere are: Nitrogen ($N_2$, 78.084 %) and Oxygen ($O_2$, 20.9476 %). Other permanent gases are: Argon, Neon, Helium, Krypton, Hydrogen, and Xenon. Among the **variable** gases in the atmosphere we can find: Water vapour (0 to 4%), Carbon Dioxide, Methane and Ozone etc. [7]. The main pollutants which are found in the atmosphere are inorganic and organic pollutants, and suspended particle matter.

Although both nitrogen and oxygen are essential to human life on the planet, they have little effect on the atmospheric processes. The variable components (< 1% of the atmosphere) have a much greater influence on both short-term weather and long-term climate.

The air pollution can be defined as: "the presence in the atmosphere of one or more contaminants in such quantity and for such duration as is injurious to human health or welfare, animal or plant life" [8]. Air pollution can be also caused by factors independent of human control. The most important natural source of air pollution is volcanic activity, which releases great amounts of ashes and toxic fumes into the atmosphere. Dust storms in desert areas and smoke from forest and grass fires contribute also to chemical and particulate pollution of the air.

## I.2.  INORGANIC POLLUTANTS

### I.2.1.  Hydrogen Sulphide (H$_2$S)

$H_2S$ is a colourless gas with odour of rotten eggs at very low concentrations. It occurs **naturally** in crude petroleum, natural gas, in volcanic gases, lake and marine sediments. It is formed also from bacterial breakdown of organic matter containing sulphur, or produced by human and animal wastes. For example, a small amount of hydrogen sulphide is produced by bacteria in our mouth and gastrointestinal tract and by enzymes in our brain and muscles. It is also a by-product of many **industrial** operations, such as petroleum refineries, natural gas plants, Kraft paper mills, iron smelters, food processing plants and tanneries.

### I.2.2.  Nitrogen Oxides (NO$_x$)

Two of the most toxicologically nitrogen oxides are nitrogen monoxide (NO) and nitrogen dioxide ($NO_2$). Both are non-flammable and colourless to brown at room temperature. Nitrogen monoxide is a sharp sweet-smelling gas at room temperature, whereas nitrogen dioxide has a strong, biting odour and it is liquid at room temperature. Nitrogen oxides are released into the atmosphere mainly in the form of NO, which is then oxidised to $NO_2$ by reaction with ozone. It is produced by motor vehicles, power plants, and other industrial, commercial, and residential source burning fuels. Among the oxides of nitrogen involved in air pollution, $NO_2$ is the most important in terms of both health risk and environmental damage.

The annual emission of $NO_2$ in 20 Europeans cities can be seen in Fig I-1.

### I.2.3.  Sulphur Dioxide (SO$_2$)

At room temperature, sulfur dioxide is a nonflammable colourless gas with a very strong pungent odor. It is handled and transported as a liquefied compressed gas. Although sulphur dioxide does not burn in air, cylinders of compressed liquid can explode in the heat of a fire.

Great quantities of $SO_2$ are emitted by **natural** sources such as volcanoes. Sulphur dioxide is formed when fuel-containing sulphur (such as coal and oil) is burned, and when gasoline is extracted from oil, or metals extracted from ore.
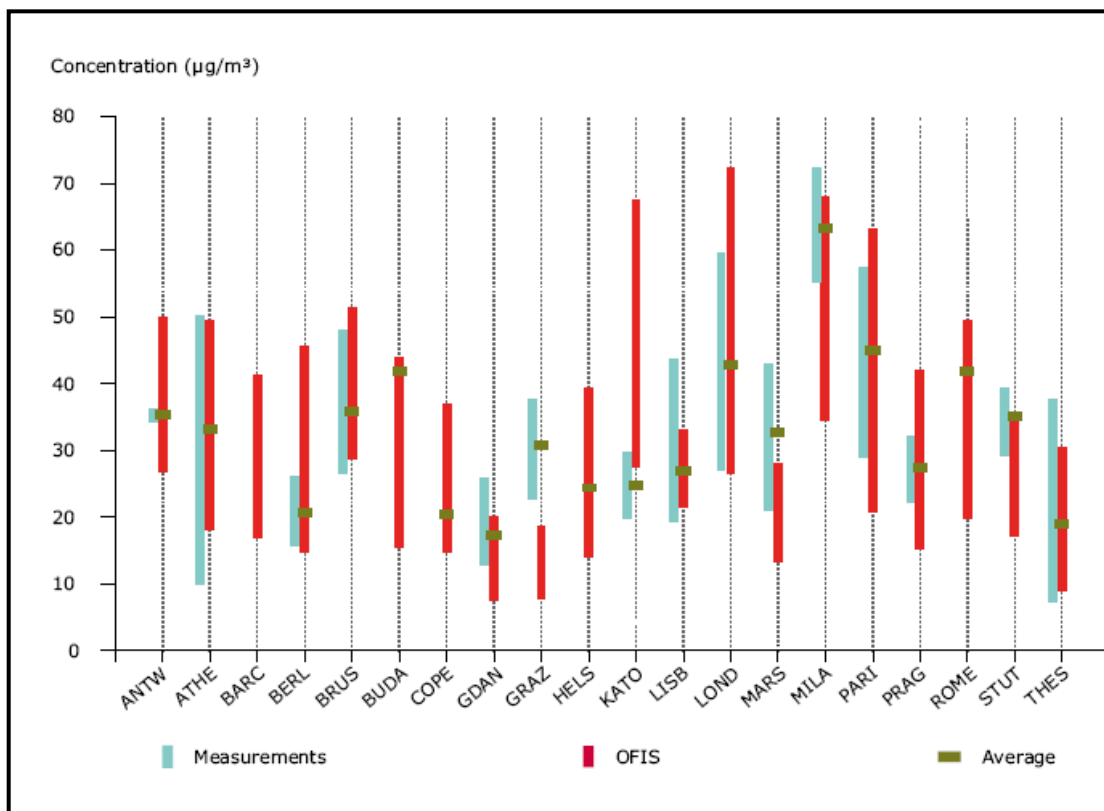
*Figure I-1: Mean annual NO$_2$ urban background concentrations ($\mu g/m^3$) in 20 European cities: the range of OFIS model results from the reference year 2000 compared to the range of observations and average values of all stations [9], (OFIS: represents the Ozone Fine Structure Model).*

## I.2.4. Carbon Oxides (CO$_x$)

**Carbon monoxide (CO)** is a colourless, odourless, tasteless poisonous gas formed when carbon in fuel is not burned completely. It is a component of motor vehicle exhaust, which contributes about 56% of all CO emissions. Other non-road engines and vehicles contribute also to CO emissions. Other sources of CO emissions include **industrial** processes (such as metal processing and chemical manufacturing), residential wood burning, and **natural** sources such as forest fires.

**Carbon dioxide (CO$_2$)** is the principle greenhouse gas emitted as a result of human activities such as the burning of coal, and oil. More details about the greenhouse effect can be found in Part I.6.1.

## I.2.5.  Ozone (O₃)

Ozone is a strong oxidizing gas, which has a bluish colour and a pungent odor.  It is created by the chemical reaction between nitrogen oxides and volatile organic compounds in the presence of sunlight. Ozone has the same chemical structure whether it occurs miles above the earth or at ground level and can be "good" or "bad," depending on its location in the atmosphere.  The "good" ozone occurs naturally in the stratosphere approximately 15 to 45 km above the earth surface and forms a layer, which protects life on earth from the sun harmful rays.  In the earth lower atmosphere, ground-level ozone is considered "bad" being a pollutant.

Motor vehicle exhaust and industrial emissions, gasoline vapours, and chemical solvents, as well as natural sources, emit $NO_x$ and VOCs (Volatile Organic Compounds), which facilitate the formation of ozone. Sunlight and hot weather cause ground-level ozone to form in harmful concentrations in the air.  As a result, it is known as a summertime air pollutant (as shown in Fig. I-2).  The emissions of ozone precursors in 20 European cities can be seen in Fig. I-3.
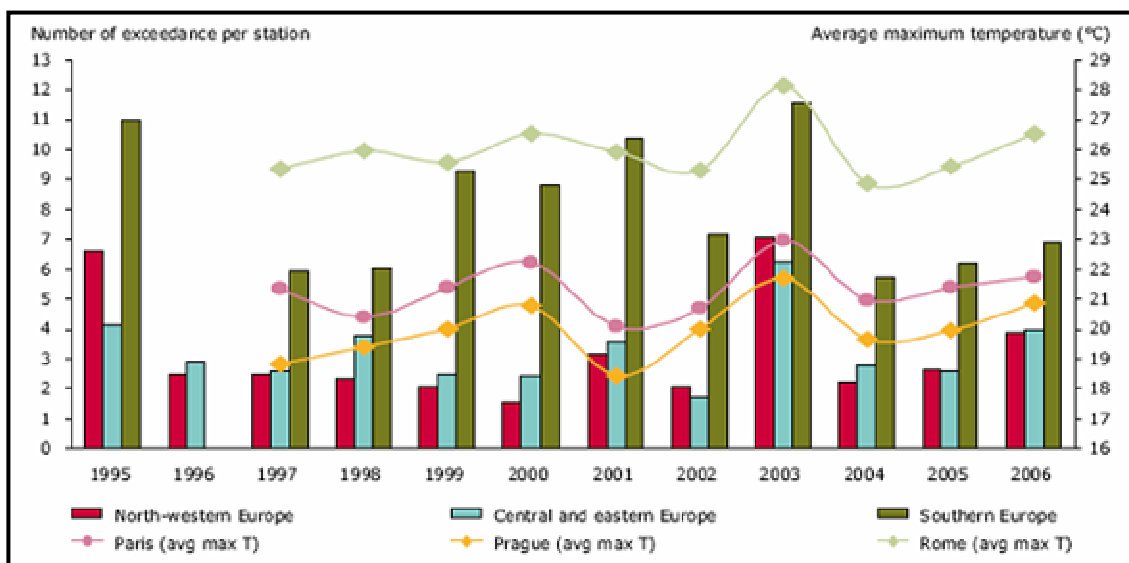


*Figure I-2: Number of exceedances per region for stations, observed during the year, and the summer average maximum daily temperature in selected cities (Paris, Prague and Rome) [10] .*
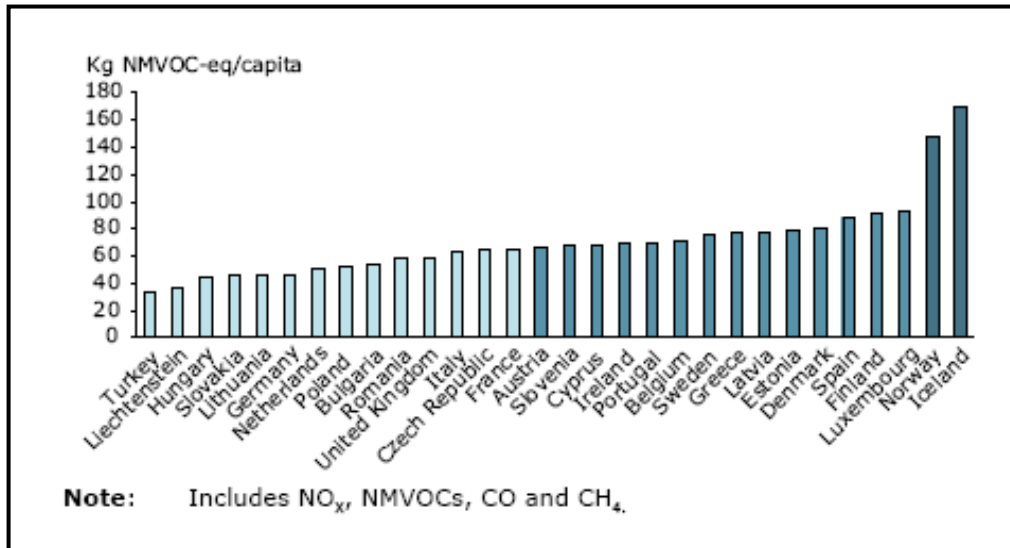
*Figure I-3: Emission of ozone precursors per capital, 2002 [11].*

## I.2.6.  Heavy metals

Particulate metals in air result from activities such as fossil fuel combustion, metal processing industries and waste incineration. The most common metals found in the air are lead and mercury.

*Lead (Pb)* is a metal found naturally in the environment, as well as in manufactured products. The major sources of lead emissions have historically been motor vehicles and industrial sources. Other stationary sources are waste incinerators, utilities, and lead-acid battery manufacturers. The most airborne emissions of lead originate from petrol-engined motor vehicles using petrol (which contain tetraethyl lead) as combustible. With the increasing use of unleaded petrol, however, emissions and concentrations in air have decreased steadily in recent years as shown in Fig. I-4.
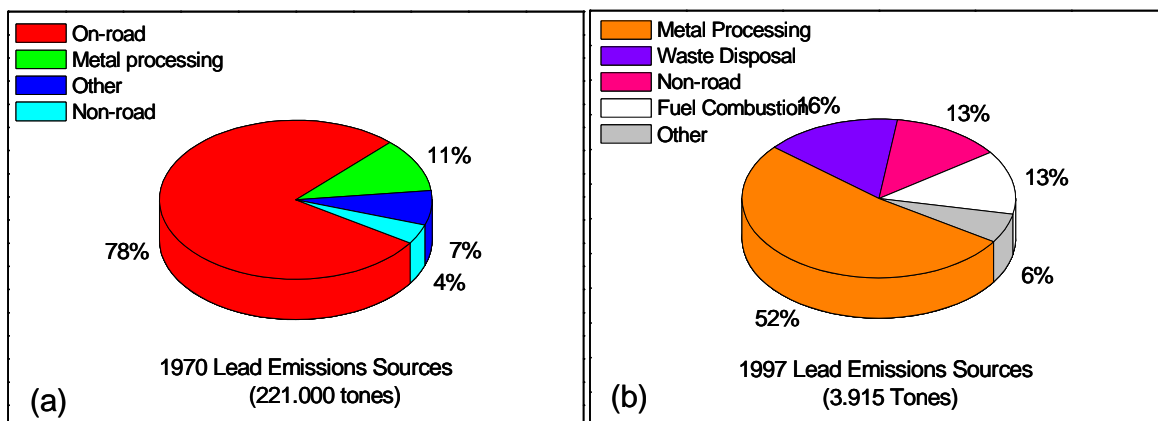


*Figure I-4: Principal Lead Emission Sources in (a) 1970 and (b) 1997 [12].*

*Mercury (Hg)* The atmospheric deposition is the dominant source of mercury, but alkali and metal processing, incineration of coal, medical and other waste are also important sources of Hg. Natural sources of atmospheric mercury include volcanoes, geologic deposits of mercury, and volatilisation from the ocean. *Methyl-mercury* [$CH_3Hg$] is the most toxic chemical form of Hg. *Elemental mercury*, Hg (0) can be found in high concentrations in gold mine sites.

*Other contaminant metals* are Zinc, Iron, Copper, Cadmium, Chromium, Nickel, and Aluminium.

## I.3. ORGANIC POLLUTANTS

There are two main groups of organic pollutants: Volatile Organic Compounds and Polycyclic Aromatic Hydrocarbons (PAHs).

### I.3.1. Volatile Organic Compounds

VOCs are released in vehicle exhaust gases, either as unburned fuels or as combustion products. Benzene and 1,3-butadiene are of particular concern, as they are known carcinogens, but other VOCs (i.e. Chlorofluorocarbons) are important because of their role played in the ozone layer destruction.

*Benzene* is a minor constituent of petrol (2% vol.). The main sources of benzene in the atmosphere are the distribution and combustion of petrol. Benzene is emitted in vehicle exhaust not only as an unburned fuel but also as a product of the decomposition of other aromatic compounds.

*1,3-butadiene* is emitted into the atmosphere principally from fuel combustion of petrol and diesel vehicles. It is produced by the combustion of olefins. 1,3-butadiene is also an important chemical in certain industrial processes, particularly the manufacture of synthetic rubber.

*Chlorofluorocarbons (CFCs)* are gases that are released mainly from air-conditioning systems and refrigeration. When released into the air, CFCs rise to the stratosphere, where they come in contact with few other gases, which leads to a reduction of the ozone layer that protects the Earth from the harmful ultraviolet rays of the sun.

### I.3.2.  Polycyclic Aromatic Hydrocarbons

Polycyclic aromatic hydrocarbons are formed during incomplete combustion or pyrolysis of organic material. The use of oil, gas, coal, and wood in energy production and tobacco smoking are additional contributions to ambient air levels. Food is considered to be the major source of human PAHs exposure, owing to PAHs formation during cooking or from atmospheric deposition of PAHs on grains, fruits and vegetables.

## I.4.  SUSPENDED PARTICULATE MATTER

Suspended particulate matter (SPM) consists of small particles (aerosols) suspended in the air in the form of smoke, dust, and vapour. The particulate matters are divided into fine particles less than 2.5 micrometers in diameter ($PM_{2.5}$), and particles between 2.5 and 10 micrometers in diameter ($PM_{10}$). In Fig. I-5 can be seen the annual $PM_{10}$ emission in 20 cities of Europe. Some particles, known as *primary particles,* are emitted directly from a source, such as construction sites, unpaved roads, fields, smokestacks, dust storms, or fires. Other particles are formed in reactions in the atmosphere with chemicals such as sulphur dioxide and nitrogen oxides. These particles, are known as *secondary particles*, and are predominant among the particle pollution.

## I.5.  INDOOR AIR POLLUTANTS

Many people spend large periods of time indoor, approximately 80-90% of their lives. They work, study, eat, drink, and sleep in enclosed environments, where air circulation may be restricted. For these reasons, some experts think that more people suffer from the effects of indoor air pollution than outdoor pollution. There are many sources of indoor air pollution such as tobacco smoke, cooking and heating appliances, and vapours from building materials, paints, and furniture. Radon is a natural radioactive gas released from the earth, and it can be found concentrated in basements.

## I.5.1. Tobacco smoke

Environmental tobacco smoke (ETS) is a dynamic complex mixture of thousands of harmful compounds in particulate and vapour phases.

## I.5.2. Radon

Exposure to radon is the dominant source of exposure to ionising radiation in most countries. The radon levels vary considerably from one building to another, and depend primarily on the inflow of soil gas and the type of building material.

**Other indoor pollutants**

*Biological pollutants* include pollen from plants, hair from pets, fungi, parasites, and some bacteria. Most of them are allergens and can cause asthma, hay fever, and other allergic diseases. *Formaldehyde* is a gas coming mainly from carpets, particle boards, and insulation foam. It causes irritation to the eyes and nose and may cause allergies in some people.
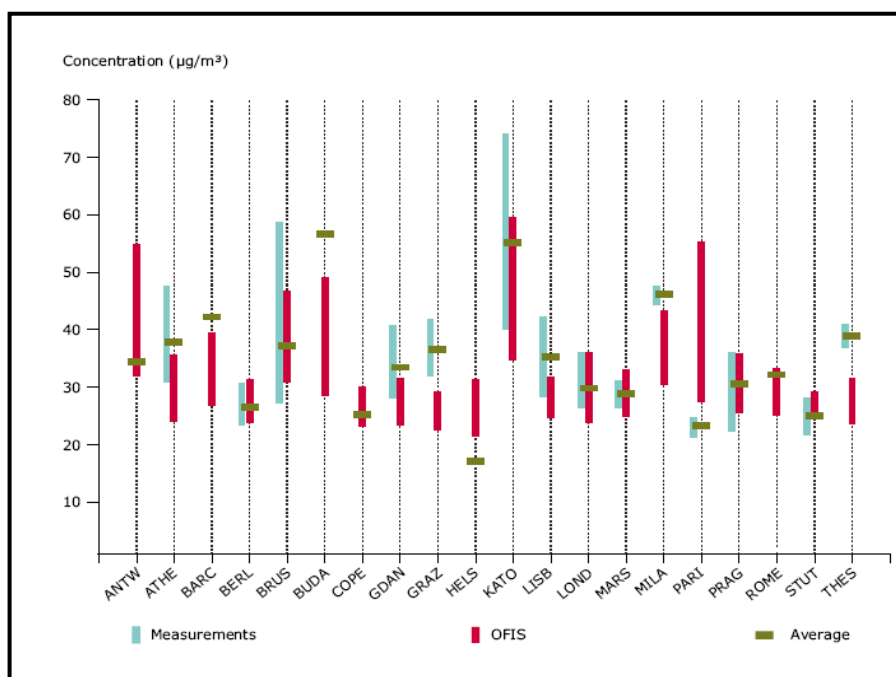


*Figure I-5: Mean annual PM$_{10}$ urban background concentrations ($\mu g/m^3$) in 20 European cities: range of OFIS model results from the reference year 2000 compared to the range of observations and average values of all stations [9].*

## I.6.  HEALTH PROBLEMS CAUSED BY POLLUTION

The pollution has negative effects on the human health and the principal problems triggered are the acute or/and chronic respiratory diseases.

The toxicity of **$H_2S$** is comparable with that of hydrogen cyanide. It forms a complex bond with iron blocking oxygen and stopping cellular respiration. The nervous system is the most affected by $H_2S$ [13]. The threshold-limited value (TLV) for hydrogen sulfide is 10 ppm and for concentrations higher than 250 ppm, it is dangerous to human body resulting in loss of consciousness, permanent brain damage and even death [14,15].

The **$NO_2$** cause eyes, nose, and throat irritations. Long-term exposure to this gas may decrease the lung function and increase the risk of respiratory symptoms, particularly for children. In the air, $NO_x$ reacts readily with common organic chemicals and even ozone, to form a wide variety of toxic products (nitrate radical, nitroarenes, and nitrosamines), which may cause biological mutations.

Exposures to high levels of **$SO_2$** (100 ppm) are causing nose and throat burning, breathing difficulties and airways obstruction. People with asthma are in particularly more susceptible to the effects of $SO_2$.

**CO** can cause harmful health effects by reducing oxygen delivery to the body's organs (like the heart and brain) and tissues. The people who inhale high levels of CO can develop vision problems, reduced ability to work or learn, and reduced dexterity. At extremely high levels, CO is poisonous and can cause death.

The ground-level **$O_3$** triggers a variety of health problems including asthma, reduced lung capacity, and increased susceptibility to respiratory illnesses (pneumonia and bronchitis) [12]. Ozone can irritate lung airways and cause inflammation like sunburn.  Furthermore, it has been found to convert cholesterol in the blood stream to plaque (which causes hardening and narrowing of arteries). This cholesterol product has also been implicated in Alzheimer's disease.

Peoples are mainly exposed to **heavy metals** by breathing and ingesting it in food, water, soil, or dust. They accumulate in the blood, bones, muscles, and fat.
**Pb** causes damage in organs, osteoporosis, and reproductive disorders. Excessive exposure to lead causes mental retardation, behavioural disorders, memory problems, and mood changes. Low levels of lead damage the brain and nerves in foetuses and children, resulting in learning deficits and lowered IQ.

**CH$_3$Hg** affects the immune system, alters genetic and enzyme systems, and damages the nervous system, including coordination and the senses of touch, taste, and sight.

**Hg** causes tremors, gingivitis, and excitability when vapours are inhaled over a long period of time.

In the terms of health risks, the smaller **PM** are most harmful because they can get deep into the lungs, and some may even get into the bloodstream. Other health problems linked to the particle pollution exposure includes: respiratory symptoms, heart attacks, asthma.

The **VOCs** and **PAHs** are known as human carcinogen [16].

**Tobacco smoke** irritates the eyes and respiratory tract and, in children, increases the risk of pneumonia and bronchitis [16]. Chronic exposures to tobacco increase lung cancer mortality. In addition, it increases the risk of morbidity and mortality from cardiovascular disease in non-smokers. In addition, the interaction between the smoke and **radon** exposure with regard to lung cancer has proved to have an almost multiplicative effect [16].

# I.7. ENVIRONMENTAL PROBLEMS CAUSED BY POLLUTION

## I.7.1. Greenhouse effect

The greenhouse effect is a naturally occurring process, heating the earth surface and atmosphere. The long wavelength radiations (IR) emitted from the earth surface are absorbed by the greenhouse gases, i.e., $CO_2$ (82%), $CH_4$ (8%), $N_2O$ (8%), and chlorofluorocarbon gases (2%) and then re-emitted. Without the greenhouse effect, the life on this planet would probably not exist, taking into account that the average temperature of the earth would be -18 °C, rather than 15 °C as it is to date.

Lately, human activity has resulted in a dramatic increase in the concentrations of greenhouse gases in the atmosphere. Since 1900, European annual mean air temperatures have increased by 0.95 °C, and this trend is expected to rise by 2–6 °C in this century. It is generally accepted that high greenhouse gas emissions lead to climate change, e.g., an increase in the global average temperature and sea level rise (due to the melt of icecaps), and a change in the magnitude and frequency of some extreme weather events [17].

The effects of the global warming are terrible to environmental, human health and safety, and economy. Higher temperatures and more intense droughts are producing a rising trend in the number and severity of forest fires in the Mediterranean zone. Changes in rainfall and flows from glaciers are altering river flows, sometimes causing floods or emptying reservoirs. The severe flooding in Austria, the Czech Republic, Germany, Hungary and Slovakia in August 2002 caused economic losses of about EUR 25 billions [18].

Higher summer temperatures are intensifying photochemical smog, raising ozone concentrations, and increase the incidence of a wide range of diseases, from allergies to asthma attacks. Potential malaria risk areas also increase.

High temperatures are a threat not only to the human health but also to the human being's life. In the 2003 heat wave, 20 000 people die in Europe and 14.000 of them in France. Most people died from heat stroke, and heart and respiratory ailments, as daily maximum temperatures rose to 40 °C and during the night time minimum temperatures stayed above 25 °C on the warmest nights (Fig. I-6).
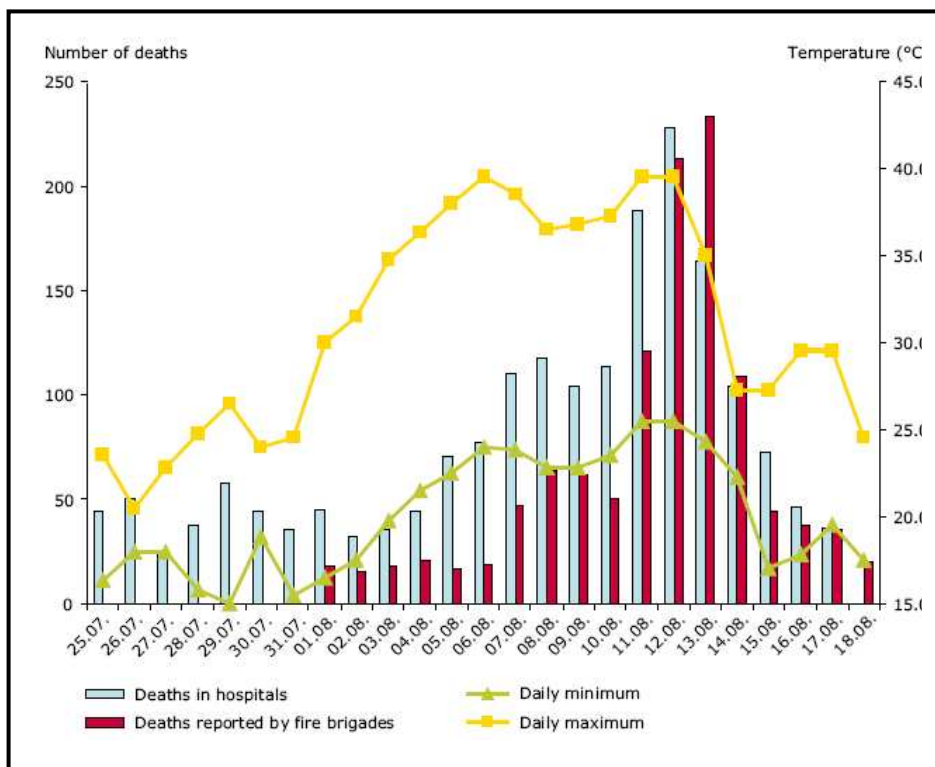


*Figure I-6: Number of reported deaths and minimum and maximum temperatures in Paris during the heat wave in summer 2003 [17].*

With the Kyoto Protocol the EU and most other industrialised countries have subscribed to concrete targets to limit and curb greenhouse gas emissions.

Between 1990 and 2002, emissions decreased by 2.9 % in the EU-15 and by 36 % in the 10 new Member States. Anyway, more cuts in emissions worldwide, than currently imposed by the Kyoto Protocol, are necessary to ensure that the global mean annual temperature does not increase by more than 2 °C compared with pre-industrial levels. The EU is committed to reducing its greenhouse gas emissions by 8 % by 2008–2012 compared with emissions in the base year (1990 for most countries) (Fig. I-7) [17].
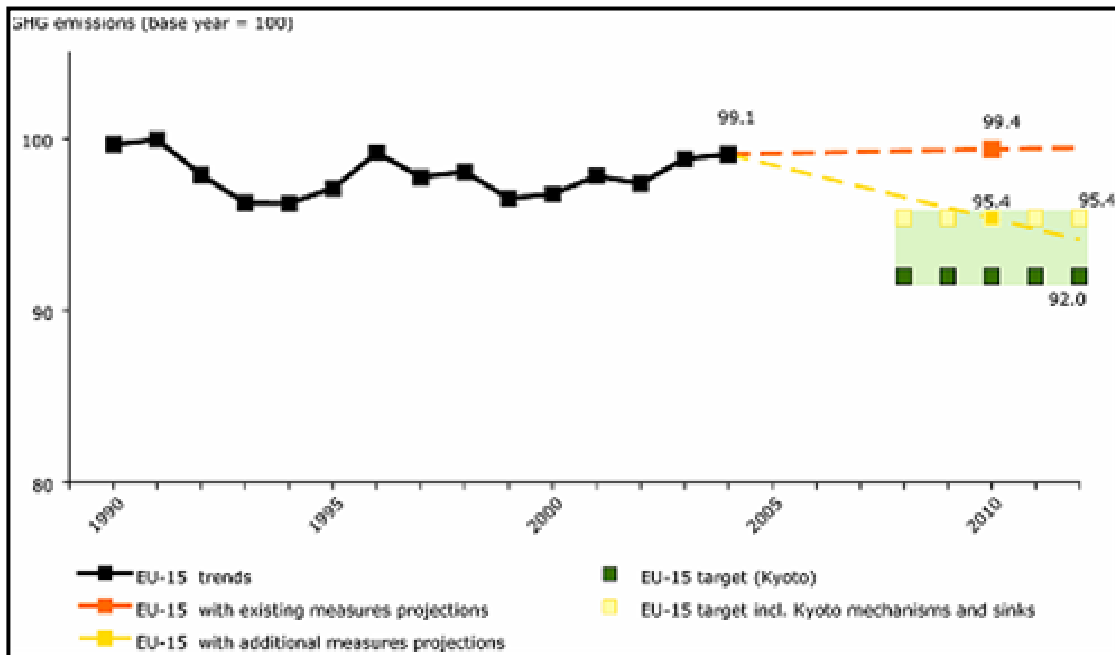


*Figure I-7: EU-15 greenhouse gas emissions 1990-2004 compared with the Kyoto target for 2008-2012 [17].*

## I.7.2.  Ozone layer depletion

The ozone layer is localized at 45 km above the earth at the top of the stratosphere. It protects the earth from the ultraviolet rays emitted by the sun. Ultraviolet radiation (UV) is harmful to life, because it can enter in the cells and destroys the deoxyribonucleic acid of many life forms.

The fact that the ozone layer was depleting was discovered in the mid-1980s. A massive hole in the ozone layer right above Antarctica now threatens not only this continent, but also many others that could be the victims of Antarctica's melting icecaps.

The mechanism of ozone destruction is based on the removal of the chlorine atom from the CFCs (due to the UV-light), which reacts in a first step with the ozone molecule to form ClO and $O_2$. In a second step, a free oxygen atom takes away the oxygen from the ClO, and the final result is an oxygen molecule and a chlorine atom, which reinitiates this cycle again.

The UV-B radiation increase is one of the most harmful consequences of the ozone depletion, because it can cause skin cancer. The rates of malaria and other infectious diseases will increase.

The environment will also be negatively affected by the ozone depletion. The life cycles of plants will change, disrupting the food chain. Other ecosystems, such as forests and deserts will also be harmed. Wind patterns could change, resulting in climatic changes throughout the world.

The CFCs problem may be hard to solve, because there are already great quantities of CFCs in the environment. CFCs would remain in the stratosphere for another 100 years, even if none were ever produced again. By the year 2000, the US and twelve nations in Europe have agreed to ban all use and production of CFCs. This will be highly significant, because these countries produced three quarters of the CFCs in the world.

## I.7.3.  Acid Rains

Acid rain is a widespread term used to describe all forms of acid precipitation (rain, snow, hail, fog, etc.). Atmospheric pollutants, particularly oxides of sulphur and nitrogen, react with water vapour and sunlight, and are converted to sulphuric and nitric acids, hence the term acid rain. Unpolluted rain has a pH value between 5 and 6. When the air becomes more polluted with nitrogen oxides and sulphur dioxide the acidity can increase to a pH value of 4. Some rain with pH 2 has also been recorded. These reactions take hours, or even days, during which polluted air may move hundreds of kilometres. Thus acid rain can fall far from the source of pollution. Rain is always slightly acidic because it mixes with naturally occurring oxides in the air. Though human causes are primarily responsible for acid rain, natural causes exist as well.  Fires, volcanic eruptions, bacterial decomposition, and lightening also greatly increase the amount of nitrogen oxide in the planet's atmosphere.

Acid rains are linked to a range of negative impacts on the environment and human health. They are responsible for the decline of many forests. In West Germany 50% of trees are affected and in Austria, if nothing is done, scientists and environmentalists have predicted that there will be no trees left by the end of the century.

Acid rain can increase the acidity of lakes, dams, and cause the death of the aquatic system. Also, birds can die from eating "toxic" fish and insects. In Sweden more than 18 000 lakes have become acidic.

Acid rain affects also many types of materials, from objects of particular historical, artistic, or cultural value to more ordinary objects such as cars and trucks. Acid rain, especially in the "dry" form, corrodes metal, and accelerates the deterioration of stone and paint.

Many countries in the world are trying to solve the problem in reducing the amount of $SO_2$ and $NO_2$ produced by various ways, either by trying to use "cleaner" fossil fuels or by introducing catalytic converters to their cars, so fewer poisonous gases are produced. In some countries, like Sweden, for example, new power plants use a method called fluidised-bed combustion, which cuts sulphur emissions down by 80 %. In Germany sulphurous smoke is sprayed with lime to produce gypsum, which is then used for building roads. As shown in Fig. I-8 the emissions of acidifying gases have decreased significantly in most EEA member countries [19]. Further developments will save millions of plants, animals, and will be beneficial to human health [18].
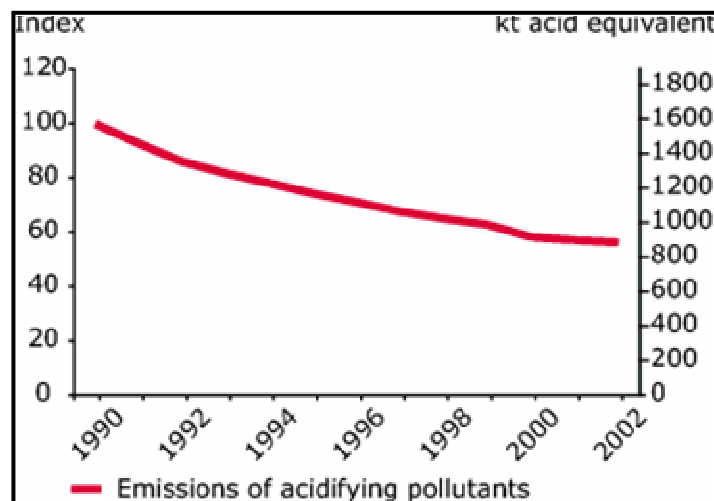


*Figure I-8: Emission trends of acidifying pollutants (EEA member countries), 1990-2002 [19].*

## I.8.  CONCLUSIONS

This chapter is dedicated to the description of different aspects of the atmospheric pollution, the origin of the pollutants, and the effects on human and animal health and on environmental safety. Then we have presented in a first step the main inorganic and organic pollutants to show the interest to control their possible presence. As the indoor life corresponds to 90% of human life, we devoted the second step to indoor specific pollutants. The last part of this chapter concerns the great environmental problems caused by the pollution, i.e., greenhouse effect, ozone layer depletion, and acid rains and the governmental projects to reduce these effects.  As part of an environmental control, an electronic nose would play an interesting role.
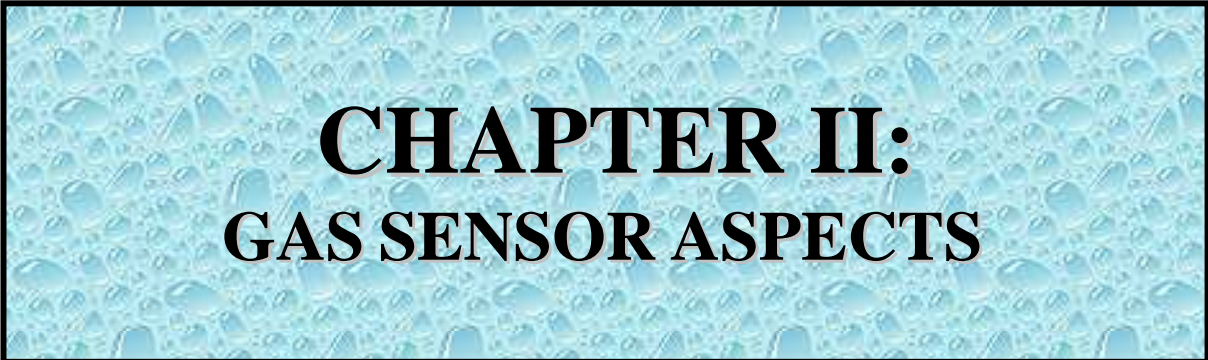
# CHAPTER II:
## GAS SENSOR ASPECTS

- 35 -

# II. GAS SENSOR ASPECTS

## II.1. INTRODUCTION

This chapter deals with a brief description of the chemical sensors and their classification. Furthermore, some general aspects concerning the gas sensors based on metal oxide semiconductors are more intensively discussed. Hence, the Metal Oxide Semiconductor (MOS) types, the conduction mechanisms and principal factors, which affect the MOS performance, are presented. The structure of the materials used in this work (tin oxide, tungsten oxide, zinc oxide, and indium oxide) is also highlighted.

## II.2. CHEMICAL SENSORS: DEFINITION AND CLASSIFICATION

"A chemical sensor is a device that transforms quantitative or qualitative chemical information into an electrical signal as a result of a chemical interaction or process between the analysed gas and the sensor device". This definition is schematically represented in Fig. II-1 [20].
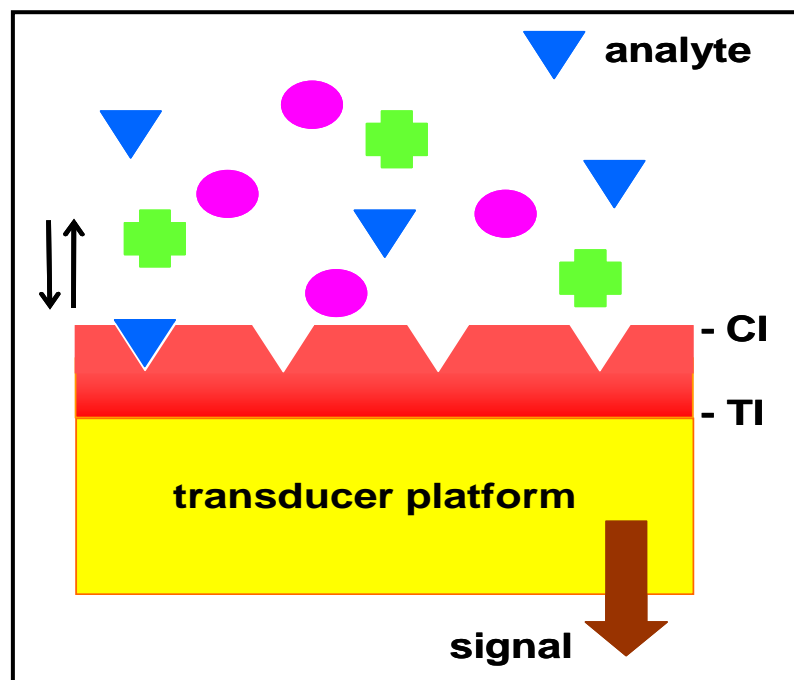


*Figure II-1: Schematical representation of a chemical sensor  (where CI represents the chemical interface and TI represents the transducer interface).*

A more complex and comprehensive definition of a chemical sensor and its properties is given below [21]:

The chemical sensor has:

- a sensitive layer that is in chemical contact with the analyte gas

- a change in the chemistry of the sensitive layer

- no moving parts

Furthermore, the chemical sensors:

- respond to the presence of a chemical with an electrical output

- are physically small

- operate in real time

- presents many physical and chemical properties in the electrical signal output

- are less expensive and more convenient than other instruments for the same type of chemical measurements

Basically, a chemical sensor consists of three different parts: a receptor, a transducer, and a conditioning module defining the operation mode.

The ***receptor*** part concerns the ability of the sensor surface to interact with the target gas and to transform this chemical information into a form of energy.

The ***transducer*** part concerns the ability of the sensor to transform the energy into an useful electrical signal.

These parts are presented in Fig. II-2 and explained in details by Simon et al. [22].

The *receptor* (the semiconductor surface) reacts under exposure to reducing or oxidizing gases with decrease, respectively, increase of the electron depleted region. The gas-induced changes at the semiconductor surface are transduced by the *transducer* (the microstructure of the sensing material), into an electrical output signal. In the case of a polycrystalline material, the grain size and different grain intersections have, thereby, a strong influence on the final *output signal*. In most cases the sensor resistance is monitored as *output signal,* but thermovoltages or changes in sensor temperature (constant power operation), respectively, heating power changes (constant temperature operation) due to gas-specific heat of reactions at the surface can also be used. The possible ***operation modes*** are manifold and allow manipulation of sensor properties.

| Receptor | Transducer | Output | Operation Modes |
|---|---|---|---|
| **Air** | **Surface** | **resistance** | -Constant or modulated operation temperature<br>-AC or DC- measurement<br>-With/without extra electric field |
| **Reducing gas**<br>R O- RO<br>O- O- | **Grain** | **thermovoltage** | -constant(or modulated) operation temperature<br>-constant(or modulated) temperature gradient |
| **Oxidizing gas**<br>X<br>Xᵟ O-<br>O- O-<br>L | **Neck**<br><br>**Nano-crystals** | Heat of reaction:<br>Power or<br>Temperature<br>change | -constant(or modulated) operation temperature or<br>-constant(or modulated) heating power |
| **Surface** | **Microstructure** | **Sensor Element** | **Electronics** |
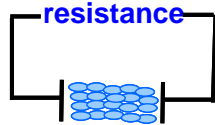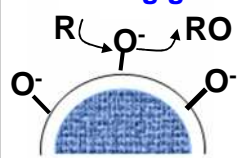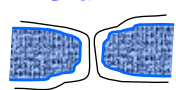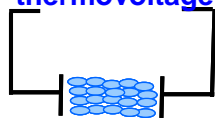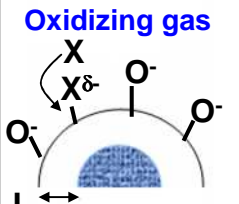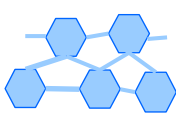
*Figure II-2: Schematic view of gas sensing (L -the thickness of the depletion layer) [22].*

According to Yamazoe [23] the sensors can be characterized also by another part, i.e., the utility part. The *utility* part concerns the accessibility of inner oxide grains to the target gas. This factor is important when the rate of reaction is too large compared to the rate of diffusion. The gas molecules partly cannot access the grains located at inner sites and thus resulting in a loss of the sensor response.

Chemical sensors may be classified according to the operating principle of the transducer in:

- Electrochemical: Voltages, Currents, Impedance
- Radiant: Frequency, Intensity
- Magnetic: Field Strength, Field Direction
- Thermal: Heat flow, Heat content
- Mechanical: Weight, Size, Shape

A schematic representation of this classification is presented in Fig. II-3 [21].
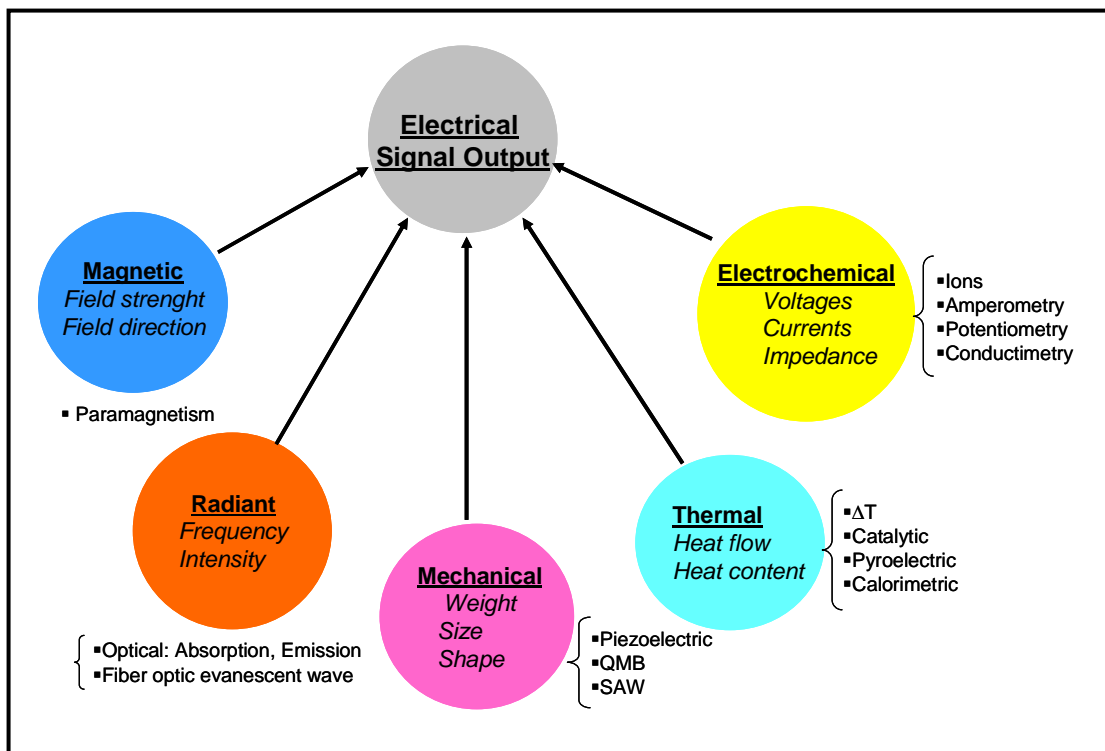
*Figure II-3: Classification of chemical sensors using the transducer mechanism [21].*

This work is focused on studying the conductometric sensors, i.e., semiconductor metal oxide gas sensors, hence more details about this type of sensors are given below.

## II.3. SEMICONDUCTOR METAL OXIDE GAS SENSORS

In 1952 Brattain and Bardeen first reported gas sensitive effects with Germanium [24]. Later, in 1962 Seiyama demonstrated that thin films of ZnO, heated to 300°C in air, change their conductivity in the presence of reactive gases [25]. In the same year, Taguchi [26] demonstrated similar properties for $SnO_2$ with the advantage of greater stability.

### II.3.1. Geometry types of MOS sensors

A sensor device comprises a *sensitive layer* deposited on a *substrate*, which is provided with *electrodes* for the measurement of the electrical properties. The sensors are heated by their own *heater,* or in special furnaces.

- *Sensitive layer* - It can be made of metal oxide semiconductors like $SnO_2$, $WO_3$, $TiO_2$, ZnO, etc.

• *Substrate* - There is a large number of substrates, suitable for deposition of gas sensing metal oxide films, i.e., polycrystalline $Al_2O_3$, Si, MgO, ZrO, $Al_2O_3$ single crystals with specific crystallographic orientation, glass, ceramics, etc.

By selecting substrates with corresponding lattice parameter and thermal expansion coefficient as the MOS, it is possible to minimize the mechanical strains and the thickness of the transition layers, which are the sources of temporal instability of film parameters [27].

• *Electrodes* - Generally, the electrodes are located underneath the sensing film, but the deposition of so-called top electrodes on thin gas-sensitive tin oxide layers has also been realized. Usually, the electrode materials are gold and platinum, but aluminium or tungsten has also been used. The aluminium contact properties to the sensing film are rather bad and the maximum operation temperature is limited to about 500 °C due to the thermal migration and oxidation of the Al. To achieve good adhesion of the electrodes adhesion layers are often employed. Chung et al. [22] used, for example, 20 nm Ti as adhesion layer before deposition of platinum.

• *Heater* - Heater structures needed to control the sensor operation temperature can be integrated in two different ways. In case platinum or gold are used as electrode materials, heater structures can be integrated in the same layer as the electrodes (horizontal approach), this is advantageous because no additional process steps are needed to form the heater. The design in a vertical approach, where the heater is formed in different layers than the electrodes, is also possible and allows much more freedom.

The most used sensor designs are the tubular and the planar structures as shown in Fig II-4 (a, respectively, b).
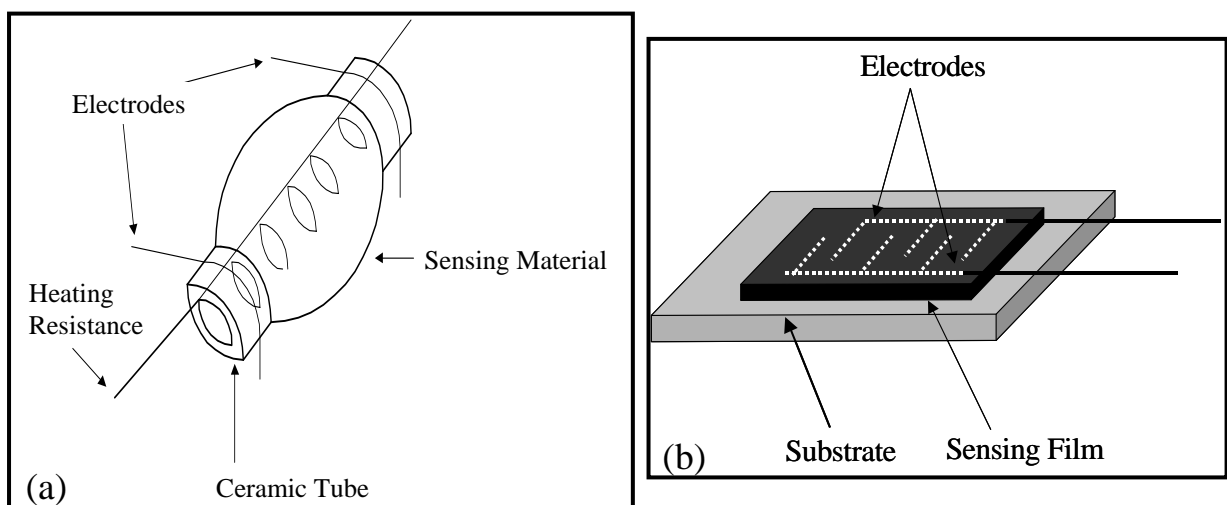


*Figure II-4: The tubular (a) and planar gas sensor designs (b).*

The planar sensor has the advantage that the film can be deposited using various techniques and this type of sensor is promising for designing a microsensor or a sensor array device.

## II.3.2. Gas Sensor Conduction Mechanism

The sensing mechanism of a MOS is based on the material conductivity (or resistance) change when it is exposed to different kinds of oxidizing or reducing gases. Despite such simple detection principle, the sensing mechanism is quite complex. The adsorption model is generally used to explain the change in conductivity. Briefly, this model can be explained as follows, when oxygen is adsorbed on the surface of an n-type semiconductor, like $SnO_2$, it traps electrons from the oxide ($O_2^-$, $O^-$, $O^{2-}$) and a space charge layer (Schottky barrier) is formed. The representative energy band diagram for $SnO_2$ is shown in Fig. II-5.
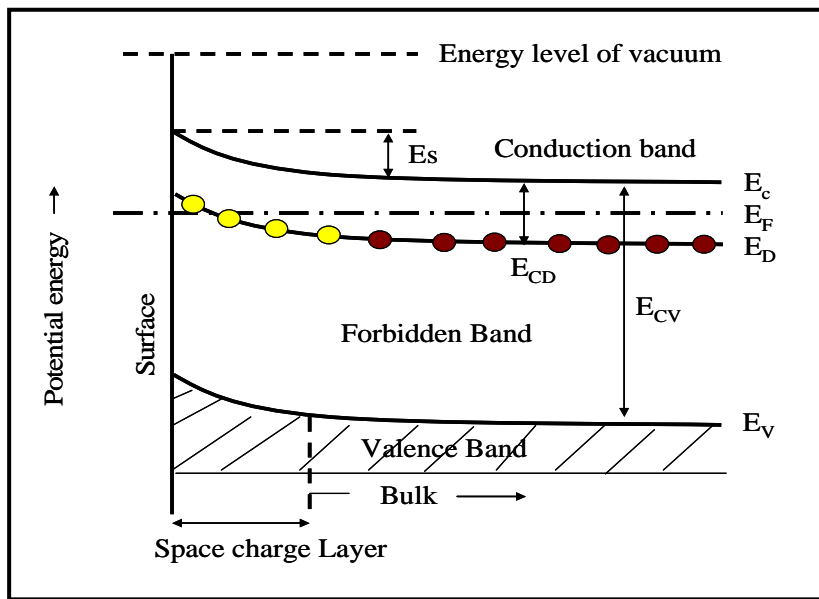


*Figure II-5: Energy diagram for $SnO_{2-x}$ with negatively charged adsorbed oxygen. Where: $E_s$: potential barrier; $E_F$: Fermi level; $E_D$: donor level; $E_C$: lowest level of conduction band; $E_V$: highest level of the valence band; $E_{CD}$: depth of donor level; $E_{CV}$: energy gap between $E_C$ and $E_V$ [28].*

This phenomenon gives rise to a decrease of the conductivity. When the film is exposed to reducing gases (CO, $H_2S$, etc.), these species react with the adsorbed oxygen at the intergrains leading to an Schottky barrier decrease ($E_s$) (Fig. II-6 a) and an electrical conductivity increase (Eqs. II-1 and II-2). When the film is exposed to oxidizing gases, the

Schottky barrier increases (Fig. II-6 b) and a decrease in electrical conductivity occurs due to the chemisorptions of gas molecules and the capture of conduction band electrons (Eq. II-3) [29].

$$(SnO_2 + e^-) + 1/2O_2 \leftrightarrow SnO_2\,(O^-)_{ad.} \qquad\qquad \text{Eq. II-1}$$

$$SnO_2\,(O^-)_{ad.} + CO \rightarrow (SnO_2 + e^-) + CO_2 \qquad\qquad \text{Eq. II-2}$$

$$SnO_2\,(e^-) + NO_2 \rightarrow SnO_2\,(NO_2^-) \qquad\qquad \text{Eq. II-3}$$
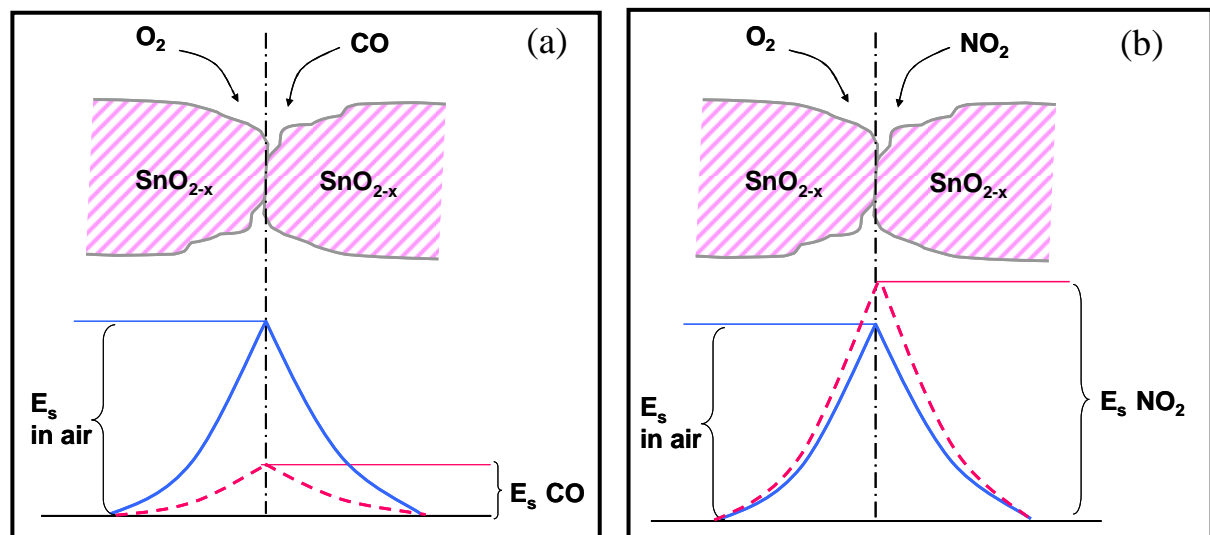


*Figure II-6: Model of potential barrier at grain boundary (a) reducing gases and (b) oxidizing gases [28].*

Table II-1 reveals the conductivity change of n and p-type MOS, if exposed to reducing or oxidizing gases.

| Conductivity type | Reducing Gas | Oxidizing Gas |
|---|---|---|
| **n**-type | R↓ | R↑ |
| **p**-type | R↑ | R↓ |

*Table II-1: MOS gas sensor behavior exposed to reducing or oxidizing gases.*

However, some experimental data cannot be explained assuming this adsorption model. Another approach of the detection mechanism takes into account the possibility of chemical interaction between the gas phase and the oxide surface. A redox reaction between the gas phase and the oxide surface can lead to a modification of the valence state of the surface ions, the appearance of anion vacancies, a change of the Me-O binding energy, and the coordination of ions [30].

## II.3.3. MOS performance parameters and influence factors

There are three parameters which should be improved in order to obtain an accurate sensor device. These are sensitivity, selectivity, and stability.

*Sensitivity*

The sensitivity represents the ability of the device to percept a variation in a physical and/or chemical property of the sensing material under gas exposure. In order to improve the sensitivity, it will be of great interest to work with the most appropriate sensing material in every case and to obtain its optimum detecting temperature.

Taking into account that sensing reactions take place mainly at the sensor's surface layer, the control of semiconductor composition, morphology, and microstructure are required for enhancing the sensitivity of the sensor.

Sensitivity is defined by the resistance change when the sensor is exposed to a certain concentration of gas. However, the most used parameter is the gas sensor response (S), which is defined as the ratio of $R_{gas}$ to $R_{air}$ for oxidizing gas and $R_{air}$ to $R_{gas}$ for reducing gas, where $R_{air}$ represents the electrical resistance of the film in air and $R_{gas}$ represents the resistance of the film during gas exposure. The usually used expressions for an n-type gas sensitive material like $SnO_2$, are:

$$S = \frac{R_{air}}{R_{gas}} \qquad \text{for reducing gases} \qquad \text{Eq. II-4}$$

$$S = \frac{R_{gas}}{R_{air}} \qquad \text{for oxidizing gases} \qquad \text{Eq. II-5}$$

In this way sensitivity should be always larger than 1.

*Selectivity*

This property is related to the discrimination capacity of a sensor in the presence of a mixture of gases.

*Stability*

This property takes into account the repeatability of the device measurements after a long use. To avoid the effects of no repeatability after an important use, the sensor materials can be subjected to a thermal pre-treatment, which would decrease the material instabilities during the time of operation.

Continuous research efforts are focused on improving the sensitivity, selectivity, and stability of these sensors. While instability represents to date the most important unsolved problem of these sensors, different promising methods have been employed to improve the sensitivity and to overcome the lack of selectivity.

There are few important parameters, which can influence the sensor performances and they will be discussed here.

➢ *Surface or bulk doping*

It has been demonstrated that the semiconductor oxide, activated by metals (Pd, Pt, Au, Ru, Rh, and Ti), are more sensitive, selective and shows a faster response time to certain gases [11,31,32]. It is believed that the addition of noble metals on the surface of MOS forms metallic clusters on the surface of the oxide grains and additional absorption sites, and also catalysis redox reactions at the surface can take place. However, there are studies suggesting a more complicated mechanism including the modification of the metal oxidation state, the creation of new bonds between oxide sensor and dopant metal, the activation and the spill-over of the gas, the removal of lattice oxygen, etc. [31,33].

Several authors showed that heterostructures or sandwich structures between two MOSs could improve the sensitivity, selectivity, the response and the recovery speed. The increase in sensitivity is associated with the formation of p-n heterostructures based on the interface between p-type and n-type semiconductors [34,35] but heterojunctions formed between two n-type semi-conducting materials have also been described [36]. The detection mechanism of heterostructures is based on changes in current flow across the junction.

The sensor response can be improved also by bulk doping with metal oxides. For example, Zhao et al. [37] enhanced the sensitivity for $NO_2$ using $WO_3$ films doped with $Al_2O_3$ and $TiO_2$. The obtained result is due to the modification of the triclinic $WO_3$ phase into tetragonal $WO_{2.9}$ and due to the decrease of the sensor material particle size.

Ruiz et al. [38] showed that $TiO_2$ doped with $Nb_2O_5$ increases the sensitivity to CO, while the sensitivity to ethanol is inhibited. In the first case the increase in the sensitivity of CO is based on the formation of new electronic states due to the donor-type behaviour of Nb while the inhibition of the sensitivity to ethanol involves the acidic properties of niobium. The acidic oxides favour the dehydratation reaction of ethanol (Eq. II-6), which will not significantly improve the sensitivity. On the contrary, the basic oxides favour the dehydrogenation reaction of ethanol (Eq. II- 7) and the sensitivity is greatly improved.

Dehydratation: $\qquad C_2H_5\text{-}OH \rightarrow C_2H_4 + H_2O \qquad$ Eq. II-6

Dehydrogenation: $\qquad C_2H_5\text{-}OH \rightarrow CH_3CHO + H_2 \qquad$ Eq. II-7
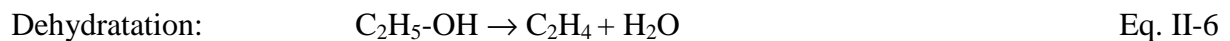
Lalauze et al. [39] showed that electrical properties of $SnO_2$ are greatly modified after a sulphur dioxide treatment (1000 ppm $SO_2$ at 500 ºC for 10 min). This treatment allows the stabilization of $SnO_2$ before gas exposure and the increase of $SnO_2$ sensitivity to different pollutant gases.

➢ *Influence of operating temperature*

The temperature has an important effect on the sensitivity of MOS gas sensors, as it influences the physical properties of semiconductors (change of the free carrier concentration, Debye length), but also because every reaction taking place at the semiconductor surface are temperature dependent. The adsorption and desorption processes are temperature-activated processes, as well as surface coverage by molecular and ionic species, chemical decomposition, reactive sites, etc.

At room temperature under ambient air operating conditions, the surface of the gas sensor is mainly covered by *oxygen* and *water* species. These species undergo changes as function of the temperature.

The *oxygen* adsorbed in molecular form can be ionised even at room temperature, and increasing the operating temperature will transform it in other species ($O_2^-, O^-, O^{2-}$) as shown in Eqs. II-8-11 [40-42].

$$O_{2(gas)} \Leftrightarrow O_{2(ads)} \qquad\qquad\qquad\qquad\qquad\qquad\qquad\qquad\qquad \text{Eq. II-8}$$

$$O_{2(ads)} + e^- \Leftrightarrow O_{2(ads)}^- \qquad\quad T < 100\ ^\circ C \qquad\qquad\qquad\qquad \text{Eq. II-9}$$

$$O_{2(ads)}^- + e^- \Leftrightarrow 2O_{(ads)}^- \qquad\quad T = 100\text{-}300\ ^\circ C \qquad\qquad\qquad \text{Eq. II-10}$$

$$O_{(ads)}^- + e^- \Leftrightarrow O_{(ads)}^{2-} \qquad\quad T > 300\ ^\circ C \qquad\qquad\qquad\quad \text{Eq. II-11}$$

When the sensor is exposed to a pollutant gas, the type of oxygen formed at a certain temperature reacts with the gas, and determines the maximum sensitivity.

At room temperature the *water* can be adsorbed in two states on the surface of a MOS: molecular water ($H_2O$ -physisorption), and hydroxyl groups (OH⁻ - chemisorption). Adsorption of water vapour always produces a large increase in the conductivity of the gas sensor.

Increasing the temperature from room temperature to 100 °C the desorption of water takes place and the conductivity decreases. Increasing the temperature more than 160 °C the water molecules dissociate in OH⁻ and H⁺. The desorption of OH⁻ groups as water begins at 250 °C and finishes at about 500 °C [43]. All these transformations influence the detection of the gas.

It is, therefore, very important to control the temperature in order to achieve the best sensor performance. In this way, the sensitivity of a gas sensor reaches a maximum at a certain operating temperature.

> ➤ *Influence of temperature modulation*

Yamazoe et al. [44] have demonstrated that monitoring the operating temperature, at which a semiconductor oxide sensor shows maximum sensitivity, can be used to enhance the selectivity.

Heiling et al. [27] improved the selectivity for CO in the presence of $NO_2$ by modulating the temperature of the sensor. The authors explained that the molecule identification using the temperature modulation is possible due to the reaction kinetics of the interacting gases at the surface.

Simultaneous measurements of the change in the semiconductor temperature ($\Delta T$) and sensor resistance ($\Delta R$) gives another method for the identification, using a single $SnO_2$-based gas sensor. The advantage over the conventional methods is that the gas identification can be made without problem even if the concentration of the gas is changing during the measurements [28].

> *Influence of crystallite size*

Xu et al. [29] reported a description of the grain size influence on the gas sensitivity. They considered that the gas sensor material is made by a chain of crystallites, which are connected mostly by necks but also by grain-boundary contacts. They state that the resistance of the film is controlled as a function of the relation between crystallite size diameter (D) and the space-charge layer thickness. In this way, three cases were distinguished: D >> 2L, D $\geq$ 2L and D < 2L (Fig. II-7) the resistance is controlled by grain-boundaries in the first case, by necks in the second case and by grains in the third case.

The sensitivity of the film is higher when the film resistance is controlled by the grains (D<2L) when their size is below the critical crystallite size [30].
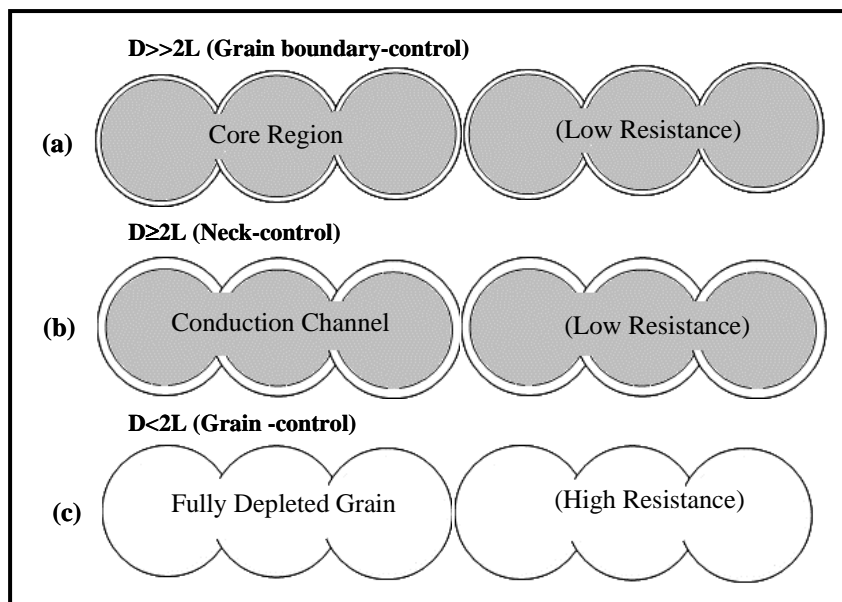


*Figure II-7: Schematic model of the effect of the crystallite size on the sensitivity of a metal oxide gas sensor: (a) D>>2L (grain-boundary control); (b) D≥2L (neck-control); (c) D<2L (grain-control) [29].*

➢ *Influence of film porosity*

The interaction of dense or porous layers with surrounding gases is rather different. Porous layers are accessible to gases due to the large internal surfaces, whereas dense layers only interact with gases at the geometric surface [31]. Due to the large gas-active surface internal areas of porous layers compared to dense layers, higher sensitivity and immunity to poisoning of sensors is expected in the case of porous layers. Increasing the porosity may also lead to the improvement of the gas sensitivity. The gas diffusion through a porous material is enhanced with the increase of the pores size as described by Knudsen equation (Eq.II-12)

$$D_K = \frac{4r}{3} \sqrt{\frac{2RT}{\pi M}}$$
Eq. II-12

where $D_K$ is the Knudsen diffusion constant, r is the pore radius, R is the gas constant, T is the temperature, and M the molecular weight [32].

➢ *Influence of film thickness*

As reported in the literature [33], the sensitivity of a sensor film increases when decreasing the film thickness. Moreover, it has been observed [34] that below a critical film thickness (about ~110 nm), the sensitivity lowers with further decrease in film thickness. This behaviour can be ascribed to the fact that porosity in this case is reduced considerably, hence, the active sites for gas molecules to be adsorbed are reduced and as a consequence the sensitivity decreases.

➢ *Use of electronic nose*

The main disadvantage of MOS sensors is that they respond in the same way to practically all the gases. In our atmosphere, there are many kinds of gases, so it is very important to distinguish a certain gas from a mixture of gases. Using a sensor array, coupled with an appropriate pattern recognition method, qualitative and quantitative information can be obtained.

Qualitative analysis (identification of a certain gas from a mixture of gases) and quantitative analysis (determination of each gas concentration) can be usually achieved

employing linear pattern recognition methods such as: Principal Component Analysis (PCA) and Discriminant Factor Analysis (DFA). Another pattern recognition method widely used to process the sensor array data is the Artificial Neural Network (ANN), i.e., probabilistic neural network, back propagation trained neural network, and radial basis function neural network.

Over time, different semiconductor materials have been studied intensively for gas sensing applications. These oxides can be obtained in various forms, such as powders, thick and thin films. Thin films seem to be more suitable for gas sensing purposes, because of the possibility of miniaturisation, low cost, easy implementation of the electrodes, etc. The following oxides: $SnO_2$, $ZnO$, $In_2O_3$, and $WO_3$ used in this work will be presented in the next part.

## II.4.    MATERIALS FOR GAS SENSORS

### II.4.1. Tin oxide (SnO$_2$)

The tin oxide is a wide bad-gap semiconductor (energy band gap 3.6 eV) and it has only one stable phase, which is named cassiterite (mineral form), or rutile (material structure). The SnO$_2$ rutile unit cell contains six atoms (two tin and four oxygen atoms) as shown in Fig. II-8. The tin atom occupies the centre of a surrounding core composed of six oxygen atoms placed approximately at the corners of a quasi-regular octahedron. In the case of oxygen atoms, three tin atoms surround each of them, forming an almost equilateral triangle. The lattice parameters are: a = b = 4.737 Å and c = 3.186 Å [35].
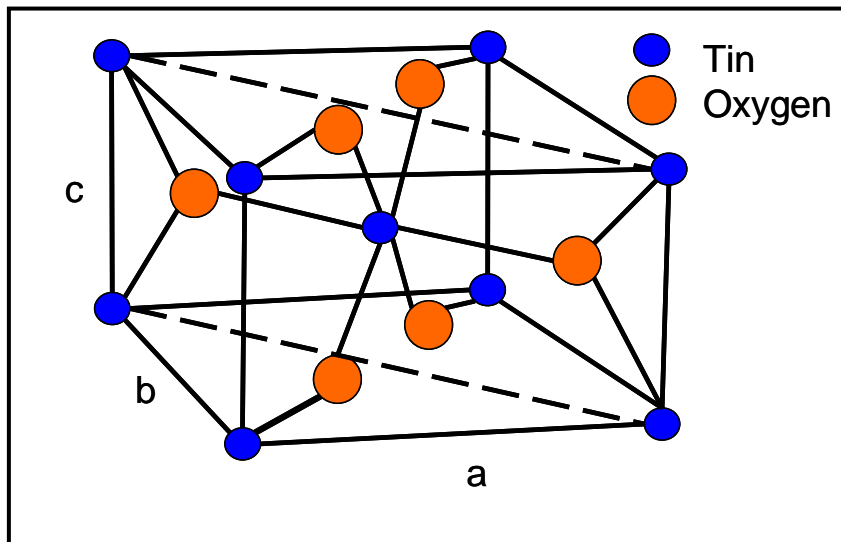


*Figure II-8: Tetragonal unit cell of SnO$_2$.*

### II.4.2. Tungsten oxide (WO$_3$)

WO$_3$ is an n-type semiconductor (energy band gap 2.7eV) with a perovskite-like structure (ABO$_3$) (Fig. II-9). Each tungsten ion is surrounded by six oxygen atoms forming an octahedron. The slight rotation of these octahedra causes a lattice distortion and reduces the symmetry [36,37]. At room temperature WO$_3$ exhibits a triclinic or monoclinic phase, but it can suffer the following phase transitions (i.e., orthorhombic, tetragonal) upon heating, as shown in Table II-2. Other phases, i.e., hexagonal and cubic have been also reported in the literature. The hexagonal WO$_3$ is obtained usually by dehydratation of tungsten trioxide

hydrate ($WO_3 \cdot xH_2O$) and is an important material in the intercalation chemistry [38]. The formation of cubic $WO_3$ was observed at high temperature during the dehydratation of tungstophosphate ($AlPW_{12}O_{20}$) [39] or tungstite ($WO_3 \cdot H_2O$) [40].
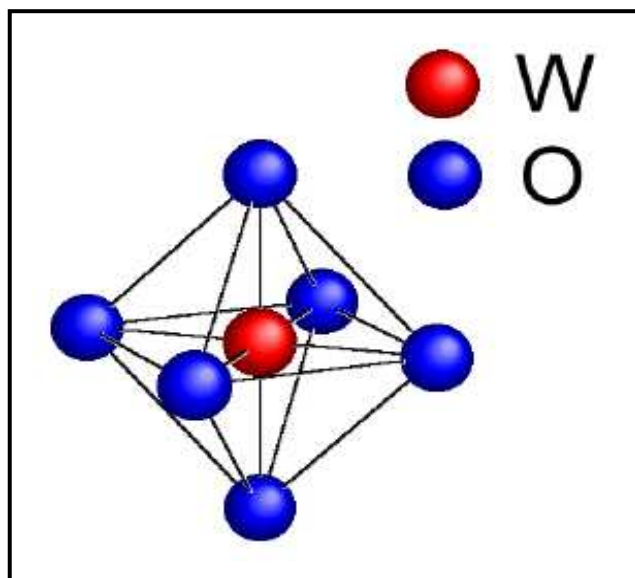


*Figure II-9: Schematic representation of a $WO_3$ octahedron in the cubic phase [41].*

| Phase | Symmetry | Space Group | Lattice Parameters (Å) | | | Temperature Range (ºC) | References |
|---|---|---|---|---|---|---|---|
| | | | a | b | c | | |
| t-**WO₃** | Tetragonal | P4/nmm | 5.25 | 5.25 | 3.92 | >720 | [42] |
| o-**WO₃** | Orthorohmbic | Pmnb | 7.34 | 7.54 | 7.75 | 320-720 | [43] |
| m-**WO₃** | Monoclinic | P2₁/n | 7.30 | 7.54 | 7.68 | 17-320 | [44,45] |
| t-**WO₃** | Triclinic | P1 | 7.31 | 7.52 | 7.69 | <17 | [44,46] |
| h- **WO₃** | Hexagonal | P6/mmm | 7.30 | | 7.80 | | [38] |
| c- **WO₃** | Cubic | | | 7.52 | | | [39] |

*Table II-2: The Polymorphs of WO₃.*

## II.4.3. Zinc oxide (ZnO)

ZnO is an n-type semiconductor (energy band gap 3.37 eV), but p-type conductivity of ZnO has also been reported for synthesis under specific conditions [47]. The stable phase of ZnO is the hexagonal wurtzite structure and can be described as a number of alternating planes composed of tetrahedrally coordinated $O^{2-}$ and $Zn^{2+}$ ions, stacked alternately along the c-axis (Fig. II- 10) [48]. This structure can be transformed into the cubic rocksalt structure under pressure. By decompression, the rocksalt structure does not convert to the wurtzite one at room temperature, but only at elevated temperatures. Another cubic phase, i.e., zinc-blende (sphalerite), has also been reported [49]. The lattice parameters and space groups of these three phases are presented in Table II-3.

| Phase | Symmetry | Space | Lattice Parameters (Å) | | References |
|---|---|---|---|---|---|
| | | | a | c | |
| h-**ZnO** | Hexagonal Wurtzite | P6₃mc | 3.249 | 5.204 | [50] |
| c-**ZnO** | Cubic rocksalt | Fm3m | 4.294 | | [49] |
| | Cubic Zincblende | F43m | 4.614 | | |

*Table II-3:The Polymorphs of ZnO.*
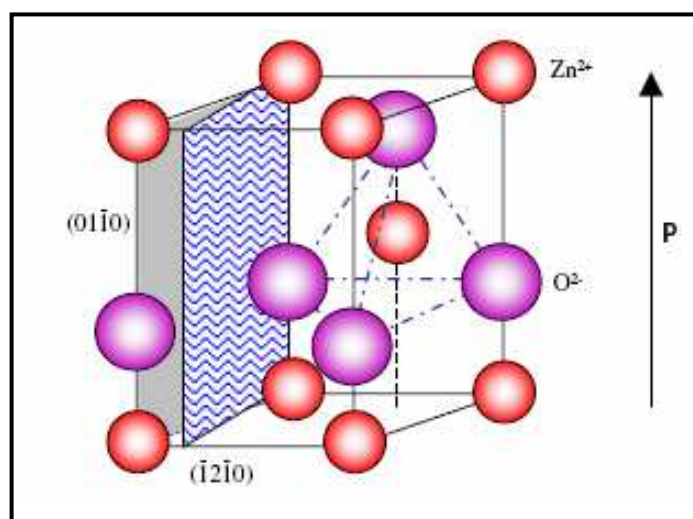


*Figure II-10: Wurtzite structure model of ZnO showing the tetrahedral coordination of Zn and O [48].*

## II.4.4. Indium oxide (In$_2$O$_3$)

Indium oxide is a wide band gap n-type semiconductor (energy band gap 3.6 eV). Two crystal structures have been reported for In$_2$O$_3$, i.e., the bixbyite structure (rare-earth oxide structure) which has a body centred cubic structure with space group Ia3 and lattice parameter a = 10.118Å (JCPDS 06-0416) and the metastable corundum ($\alpha$-Al$_2$O$_3$) structure which has a rhombohedral structure with space group R-3c and lattice parameters a = 5.484 Å and c = 14.508 Å (JCPDC 22-336). The rare-earth structure can be transformed into the corundum structure at high temperatures (1000 °C) and high pressure (65 Kbar) [51]. Recently [52], the metastable corundum In$_2$O$_3$ structure has been obtained also under ambient pressure by annealing InOOH in air at temperatures starting from 485 °C.

Since the indium oxide cubic form is the stable one and the most used, it will be described now. In the cubic form, the cations form a nearly cubic face-centered lattice in which six out of the eight tetrahedral sites are occupied by oxygen ions. The unit cell of the crystal structure consists of eight such cubes, containing 32 cations and 48 O$^{-2}$ ions. Two nonequivalent cation sites, called ''C'' and ''D'', both with 6-fold oxygen coordination, characterize the structure. The site D is axially symmetric and can be described as a cation surrounded by six oxygen ions at the corners of a distorted cube, leaving free two corners of a diagonal body. For site C the cube is more distorted and the six oxygen ions leave free two corners of a face diagonal (Fig. II-11) [53].
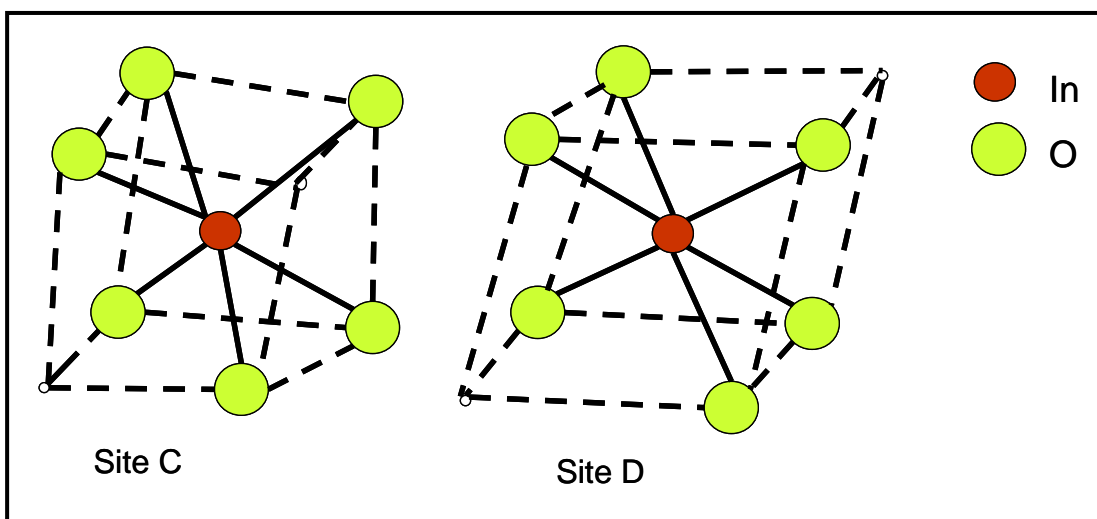


*Figure II-11: The nearest –neighbour oxygen distribution around each cationic site C and D in the In$_2$O$_3$ bixbyite structure [53].*

## II.5.   CONCLUSIONS

After a first description of chemical gas sensors, the metal oxide semiconductor sensors, which actually are used in this work, have been widely presented. Because it is important to understand the working principle of these sensors, the concerned conduction mechanisms are explained. The adsorption model is presented in detail considering, that it is the generally accepted model.

The MOS performance parameters like sensitivity, selectivity, and stability are described along with factors, which influence them. We have observed that parameters such as operating temperature, particle size, film thickness, and porosity are important to achieve the optimal sensor performances. The end of the chapter is devoted to the structure of tin (IV) oxide, tungsten (VI) oxide, zinc oxide and indium (III) oxide studied as materials for gas sensing measurements.

# CHAPTER III: EXPERIMENTAL ASPECTS

# III.   EXPERIMENTAL ASPECTS

## III.1.   INTRODUCTION

In this chapter we present the deposition method of the MOS films and also the experimental techniques used to study the morphological and structural properties of these films, followed by the experimental set-up used to characterize the film gas sensor performances.

Firstly, the Electrostatic Spray Deposition (ESD) technique is described with the experimental set-up used to deposit the films, followed by the preparation of the different solutions and the deposition parameters used to fabricate the layers.

In the second part the characterization techniques used to study the morphology and microstructure of the films, i.e., Scanning Electron Microscopy (SEM) coupled with Energy Dispersive X-ray analysis (EDX), Transmission Electron Microscopy (TEM), X-ray Diffraction (XRD) and Raman spectroscopy are discussed.

The third part deals with the gas sensor measurement system used in this work and also with the presentation of the working procedure for studying the gas sensor properties of the films.

## III.2.  ELECTROSTATIC SPRAY DEPOSITION TECHNIQUE

Electrostatic Spray Deposition (ESD) is a technique mainly used to deposit thin films of functional metal oxides with application in different fields, i.e., rechargeable lithium-ion batteries, $LiCoO_2$ [71], $Li_{1.2}Mn_2O_4$ [72], solid oxide fuel cells, yttria-stabilized zirconia [73], gadolinia-doped ceria, and $LaGaO_3$ [74], microelectromechanical systems, $Pb(Zr, Ti)O_3$ [75], heat exchange reactors, $TiO_2$ [76],  protecting layer for dielectrics, $MgO$ [77], sensors, $SnO_2$ [78,79], and even in biomedical ceramic implants, CaP [80]. Furthermore, there are studies revealing that protein [81] or polymer [82] films can be deposited using this technique.

The basic principle of the Electrostatic Spray Deposition technique consists of the generation of an aerosol from a precursor solution when a strong electric field is applied between a metallic nozzle and a substrate. The precursor solution comprises an organic solvent in which an inorganic salt is dissolved. As a result of the applied voltage difference, the aerosol made from highly charged droplets is attracted by the grounded and heated substrate where they impinge and loose their charge. After complete solvent evaporation a thin film of inorganic material is formed onto the substrate surface.

This deposition technique presents several advantages in comparison with other deposition techniques like: chemical vapor deposition, sputtering, pulsed-laser deposition etc. and will be described in more detail:

- very simple and low cost experimental set-up
- ambient atmosphere operation
- easy control of the morphology of the deposited layers
- the overall film composition is the same as that of the precursor solution
- high deposition rate and efficiency
- wide choice of precursors [83]

In this thesis the ESD technique is used to deposit films of tin oxide, tungsten oxide, indium oxide and zinc oxide on Pt-coated alumina substrates for gas sensor applications. Hence, the ESD processes involved in the formation of these films will be discussed.

The principal conditions to spray films with ESD are:

- the precursor salt must be soluble in the solvent,
- organic solvents with lower surface tension are usually demanded  because the liquid surface tension influences the electrical discharge and it is very difficult to spray solutions with a high surface tension (i.e., aqueous solutions).

It is obvious that the choice of the precursor and the solvent is very important in order to be able to spray and to obtain good quality layers. Supplementary information concerning the types of precursors, solvents, substrates that can be used with the ESD technique are presented elsewhere [83].

## III.2.1. Processes involved in the formation of the ESD films

There are a few physical and chemical processes involved in the ESD formation (Fig. III-1) of the layers, i.e.,

1. spray formation
2. droplet transport, evaporation, disruption
3. preferential landing of droplets
4. discharge, droplet spreading, drying
5. surface diffusion, reaction [83]
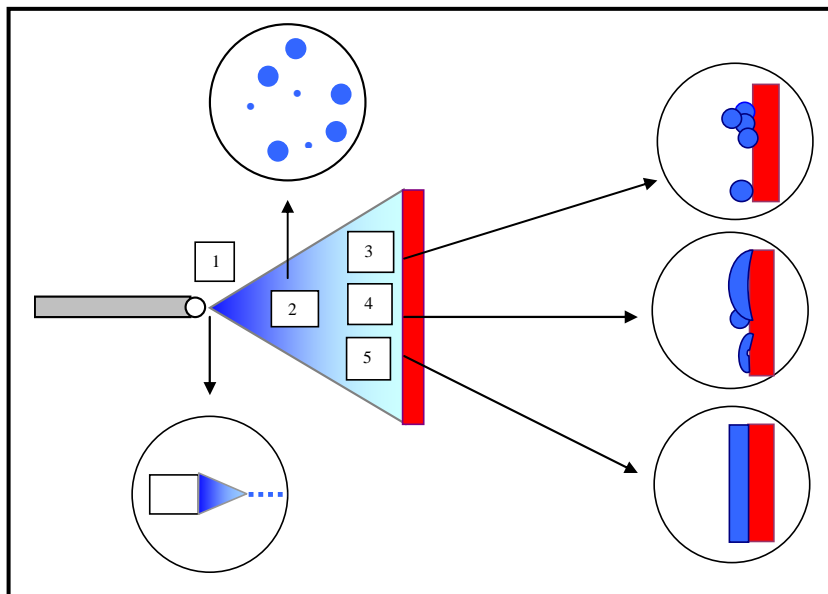


*Figure III-1: Processes involved in formation of the ESD films.*

Because these processes can influence the morphology of the deposited layer, they will be described in the following paragraphs.

### 1. Spray Formation

The formation of a spray using an electric field is named ElectroHydroDynamic Atomization or more commonly electrospraying [84]. The electrospraying process is

governed by the physical properties of the liquid such as surface tension, viscosity, density, and electrical conductivity. This process depends also on the capillary diameter, the electric field strength, and the liquid flow rate. The combination of these parameters allows the generation of certain modes of spraying as shown in [85]. From these spraying modes the most investigated one is the cone-jet mode. Taylor has shown that, when the electric field is strong enough (3-15 kV), the electrostatically stressed liquid surface can be distorted into a stable conical shape (Taylor cone). The Taylor cone emits charged droplets ($10^8$-$10^{10}$ droplets/ second) after the application of the electric potential. The droplet size depends on the flow rate of the solution, the conductivity, and the permittivity of the solution, as it can be seen in Eq. III-1 [83]:

$$d \sim \varepsilon_r^{1/6} \left( \frac{Q}{k} \right)^{1/3}$$

Eq. III-1

Where d is the droplet size, $\varepsilon_r$ is the relative permittivity of the solution, Q the flow rate, and k the electrical conductivity.

The spray of charged droplets is attracted by the heated substrate. During the flight of the droplets and after impingement onto the substrate, some processes will occur, influencing the final morphology of the films. These processes can be theoretically explained.

## *2. Droplet transport, Evaporation, Disruption*

### A. Droplet transport

A charged droplet is attracted by the grounded substrate due to a Coulombic force and simultaneously by a gravitational force, and a viscous drag force. These forces will determine the trajectory and the flight time from the nozzle to the substrate for this droplet. In the case of electrostatic spraying the gravitational force can be neglected because the droplets are very small. The real situation is further complicated by the non-uniform temperature profile, the evaporation process, and also by the possible droplet disruption.

### B. Evaporation

Solvent evaporation during the flight of the solution occurs depending on the substrate heating condition inducing a shrinkage of the droplet, the total charge remaining the same.

## C. Disruption

A charged droplet ("mother droplet") can be disrupted in a few smaller droplets ("daughter droplets") after reaching a maximum attainable charge density, $q_r$, for a liquid droplet with a radius a. This is the so-called Rayleigh limit [83].

### 3. Preferential landing of droplets

In the strong electric field, induced charges exist on the surface of the grounded substrate, with a sign opposite to that of the droplets and the nozzle. The charge distribution is generally not uniform, but depends on the position relative to the nozzle and, in particular, on the local curvature of the surface. The charges concentrate more at the places where the curvature is greater, making the electric field the strongest there. When a charged droplet approaches the surface, it will be attracted more towards these more curved areas. This is referred to a "preferential landing" and will cause the agglomeration of the particles especially when the incoming droplets are small. Consequently, the topography of the substrate surface has a large influence on the morphology of the produced layers [83].

### 4. Discharge, Droplet spreading

## A. Discharge

When a charged droplet gets in contact with the substrate or the formed layer, the droplet is discharged, by transferring the charge to the grounded substrate. This process is very fast if the electronic conductivity of the substrate (i.e. metallic substrate) and of the deposited layer is relatively high. In this case the discharge is not expected to determine the morphology of the layer [83]. In the case of an alumina substrate, which is an insulator, the discharge will be slow and will influence the morphology.

## B. Spreading

If the evaporation of the solvent is not finished when reaching the heated substrate, the solution wets the surface of the substrate or of the already deposited layer. The types and dynamics of spreading depend upon the spreading coefficients:

$$S = \Upsilon_{sv} \cdot \Upsilon_{sl} \cdot \Upsilon_{lv}$$
<div align="right">Eq. III-2</div>

$\Upsilon_{sv}$ is the interfacial tension between the substrate and the ambient gas;

$\Upsilon_{sl}$ is the interfacial tension between the substrate and the droplet liquid;

$\Upsilon_{lv}$ is the interfacial tension between droplet liquid and the ambient gas.

If S<0 partial spreading occurs,

if S>0 complete spreading occurs. Also, in this case, the spreading may not be complete if the simultaneous drying process proceeds rapidly.

The type of the substrate material influences the spreading process and consequently the morphology of the films. Moreover, the spreading decreases if the viscosity of the solution is increasing.

### 5. Surface diffusion, Reaction

Solute decomposition and reaction can occur: (a) before landing on the substrate (when the temperature is high enough to evaporate the solvent), in this case, dry particles arrive on the substrate and grain-like structures will be obtained, (b) on the substrate (at low temperature), when droplets arrive on the substrate in liquid form, the wet chemical process leads to different morphologies, and (c) partly during the flight and partly on the substrate, partial drying of the droplets in the spray and also in the liquid will lead to layers with incorporated particles and possible porosities.

## III.2.2. Morphological control of the ESD films

A wide range of surface morphologies of a film can be achieved due to the large number of parameters which can be varied in the ESD process. Chen [83] described qualitatively the relevant deposition parameters for ESD and their influence on the morphology. He also observed that there are four main types of layer morphology: (I) dense, (II) dense with incorporated particles, (III) porous top layer with dense bottom layer, and (IV) fractal-like porous layers. These four types are schematically shown in Fig. III-2.
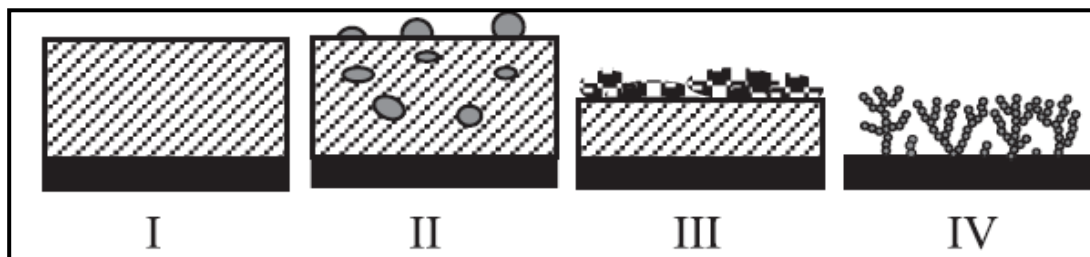


*Figure III-2: The four types of film morphologies obtained by the ESD technique.*

*A. Influence of the deposition time*

Increasing the deposition time the porosity increases also and the morphology of the layer shifts from relatively dense to porous when the deposition time is very long. Increasing the deposition time, the layer thickness increases and spreading becomes slower due to the smaller surface tension of the produced film. This leads to the deposition of small, discrete particles, which induces an increase of the surface roughness, enhancing in this way the possibility of preferential landing and agglomeration.

*B. Influence of the deposition temperature*

The temperature is the main parameter influencing the final morphology of a film. When increasing the deposition temperature, the morphology of the deposited layer changes from relatively dense to highly porous. At low temperatures the incoming droplets are large and heavy owing to less solvent evaporation and for this reason agglomeration does not happen. Upon increasing the deposition temperature more solvent evaporates and the agglomeration extent increases by increasing the effect of preferential landing. At high temperature the particles reach the substrate in dry condition and fractal-like layers are formed.

*C. Influence of the precursor solution concentration*

Chen [83] showed that the influence of the concentration on the morphology is not remarkable as long as the layer thickness is similar. A lower concentration, and hence a lower conductivity, will lead to larger primary particle size. On the other hand, the solid particle size after drying increases with the increase of the concentration.

*D. Influence of the electric field strength*

The layer obtained by applying a stronger electric field is denser than the layer formed by using a weak electric field. A shorter flight time of the droplets can be attributed to a stronger electric field. This fact results in less solvent evaporation and larger incoming droplets at the substrate surface.

*E. Influence of the solvent*

The boiling point of the solvent is very important. Using a low boiling point solvent (ethanol, 78 °C), evaporation is faster than in the case of using a higher boiling point solvent (butyl carbitol, 231 °C). Chen [83] found that layers formed using pure ethanol solutions are more porous than those formed using a mixture of butyl carbitol and ethanol.

In this work, the MOS ($SnO_2$, $ZnO$, $In_2O_3$, and $WO_3$) films were deposited using the Electrostatic Spray Deposition technique. This technique was never used to deposit films of $WO_3$ and $In_2O_3$, it was used a few times to deposit films of $ZnO$ with applications as transparent electrodes [86] but never in gas sensor applications. The $SnO_2$ films were deposited using the ESD technique by our group and used as $H_2$ gas sensor [78] but, in this work we will use $SnO_2$ and Cu-doped $SnO_2$ for the detection of $H_2S$, $SO_2$, and $NO_2$.

## III.2.3. ESD set-up

For the deposition of the films a vertical ESD set-up was used (Fig. III-3 a and b). In the ESD technique the liquid precursor is pumped by a syringe pump (Kd Scientific, model 100, USA) through a flexible tube of plastic material (Watson Marlow Marprene®, inner diameter 1.3 mm) to the tip of a stainless steel nozzle (outside diameter, 0.9 mm). When a high voltage is applied by a DC voltage power supply (FUG HCN 14-12500, Rosenheim, Germany) between the nozzle and the substrate the precursor solution is atomised into an aerosol. This aerosol, composed of highly charged droplets, is attracted by the grounded and heated substrate where they impinge and loose their charge. After complete solvent evaporation a thin layer is formed on the substrate surface. During all the layer depositions the temperature of the substrate is maintained at a constant value using a temperature control unit (Eurotherm Controls, model 2216e), which includes a heating element and a temperature controller.
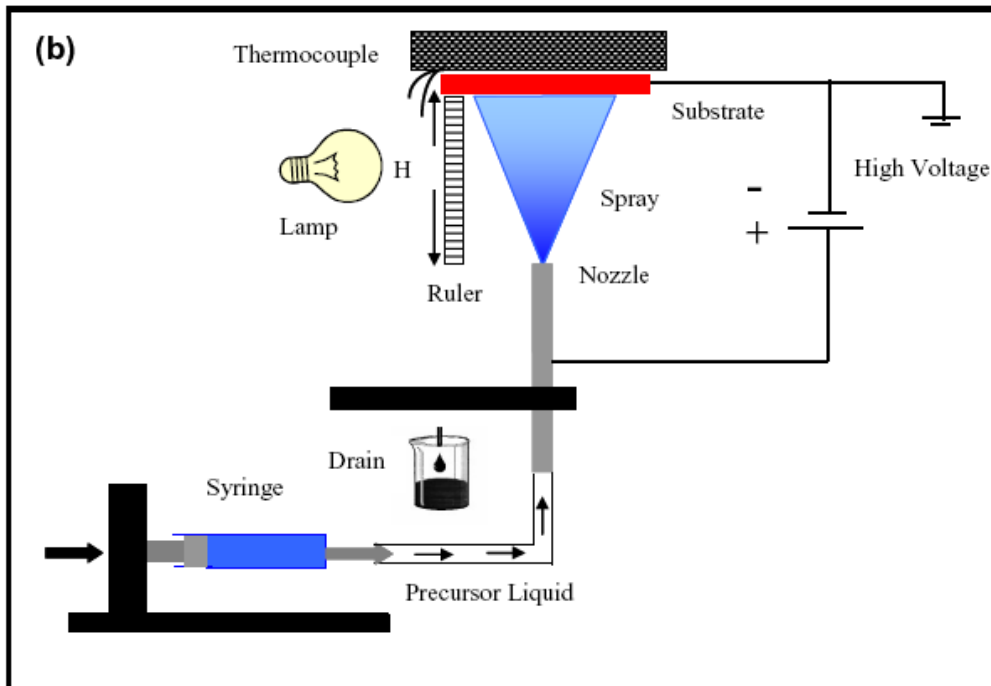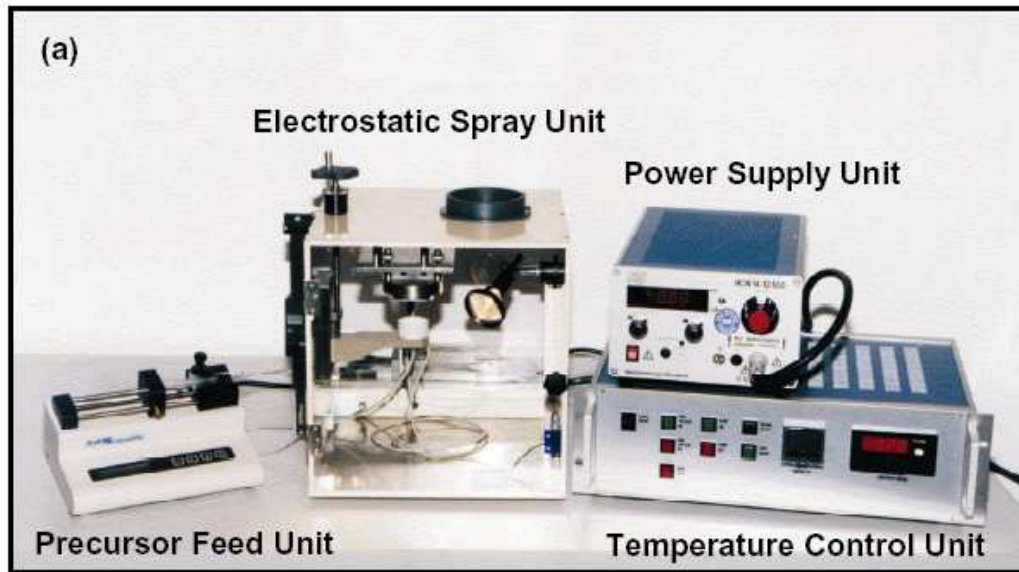
*Figure III-3: The ESD (a) experimental set-up and (b) schematical representation.*

## III.2.4. Film Deposition

The films were deposited on alumina pellets (99.7%, Gimex Technische Keramiek B.V., The Netherlands), with dimensions of 10 mm x 20 mm and a thickness of 1mm. The substrate was coated partially by a layer (1-5 µm) of platinum paste (Engelhard Clal, model 6082A) and fired at 800 °C for 2 hours in air. The distance between electrodes was 1mm. The as-made substrate was fixed in a stainless steel substrate holder, in order to allow a circular deposition surface of 10 mm in diameter (Fig. III-4). SEM pictures of the partially Pt-coated alumina can be seen in Fig. III-5.
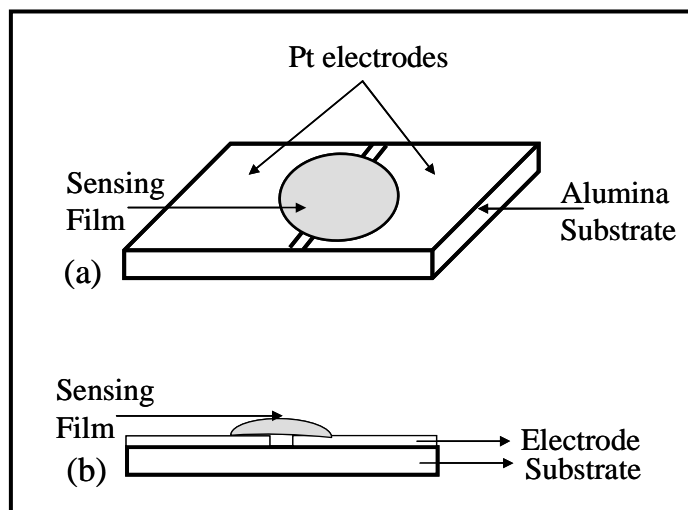


*Figure III-4: Schematic representation of a film deposited on a Pt-coated alumina substrate (a) top view and (b) cross-section view.*
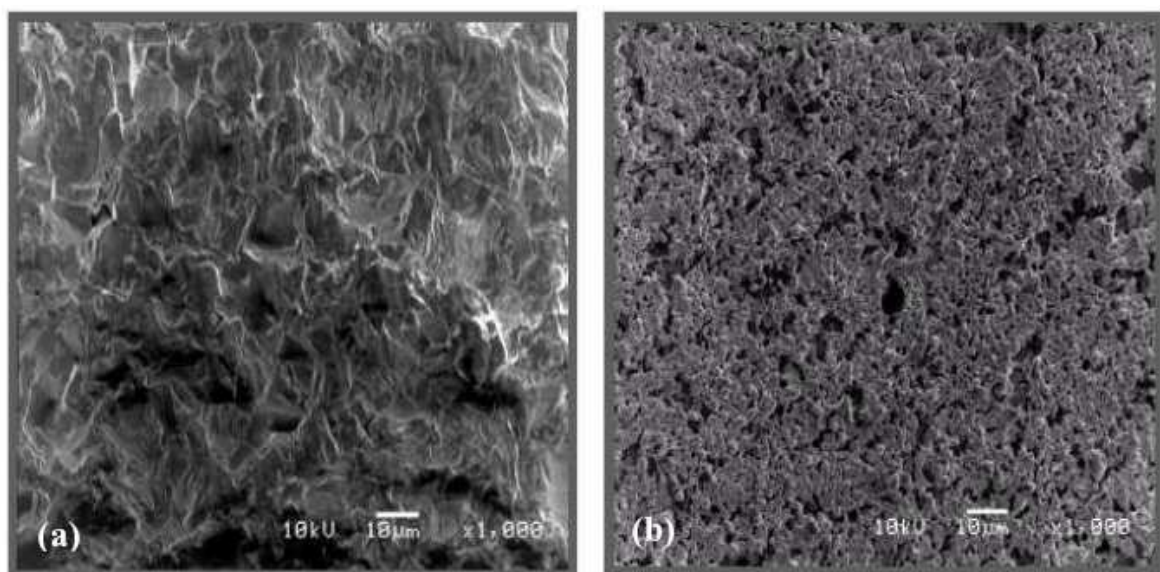


*Figure III-5: SEM picture of the substrate (a) alumina and (b) platinum.*

The precursor solutions were pumped through the metal nozzle using a flow rate of 1 to 4 ml h$^{-1}$, the temperature of the substrate varied in the range 150 to 400 °C and the deposition time between 1 and 3 hours. A distance of 20 mm was kept between the nozzle and the substrate. A positive voltage between 6.0 and 8.5 kV was applied to the nozzle breaking the liquid at the tip of the nozzle in an aerosol composed of very small droplets. Depending on the properties of the precursor solution, the flow rate of the liquid, and the voltage applied, different modes of atomization can occur [87]. In this study the experimental conditions have been adjusted to obtain the cone-jet mode, which produces droplets with a narrow size distribution. From this cone apex a thin jet is ejected which breaks up into micrometer droplets [88]. The deposition parameters used to spray the precursor solutions are presented in Table III-1.

| Precursor Solution | Flow Rate (ml/h) | Deposition Temperature (°C) | Annealing Temperature (°C) | Time (h) | Voltage (kV) |
|---|---|---|---|---|---|
| $SnO_2$ | 1-4 | 150-400 | 550 | 1-3 | 6-8.5 |
| $ZnO$ | 1-2 | 200-400 | 600 | 1-2 | 7.5-8 |
| $In_2O_3$ | 1.5 | 400 | 500 | 1 | 7.5-8 |
| $WO_3$ | 1 | 350 | 500 | 1 | 7.5-8 |

*Table III-1:  Deposition parameters used to deposit the films.*

## Solution Preparations:

### a.  $SnO_2$

Tin chloride pentahydrate ($SnCl_4 \cdot 5H_2O$, ALDRICH, 98% purity) was dissolved in absolute ethanol ($C_2H_5OH$, J.T. Baker, 99.9% purity) to obtain a 0.05 M precursor solution for depositing $SnO_2$ films. For the doping procedure a 0.05 M precursor solution of copper nitrate hydrate (Cu $(NO_3)_2 \cdot 2.5H_2O$, 98% purity, Aldrich) in ethanol was used. The dopant concentration of the films was varied from 1 to 4 at. %.

### b.  $ZnO$

For the preparation of a 0.05 M precursor solution, zincacetat-dihydrate ([Zn $(CH_3COO)_2 \cdot 2H_2O$], Merck, 99.5 % purity) in ethanol ($C_2H_5OH$, J.T. Baker, 99.9% purity) was used. A few drops of hydrochloric acid (HCl, J.T. Baker, 37-38%) were added to the solution in order to dissolve any possible precipitate of zinc hydroxide due to the reaction of ethanol with zinc acetate.

### c.  In$_2$O$_3$

The precursor solution (0.05 M) was prepared by mixing anhydrous indium chloride (InCl$_3$, Alfa Aesar, 99.9 % purity) and absolute ethanol (C$_2$H$_5$OH, J.T. Baker, 99.9% purity). A few drops of acetic acid (CH$_3$-COOH, Merck, 99-100% purity) were added to the solution to stabilize it. For the doping procedure, 0.05 M tin chloride pentahydrate (SnCl$_4$·5H$_2$O, ALDRICH, 98% purity) dissolved in absolute ethanol (C$_2$H$_5$OH, J.T. Baker, 99.9% purity) has been used. The dopant concentration of the films was fixed at 2 at. % SnO$_2$.

### d.  WO$_3$

Considering that WO$_3$ precursor salts and solutions are not stable, we have employed several methods to obtain suitable precursors to deposit WO$_3$ without impurities. Impurities will be detected after the deposition using different characterization techniques.

### 1. Tungsten Ethoxide (W(ETOH)$_6$)

First the tungsten (VI) ethoxide (W (C$_2$H$_5$O)$_6$, Alfa Aesar, 5% w/v in ethanol 99.8%) in absolute ethanol (C$_2$H$_5$OH, J.T. Baker, 99.9% purity) was used as precursor solution. The precursor is commercially available so, we had only to dilute it with absolute ethanol to obtain the 0.05 M solution.

### 2. Peroxotungstic Acid (PTA)

Tungstic acid powder (H$_2$WO$_4$, Sigma, 99%) was dissolved in an aqueous solution of hydrogen peroxide (H$_2$O$_2$, Merck, 30%) to obtain a 0.5M solution. The solution was stirred over night to dissolve all H$_2$WO$_4$ powder and to obtain peroxotungstic acid (PTA). This solution was evaporated at different temperatures (20, 60, 90 °C) in order to obtain a yellow-orange powder, which can dissolve in ethanol to obtain a 0.05 M solution. In Fig. III-6, the flowchart of the WO$_3$ deposition using the peroxo route is shown.

H₂WO₄ (tungstic acid)

↓ + 30% H₂O₂

PTA(peroxotungstic acid solution)

↓ Evaporation

PTA(peroxotungstic acid powder)

↓ + ETOH

PTE (peroxotungstic ester)

↓ Spraying
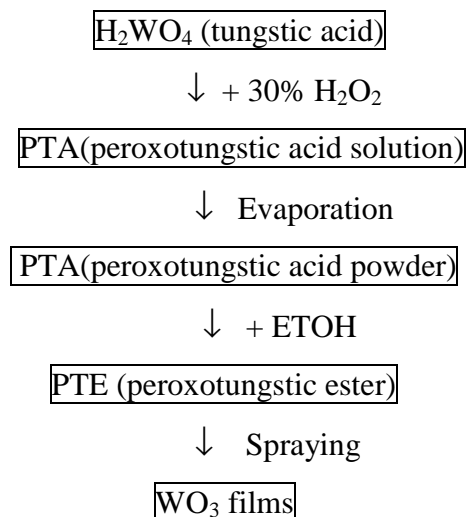
WO₃ films

*Figure III-6: Flow chart of the WO₃ film preparation using the PTA precursor.*

### 3. Tungsten Chloride (WCl₆)

To prepare a 0.05 M precursor solution, tungsten hexachloride (WCl₆, 99%, Alfa Aesar) was dissolved in ethanol (C₂H₅OH, J.T. Baker, 99.9% purity) in a glove box. The colour of the solution after preparation was yellow and it became successively green and then dark blue. Other authors [89] reported this change in colour [90],91] and they considered that the blue solution is tungsten chloride alkoxide in which W have the oxidation state V that is formed due to the reduction of W (VI) by hydrogen from the alcohol [92].

Generally, the process can be represented by the following reaction (Eq. III-3):

$$WCl_6 + x\ C_2H_5OH \rightarrow WCl_{6-x}(OC_2H_5)_x \text{ (blue)} + x\ HCl \qquad \text{Eq. III-3}$$
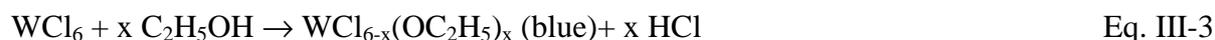
The blue solution is not very stable in air, so we tried to stabilize it by heating under reflux at 60-70 °C for 24 hours until a colourless stable solution was obtained (Eq. III-4).

$$WCl_{6-x}(OC_2H_5)_x + (6-x)\ C_2H_5OH \rightarrow W(OC_2H_5)_6 \text{ (colourless)} + (6-x)\ HCl \qquad \text{Eq. III-4}$$
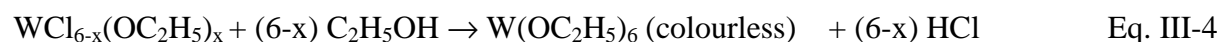
### 4. *Tungsten oxochloride (WOCl$_4$)*

The precursor solution (0.05M) was prepared in a glove box by dissolving tungsten (VI) oxychloride (WOCl$_4$, 98% Aldrich) in 2-propanol (C$_3$H$_7$OH, J.T. Baker). The solution after the preparation was yellow and after a few hours of stirring the solution became colourless. The as prepared solution is very stable and no precipitation or change in the colour were observed in time.

The reaction that took place can be represented by the following equation (Eq. III-5):

$$WOCl_4 + x\ (C_3H_7OH) \rightarrow WOCl_{4-x}(OC_3H_7) + xHCl \qquad \text{Eq. III-5}$$
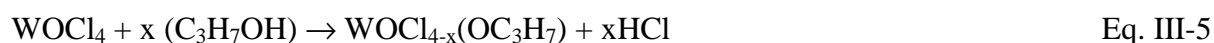
### 5. *Ammonium tungstate (NH$_4$)$_2$WO$_4$*

The precursor solution of ammonium tungstate was prepared by dissolving WO$_3$ powder (Alfa Aesar 99.8% purity) in an ammonium hydroxide solution (NH$_4$OH, J. T. Backer 25%). The solution was stirred under reflux conditions at 90°C until all the WO$_3$ powder was dissolved (Eq. III-6). A colourless solution was obtained, which is very stable. By spraying this solution at high temperatures the ammonium tungstate decomposed to tungsten oxide, ammonia and water (Eq. III-7):

$$WO_3 + 2NH_4OH \xrightarrow{\ 90°C\ } (NH_4)_2WO_4 + H_2O \qquad \text{Eq. III-6}$$

$$(NH_4)_2WO_4 \rightarrow WO_3 + NH_3 \uparrow + H_2O \uparrow \qquad \text{Eq. III-7}$$

The solutions prepared using different precursors were sprayed at 400 °C with 1ml/h during 1 hour. Considering the advantages and disadvantages of these solutions, and taking into account the structure characterization results, we have selected the best precursor solution (tungsten ethoxide), which allowed us to deposit good quality WO$_3$ films.

## III.3. MORPHOLOGY AND STRUCTURE CHARACTERIZATION

### III.3.1. Scanning Electron Microscopy and Energy Dispersive X-ray Analysis

The **Scanning Electron Microscopy** is one of the most versatile and widely used tools of modern science, which provides information about the morphology (shape, size, arrangement of the particles), the topography (determination of the surface features of an object, its texture), the compositional differences, the crystal orientation and the presence of defects. This technique can be used to determine the film thickness using a cross-sectional SEM picture. For this, a perpendicular cut of the film is necessary and furthermore, before analysis a layer of gold can be sputtered on the top of the film to provide electrical conductivity. A schematic drawing of an electron microscope is shown in Fig. III-7. The magnification of this technique is between 10 and 100 000 times [93].

The basic working principle of the scanning electron microscopy is based on the bombardment of the sample with a scanning beam of electrons to collect the slow moving secondary electrons generated by the sample. These electrons are collected, amplified, and displayed on a cathode ray tube. The electron beam and the cathode ray tube scan synchronously, so that, an image of the surface of the sample is formed.

Information about the chemical composition of the samples can be obtained using an **Energy Dispersive X-ray** spectrometer with the SEM. In this technique the X-rays emitted from a sample, under electron bombardment, are collected with a liquid nitrogen - cooled solid-state detector and analysed via a computer according to their energy. The computer programs used in EDX display an histogram of the number of X-rays detected versus the energy. The energy of the detected X-rays relates to the elements present in the sample and the intensity of the peaks is proportional to the amount of the element present in the compound. In this way qualitative analysis (identification of elements) as well as quantitative analysis (amount of each element in the sample) can be performed.

In the present work, the surface morphology and the thickness of the coatings were investigated using a JOEL JSM 580 LV Scanning Electron Microscope (SEM) and the operating voltage used was 15 kV-20 kV. To determine the film thickness the cross-sectional SEM picture was used. To obtain high-quality pictures, a thin film of gold was sputtered (using an Edwards Sputter Coater S150 B) on the layer surfaces in order to provide electrical conductivity.

The chemical analysis of the thin films was investigated using an Energy Dispersive X-ray analyser, Link ISIS, (Oxford Instruments, U.K.). The system was operating at 10 kV and 80-100 mA, the collection time was 1 min and the working distance was set to 10 mm.
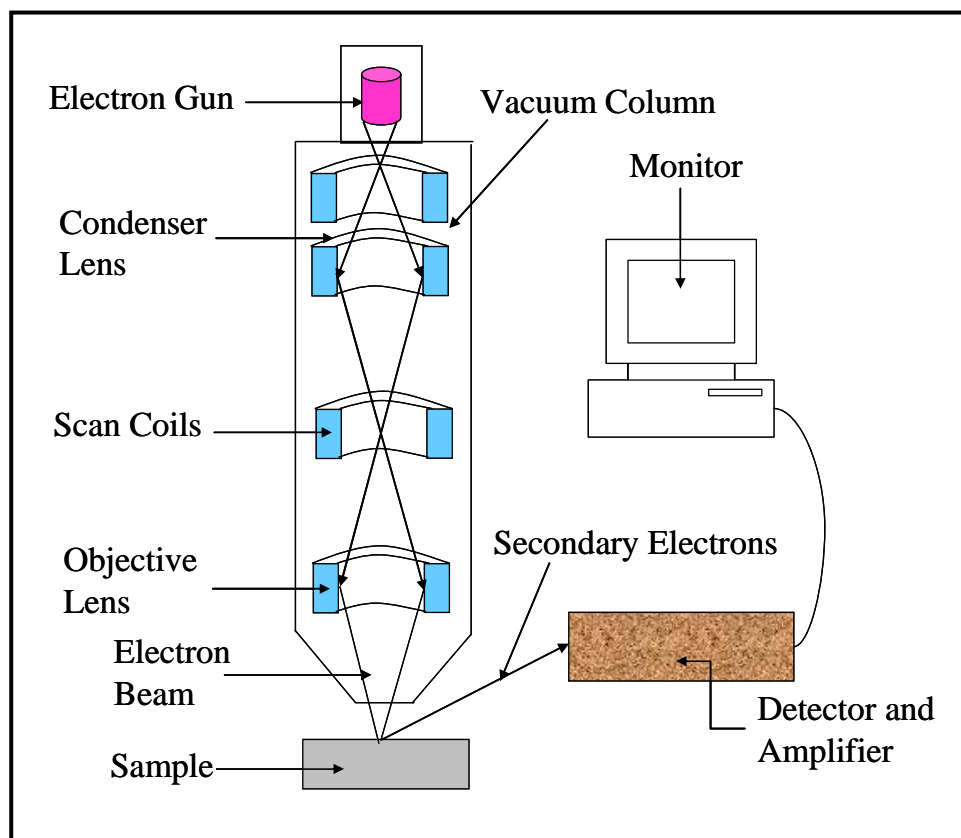


*Figure III-7: Schematic view of a Scanning Electron Microscope.*

## III.3.2. Transmission Electron Microscopy

Transmission Electron Microscopy is a technique related to SEM but the magnification is much higher (2 000-450 000X) which is a great advantage to study the samples down to their atomic level, and to determine the size and shape of the particles. In contrast with SEM, the sample preparation using TEM is destructive, requiring the milling in order to reach a submicron thickness necessary for the transmittance of the electrons through the sample. TEM is a more expensive technique than SEM, requiring both high vacuum and a high voltage electron gun to enable the electrons to penetrate the sample.

The TEM working principle can be described as follow: the electron beam is generated in an electron gun (heated tungsten filament). The electrons are accelerated towards the anode by applying a high voltage between the anode and the cathode (gun). The accelerated beam is focused by a condenser lens and travels through the specimen, where the objective lens

produces the primary magnified image of the specimen. A series of projector lenses further enlarges this image, which is displayed on a fluorescent screen, or recorded photographically or digitally. As SEM, the TEM can be connected to an energy dispersive X-ray analyzer.

The Transmission Electron Microscopy measurements were performed using a PHILIPS CM30T electron microscope with a filament of $LaB_6$. The system is operating at 300 kV. The samples are placed on quantifoil carbon polymer supported on a gold or copper grid by applying a few droplets of a ground sample in ethanol, followed by drying in air. The chemical composition of the thin films was investigated using an Energy Dispersive X-ray analyser, Link Isis, (Oxford Instruments, UK).

## III.3.3. X-ray Diffraction

The X-Ray Diffraction is a versatile technique used in different application fields to analyse crystalline materials, to do a nondestructive analysis of bulk samples, powders, single crystals, and thin films.

Samples can be analysed with an X-ray diffractometer in order to determine the crystal lattice parameters, changes in phase or lattice parameters before and after thermal treatment, strain and composition of thin films and the amount of each phase present in a sample.

In X-ray diffractometry, X-rays are generated within a sealed X-ray tube under vacuum. A current is applied to heat a filament in the top of the tube; the higher the current is the greater the number of electrons emitted from the filament is. A high voltage is applied within the tube (10 –100 keV) and accelerates the electrons, which then hit a target, commonly made of copper, cobalt, iron or molybdenum. When these electrons reach the target, X-rays are produced and they are collimated and directed onto the sample. A detector receives the X-ray signal, which is then processed either by a microprocessor or electronically, converting the signal to a count rate. The results of this analysis are described graphically as a set of peaks with intensity on the y-axis and the diffraction angle on the x-axis.

When an X-ray beam hits a sample and is diffracted, the distances between the planes of the atoms of the sample can be obtained by applying Bragg's Law (Eq. III-8):

$$n\lambda = 2d\sin\theta \qquad\qquad\qquad\qquad \text{Eq. III-8}$$

Where n is the order of diffracted beam and it is an integer (1, 2, 3…); $\lambda$ is the wavelength of the incident X-ray beam; d is the distance between adjacent planes of atoms; $\theta$ is the angle of incidence of the X-ray beam and the atomic plane. A schematic representation of Bragg's law can be seen in Fig. III-8.

Since we know $\lambda$ and we can measure $\theta$, we can calculate the d spacing. The characteristic set of d spacings generated in a typical X-ray scan provides an unique "fingerprint" of the material comprising the sample. When properly interpreted, by comparison with standard reference patterns and measurements, this "fingerprint" allows the identification of the material. Computer "search-match" algorithms are used to compare experimental pattern with JPCDS (International Centre for Diffraction Data) database of known compounds.
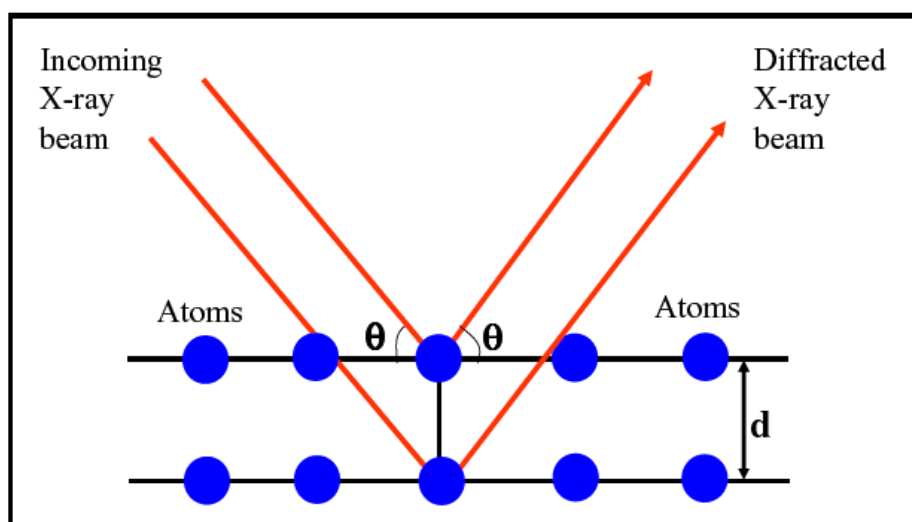


*Figure III-8: Schematic representation of Bragg's law.*

Besides the material identification (qualitative analysis), the XRD method can be used also for quantitative analysis, i.e., to determine the crystallite size of a material by using Scherrer's formula (Eq. III-9) [94]:

$$t = k\lambda/\beta\cos\theta \qquad\qquad\qquad\qquad \text{Eq. III-9}$$

Where t is the averaged dimension of the crystallite (nm), $\lambda$ is the radiation wavelength (0.15406 nm for Cu $K_{\alpha}$), $\beta$ is the full-width at half maximum height (FWHM) of the X-ray line (radians), and $\theta$ is the diffraction peak angle.

In the present work, the crystal structure of the films was determined with a BRUKER D8 ADVANCE X-ray diffractometer (XRD) using a monochromatic Cu-K$_\alpha$ radiation ($\lambda$ = 1.5406 Å) with operating voltage of 40 kV and current of 40 mA.

### III.3.4. Raman Spectroscopy

Raman spectroscopy is an invaluable technique, which offers non-destructive qualitative (identification) and quantitative (particle size determination) microanalysis of materials. The Raman effect arises when the incident light excites molecules in the sample, scattering subsequently the light. While most of this scattered light is at the same wavelength as the incident light (Raleigh scatter), some part is scattered at different wavelengths (Raman scatter) (Fig. III-9). This inelastically scattered light is called Raman scatter. It results from the molecule changing its molecular motions. The energy difference between the incident light (Ei) and the Raman scattered light (Es) is equal to the energy involved in changing the molecule's vibrational state (i.e., getting the molecule to vibrate, Ev). This energy difference is called the Raman shift (Eq. III-10).

Ev = Ei – Es                                                                           Eq. III-10

Several different Raman shifted signals will often be observed, each signal being associated with different vibrational or rotational motions of molecules in the sample. The particular molecule and its environment will determine which Raman signals will be observed. A plot of Raman intensity versus Raman shift represents a Raman spectrum.
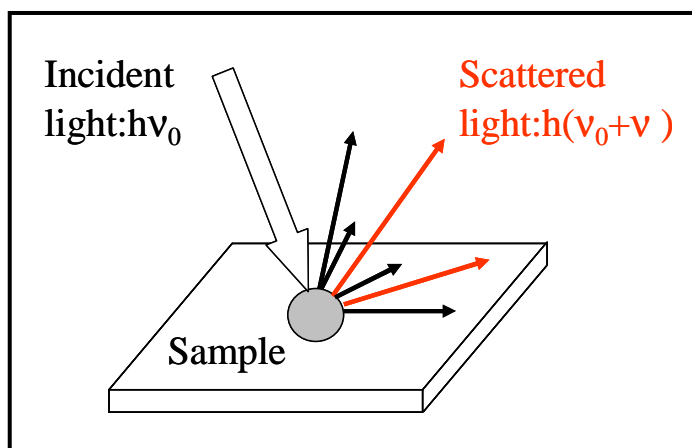


*Figure III-9: The representation of the light scattering.*

Raman measurements were performed at room temperature using a home-built set-up (Fig. III-10). The excitation source used is an $Nd:YVO_4$ laser system (SPECTRA PHYSICS MILLENNIA), which provides a wavelength of 532 nm. The spectra were recorded in the back-scatter mode using a liquid-nitrogen cooled CCD camera (PRINCETON INSTRUMENTS LN/CCD-1100PB) connected with a Spex 340E monochromator. The monochromator is equipped with an 1800 grooves/mm grating. The CCD chip is controlled by a Princeton Instruments ST-138 controller, which is connected to a personal computer running with WinSpec software. The laser beam power on the sample was limited to ~ 2mW in order to prevent heating of the samples. The scattered light was removed effectively by two notch filters (KAISER Optical Systems). The Raman shift was corrected before each measurement using a silicon reference sample and spectrum.
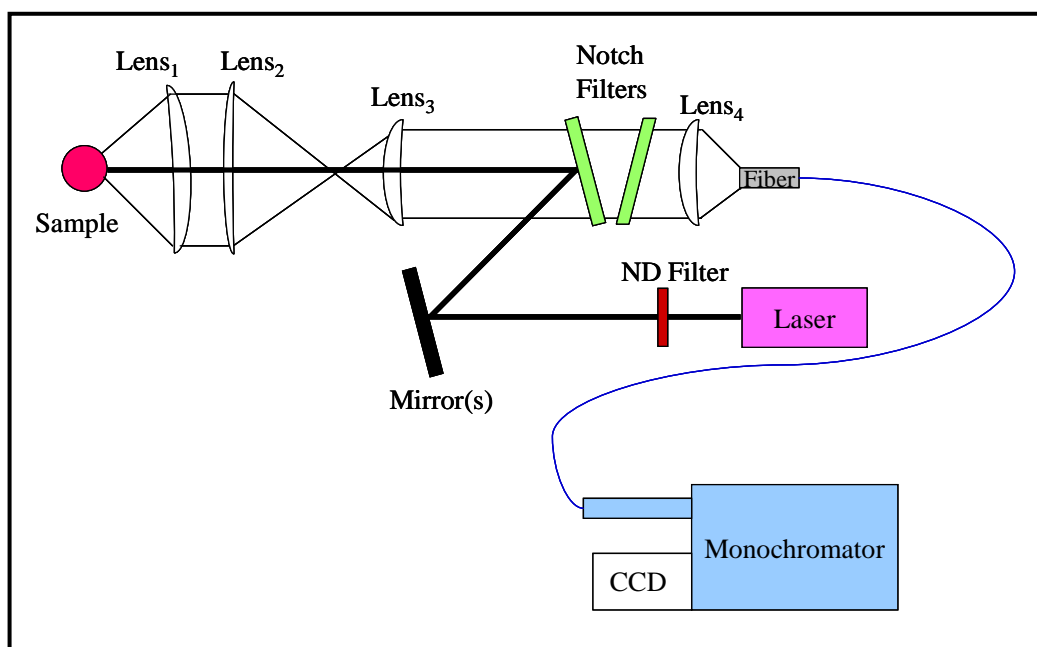


*Figure III-10: Schematic representation of the Raman Set-up.*

## III.4. GAS SENSOR TEST SYSTEM AND WORKING PROCEDURE

### III.4.1. Experimental Test System

The gas sensor measurements were carried out in a closed quartz tube furnace (HERAEUS, type ROK 3130, Thomson Holland). Two samples were placed in the furnace and then studied. The temperature was measured using a type K thermocouple (Nickel-Chrome/Nickel-Aluminium) and controlled by a PID temperature regulator (JUMO dTRON 16.1, France). The sample resistance measurements were performed using two Pt wires using the two-point probe method with an Electrometer (KEITHLEY 6514, USA). The experimental set-up and its schematic representation are shown in Fig. III-11 and 12.
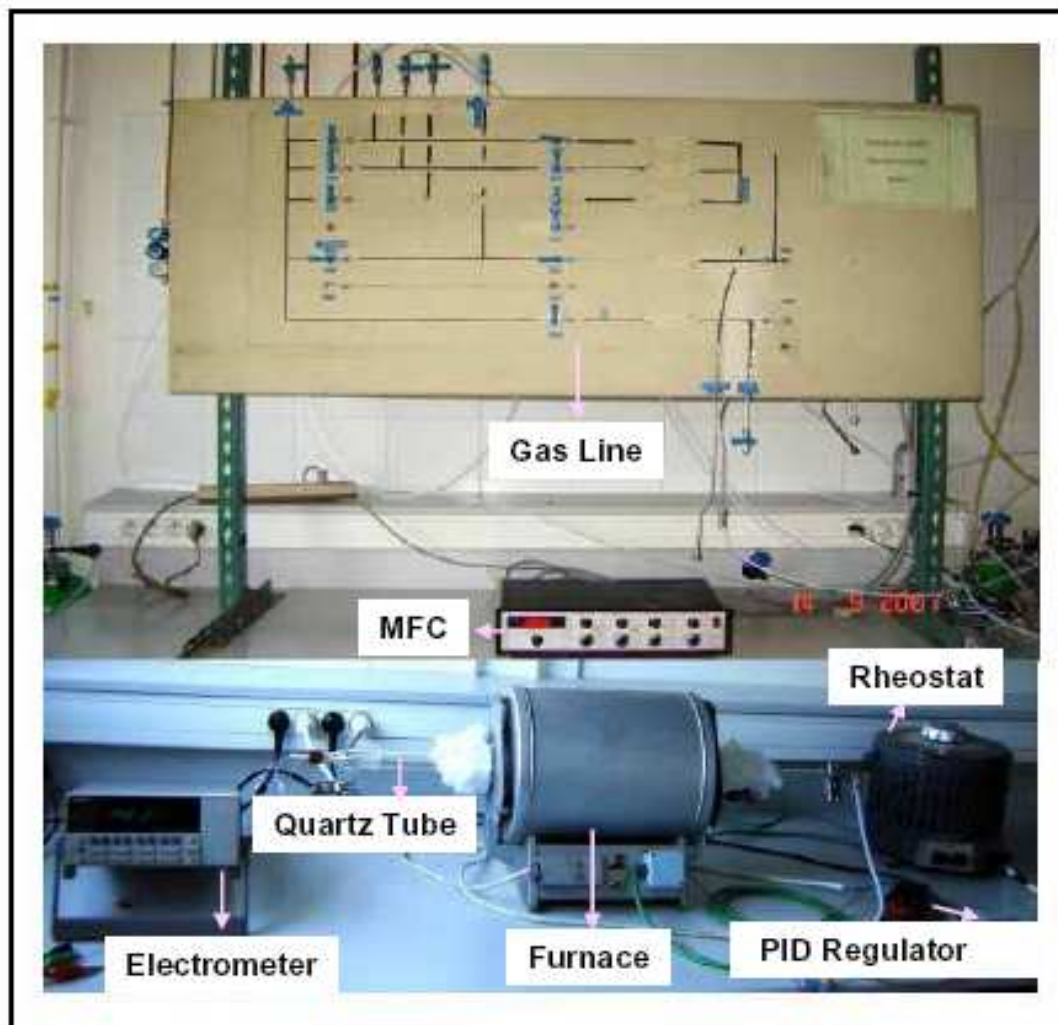


*Figure III-11: Gas sensor experimental set-up used in this study.*
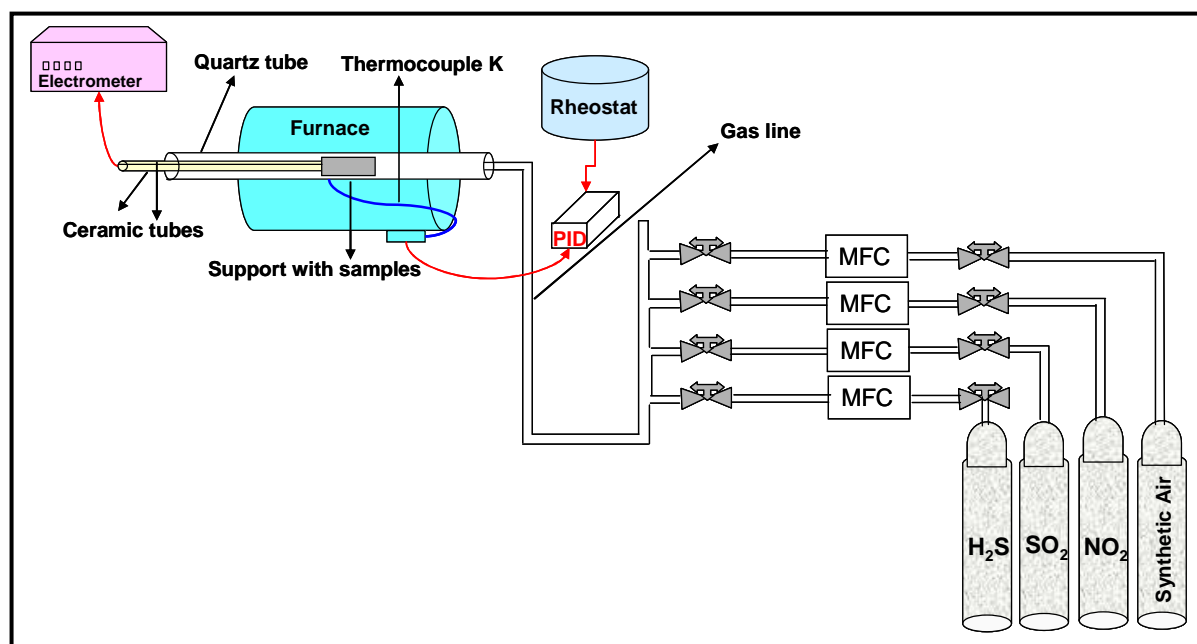
*Figure III-12: Schematic representation of the gas sensor experimental set up.*

The quartz tube is connected to the gas line allowing the gas passage. The concentration of the gases was fixed by adjusting the flow rates of the target gas and the carrier gas (synthetic air) in such a way to maintain a total constant flow rate of 100 ml/min. The gas bottles were provided by Air Products (France) and the concentration of the gases was controlled using mass flow controllers (MFC, BROOKS Instruments, 5850 TR). The compositions and the concentrations of the bottles are listed in Table III-2.

| Gas | Composition |
|---|---|
| Synthetic Air | 20% oxygen + 80% nitrogen |
| Hydrogen sulphide | 100 ppm $H_2S$ in synthetic air |
| Sulphur dioxide | 100 ppm $SO_2$ in synthetic air |
| Nitrogen dioxide | 100 ppm $NO_2$ in synthetic air |

*Table III-2: Gas bottle compositions.*

## III.4.2.  Working Procedure

Before starting the measurements the film resistance was stabilized in air by repeated temperature cycles between 100 and 450 °C, approximately 7 cycles.

**Experimental conditions:**

- ➢ The gas flow was fixed at 100 ml/min for all the measurements
- ➢ The gas exposure time was 30 min in order to ensure the stability of the response
- ➢ The synthetic air exposure was 1 hour to provide a good regeneration of the films
- ➢ The gas concentrations used in the work are shown in Table III-3

The first consideration in the selection of the gas concentrations was to do not exceed the maximum allowed limit in the atmosphere (i.e., 10 ppm for $H_2S$, 20 ppm for $SO_2$, and 5 ppm for $NO_2$). The second consideration was to use a concentration high enough in order to have a sensor response for the entire studied temperature range.

| Type of gas | Concentration (ppm) |
|:---:|:---:|
| $H_2S$ | 1; 4; 7; 10; 12 |
| $SO_2$ | 20 |
| $NO_2$ | 0.25; 0.5; 0.75; 1 or 1; 2; 3; 4; 5 |

*Table III-3: Gas concentrations used in this study.*

### III.4.2.1.  Response as a function of the temperature

To determine the optimum operating temperature the gas sensor was exposed to a fixed concentration of $NO_2$ or $H_2S$ and the temperature was changed between 50 and 450 °C by steps of 50 °C depending on the studied films (Table III-4). The temperature ranges were chosen taking into account the results presented in the literature. For the reducing gases a concentration of 10 ppm has been selected for $H_2S$ and only for ZnO it was used 12 ppm, considering the low response to this gas. For $SO_2$ a higher concentration (20 ppm) than $H_2S$ was chosen because all metal oxides used in this work offer generally a very small response to $SO_2$.

Taking into account that the resistance of the films in synthetic air is quite high (order of Mega or Giga ohm), for the oxidising gas $NO_2$ a concentration of 1 ppm was selected to study the response as a function of the temperature in order to avoid to measure a too high resistance during the gas exposure.

For each day of measurements the temperature was set to a certain value between 100 and 300 °C. Before starting the measurements for one day the films were regenerated with synthetic air during 60 min and then exposed to the pollutant gas for 30 min. This cycle was repeated 4 or 5 times during a day and then the next temperature was set for the following day. The same procedure was followed every day until all the ranges of temperatures were explored.

| Type of film | Temperature (°C) |
|:---:|:---:|
| $SnO_2$ | 100-300 |
| $ZnO$ | 200-450 |
| $In_2O_3$ | 100-300 |
| $WO_3$ | 50-300 |

*Table III-4: Temperature ranges used in this study.*

### III.4.2.2.  Response as a function of the concentration

The relation between the gas response and the gas concentration was evaluated at a fixed temperature (i.e., optimum operating temperature) by changing the $H_2S$ concentration between 1-10 ppm and the $NO_2$ concentration between 0.25-1 ppm or 1-10 ppm depending on the film resistance (if the film resistance during gas exposure is very high, it is preferred to work with very low gas concentrations). During a day the film was exposed a few times to a fixed concentration of pollutant gas ($H_2S$ or $NO_2$) followed by regeneration with synthetic air and this operation was repeated daily until all the concentration ranges were studied.

## III.5.   CONCLUSIONS

Theoretical aspects of the ESD technique used to deposit the films have been first presented. It was observed that the temperature is the parameter which has the greatest influence on the morphology, compared to the other deposition parameters.

The experimental details of the precursor solution preparation, parameters used for the film deposition, and the characterization methods have also been presented. The techniques (SEM, XRD, TEM, and Raman Spectroscopy) used to characterize the film morphology and microstructure are described in this chapter and it is concluded that all the techniques are useful to obtain sufficient information in order to select the suitable layers for gas sensor applications.

The final part of the chapter is devoted to the gas sensing measurement system and the working procedure used to study the sensor performance as a function of the operating temperature and the gas concentration.

# CHAPTER IV:

## GAS SENSORS BASED ON TIN OXIDE

# IV.  GAS SENSORS BASED ON TIN OXIDE

## IV.1.  INTRODUCTION

$SnO_2$ is an interesting material due to its potential application in solar cells [95] as conductive transparent electrode [96], in transistors [97], in varistors [98], and in different kinds of sensors [99-101]. Over the time, tin oxide proved to be the most widely used semiconductor oxide gas sensor, which can detect a wide range of pollutant gases [101-104].

A major drawback of $SnO_2$ and metal oxide-based gas sensors is the lack of selectivity, which limits its further applications when each gas must be detected in a mixture of gases. To overcome this drawback different strategies have been employed. It is well known that the sensitivity and selectivity of $SnO_2$ can be improved by adding small amounts of dopants. For example, the sensitivity of $SnO_2$ to $H_2$ is improved by doping with $In_2O_3$ [105] and the sensitivity to $O_2$ by doping with $Ga_2O_3$ [106]. Particularly the performance of $SnO_2$ in the detection of $H_2S$ has been improved greatly by the addition of small amounts of $CuO$ [107]. For example, $CuO$ has been introduced into $SnO_2$ as dopant [108], as additive [107], but heterostructures [109] or sandwich structures [36] have been also reported.

$SnO_2$ or doped-$SnO_2$ thin films have been deposited using different techniques, such as spray pyrolysis [110], sol-gel process [111,112], Chemical Vapour Deposition [113], sputtering [114], pulsed-laser deposition [115]. In this study the ESD technique is used for the deposition of $SnO_2$ and Cu-doped $SnO_2$ films [79] in order to detect $H_2S$, $SO_2$, and $NO_2$. This technique has been before used by our group for the deposition of $SnO_2$ and $Mn_2O_3$-$SnO_2$ with applications as $H_2$ sensor [78,116].

The first goal of this work is to prepare porous thin films of $SnO_2$ using the ESD technique. To optimize the $SnO_2$ film deposition process the parameters such as temperature, time, flow rate were changed and the morphology and microstructure of the films were studied with different characterization techniques. After a detailed analysis of the films, the parameters which yielded porous, adherent, and thin films have been selected.

As mentioned above, the performances of $SnO_2$ films in the detection of $H_2S$ are considerably improved by doping with copper oxide. So, the second focus of this chapter is doping the $SnO_2$ films with different amounts of copper (1, 2 and 4 at. % Cu) in order to improve especially the sensitivity to $H_2S$ but also to $SO_2$ and $NO_2$. The selection of the copper dopant and its concentrations in $SnO_2$ was done considering the literature results which show good sensing properties by doping $SnO_2$ with small amounts between 1 and 5 wt. or at.% copper [108,117,118].

The film response to $H_2S$ is first studied as a function of the operating temperature in order to select the optimal working temperature, which yields the maximum $H_2S$ sensitivity. This temperature is used further to determine the sensor response in function of the $H_2S$ gas concentration and also to evaluate the cross-sensitivity to the other gases, i.e., $SO_2$ and $NO_2$.

## IV.2.   RESULTS AND DISCUSSIONS

### IV.2.1.Morphology and Structure Characterizations

#### IV.2.1.1.   Scanning Electron Microscopy

The influence of the deposition temperature, time and flow rate on the morphology of the films is presented. Firstly, the temperature parameter is studied because of its greatest influence on the film morphology.

### A.  Deposition Temperature Effect

The $SnO_2$ morphology changes as a function of the substrate temperature (Fig. IV-1) were first studied. If the film is deposited at 150 °C (Fig. IV-1 a) the droplets arriving at the substrate do not evaporate immediately on the surface and a dense smooth film is formed. Nevertheless, the film presents cracks, probably caused by thermal stress built-up during the drying process of the film in air.

In the same experiment repeated at 250 °C (Fig. IV-1b) the film is dense and composed of large particles with almost regular shape and size (about 2 μm). Few small cracks only are observed in this case.

If the deposition temperature is at 350 °C and at 400 °C (Fig. IV-1c and Fig. IV-1d) a porous layer is formed due to the fast growth rate. In the films are many agglomerates of particles with irregular shape and their sizes are about 0.5-1.5 μm, respectively, of 0.2 -1 μm for 350 °C, respectively, 400 °C as deposition temperature.

As it can be seen (Fig. IV-1) with the increase of the deposition temperature the particle sizes decrease, while the porosity and roughness vary inversely.

Porous films with small particle size are preferred because they offer a large sensible surface for the gas detection. To increase the adsorption of the gas and to improve the sensor properties, the deposition temperature of 400 °C (Fig. IV-1d) was selected as an optimal deposition temperature.

## B. Deposition time effect

The effect of the deposition time (1h and 3h) on the morphology of the $SnO_2$ films has also been studied.

Fig. IV-2a shows that the films deposited in 1h exhibit a porous morphology with small agglomerates of about 1μm, which are uniformly distributed. If the film is deposited during 3h (Fig. IV-2b), the porosity of this film increases, offering a fractal-like structure with uniformly distributed agglomerates and sizes (about 10-20 μm). Changing the porosity by increasing the deposition time can be explained by the fact that, in the first case (1h deposition time), the particles arriving at the substrate are spreading easily on the alumina substrate, and therefore a denser layer compared with the second one (3h deposition time) is formed. When the deposition time increases, the arriving droplets have to spread on the surface of the already deposited layer and discrete particles are formed, which increase the roughness, and lead to a more porous morphology. This type of morphology would be preferred for our sensing application but unfortunately it presents the disadvantage of poor adhesion to the substrate, fact also observed by Chen et al. [119]. In this way a compromise between porosity and adhesion must be obtained in order to have good quality $SnO_2$ thin films, so, the shorter deposition time (1h) is selected to deposit the layers.
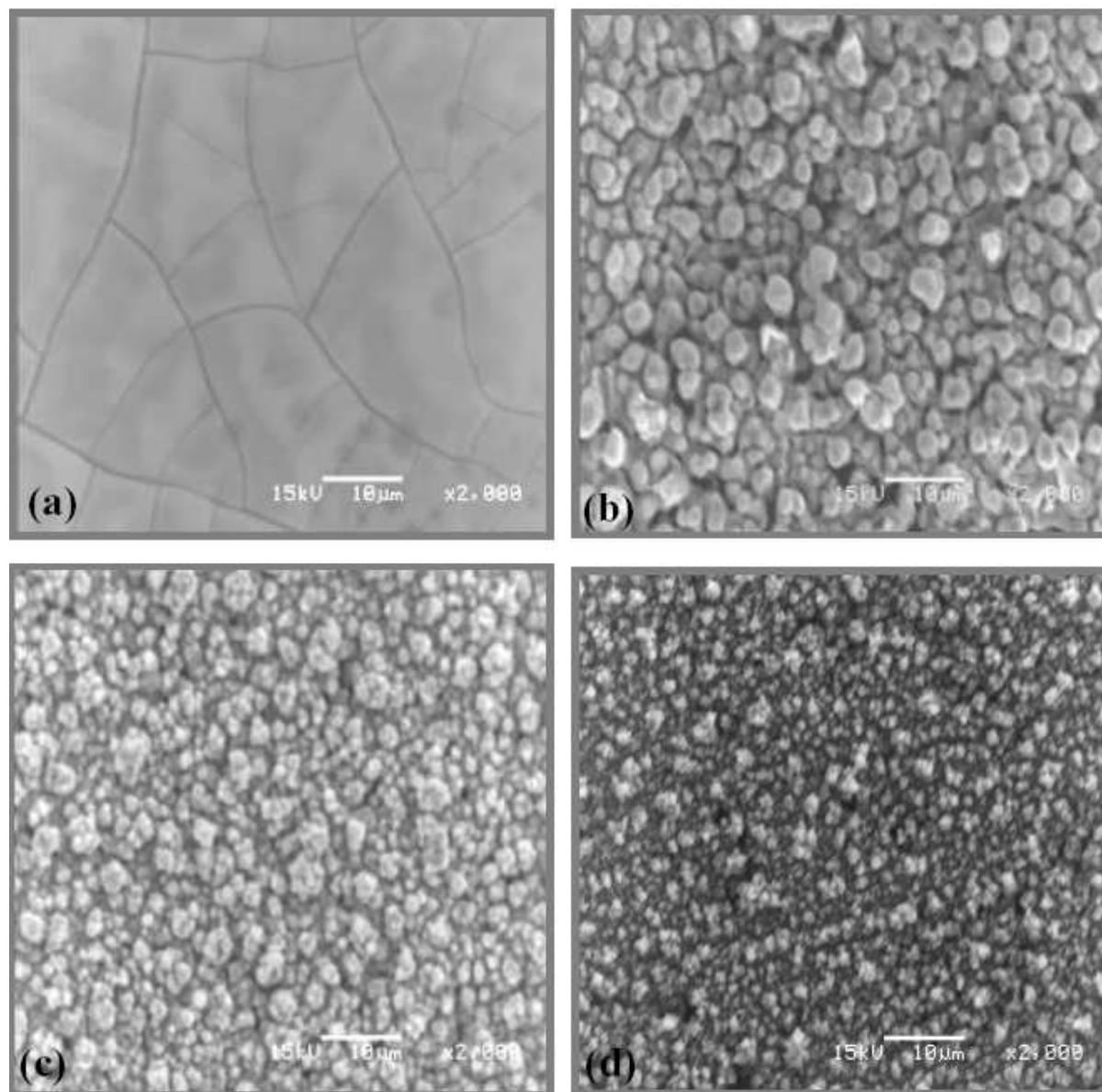
*Figure IV-1: SEM pictures of SnO$_2$ films deposited with 1ml/h for 1h using different deposition temperatures: (a) 150°C, (b) 250°C, (c) 350 °C, (d) 400 °C.*

Fig. IV-2a' shows that the films deposited in 1h have a thickness of 5-6 $\mu$m as determined using the film SEM cross-sectional photo. When increasing the deposition time up to 3h the layer thickness increases to 20-25 $\mu$m (Fig.IV-2b').

So, it can be noted that if the deposition time increases, the porosity, the agglomerate size, and the film thickness increase as well.

### C. Flow rate effect

Fig.IV-3 presents the SEM pictures of the $SnO_2$ layers deposited at 400 °C, using a flow rate range from 1ml/h to 4ml/h.

For a low flow rate (Fig. IV-3a, b) porous films are formed due to the fact that the particles arriving at the substrate are dry or semi-dry and they slightly spread over the substrate. The films deposited using 1ml/h respectively 2ml/h flow rates comprise agglomerates with sizes of about 1$\mu$m respectively 1-5$\mu$m, which are uniformly distributed. The shape of the agglomerates is irregular suggesting that the films are porous. When high flow rate of 4ml/h is used, the droplets landing on the substrate are still wet, they are spreading over the substrate and a denser film is formed (Fig.IV-3c) comparing with the first two cases. This film comprises uniform distributed agglomerates (sizes between 1-5$\mu$m), which have regular shape, and some small crakes can be noticed.

It can be concluded that the porosity decreases with the increase of the flow rate of the precursor solution while the size of the particles increases.

The parameters, which lead to a porous morphology as well as a good adherence, an entire coverage of the substrate, and an uniformity of the film aggregates, are selected for the copper doping procedure. We have prepared 5 films along with these conditions (temperature 400°C, deposition time 1h and flow rate 2ml/h) in order to ensure reproducibility (Fig. IV-3b).

The morphology studies of this layer show a porous structure in which the particles are present in aggregates. These agglomerates are uniformly distributed, with a 1-5 $\mu$m diameter range. The thickness of the film determined using the cross-sectional SEM picture (Fig. IV-3d) is about 7-8 $\mu$m.
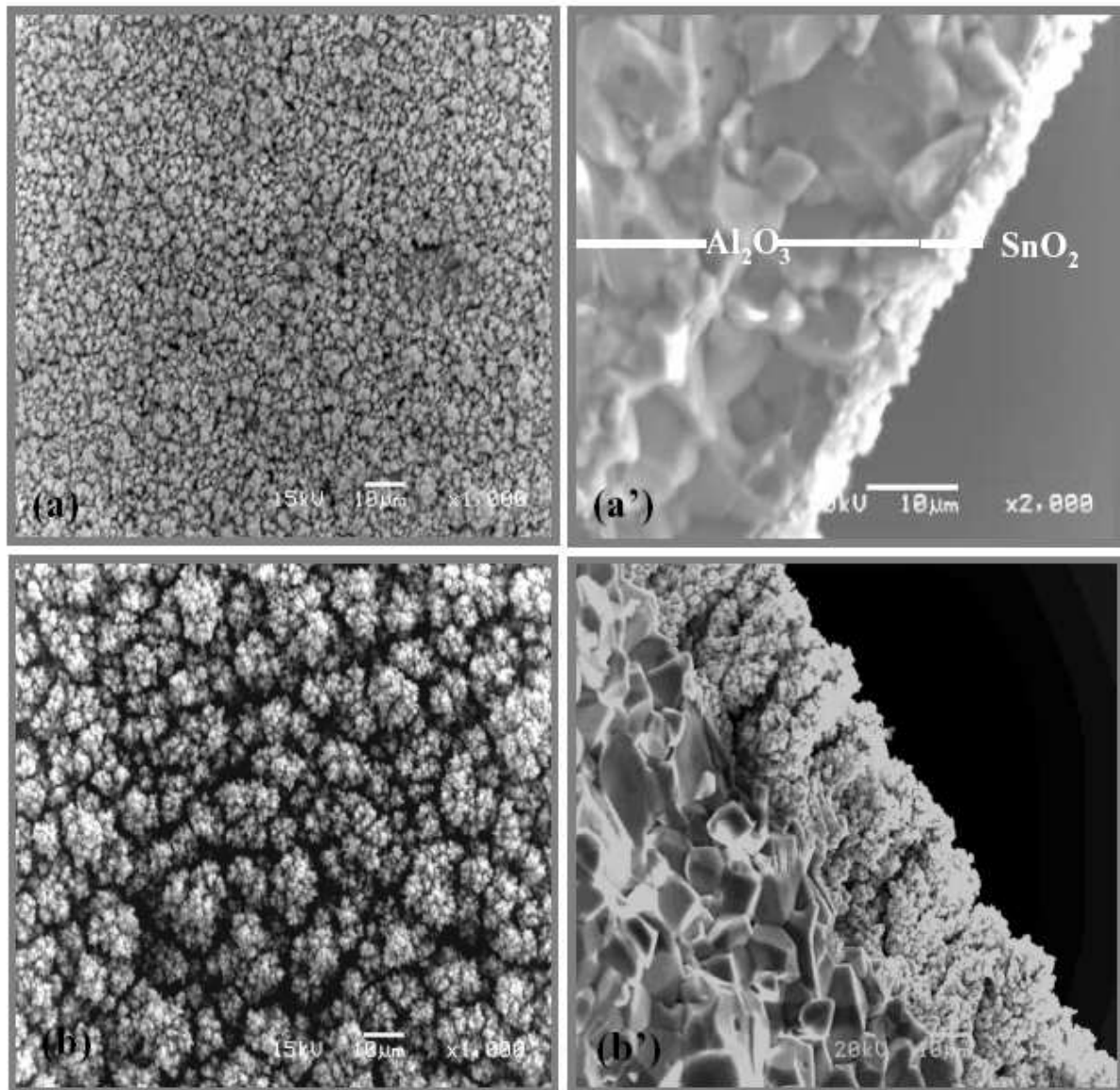
*Figure IV-2: SEM pictures of SnO₂ films deposited with 1ml/h at 400 °C using different deposition times: (a) 1h-top view (a') 1h-cross section, (b) 3 h-top view, (b') 3h-cross section.*
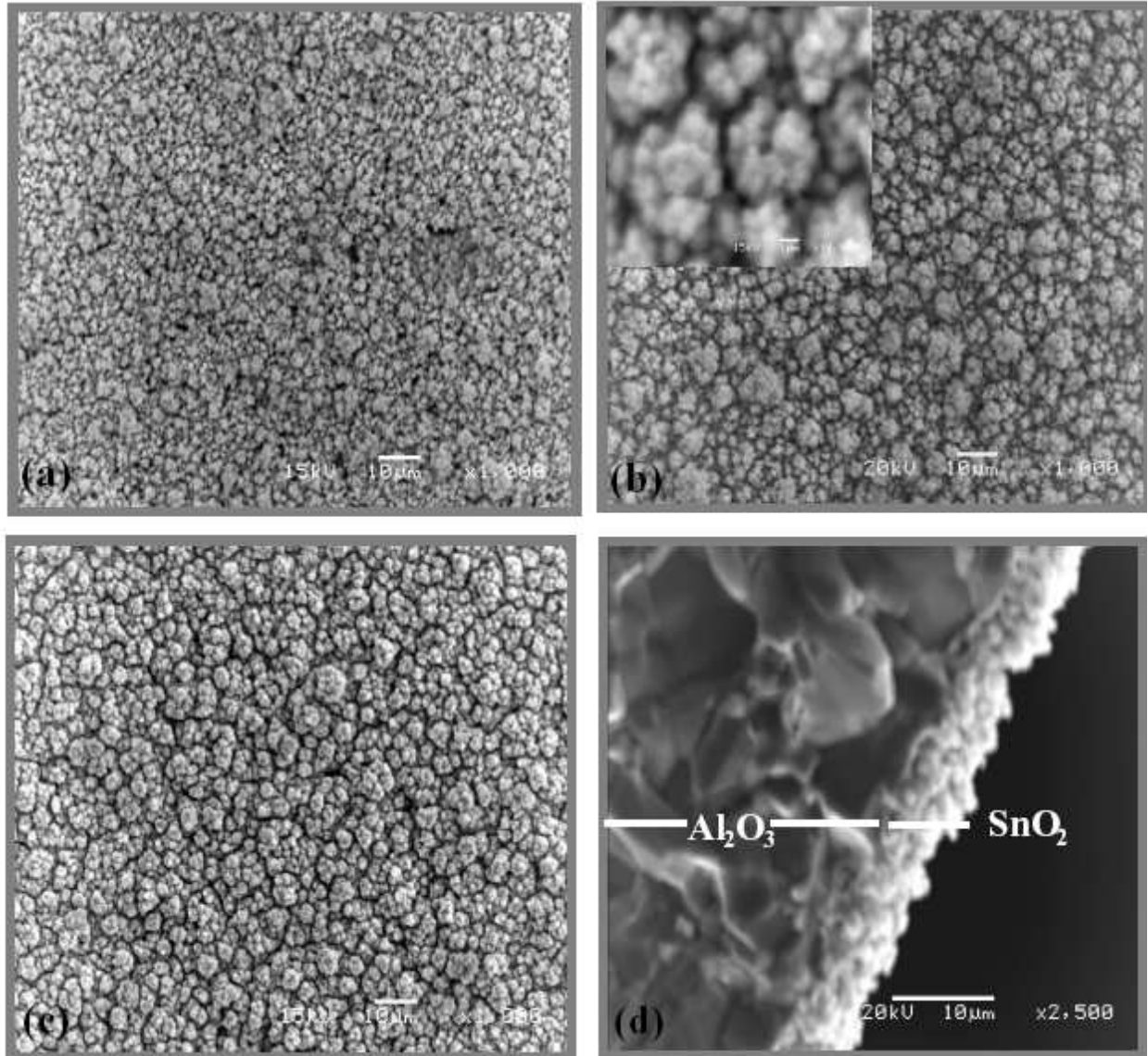
*Figure IV-3: SEM pictures of SnO₂ films deposited at 400 °C for 1h using different precursor solution flow rates: (a) 1ml/h, (b) 2ml/h-top view, (c) 4ml/h, (d) 2ml/h-cross-section.*

### D. Copper doping effect

The influence of the Cu dopant (1, 2 and 4 at. % Cu) on the morphology of the films is studied and the SEM pictures are shown in Fig. IV-4. These pictures show that the doping process has no significant influence on the morphology. All the films present porous morphology made of aggregates with uniform sizes. Comparing $SnO_2$ SEM pictures (Fig. IV-4 a) and Cu-doped $SnO_2$ ones (Fig. IV-4 b-d) we can remark a small decrease in the porosity and in the aggregate size along with the increase of the copper dopant amount.
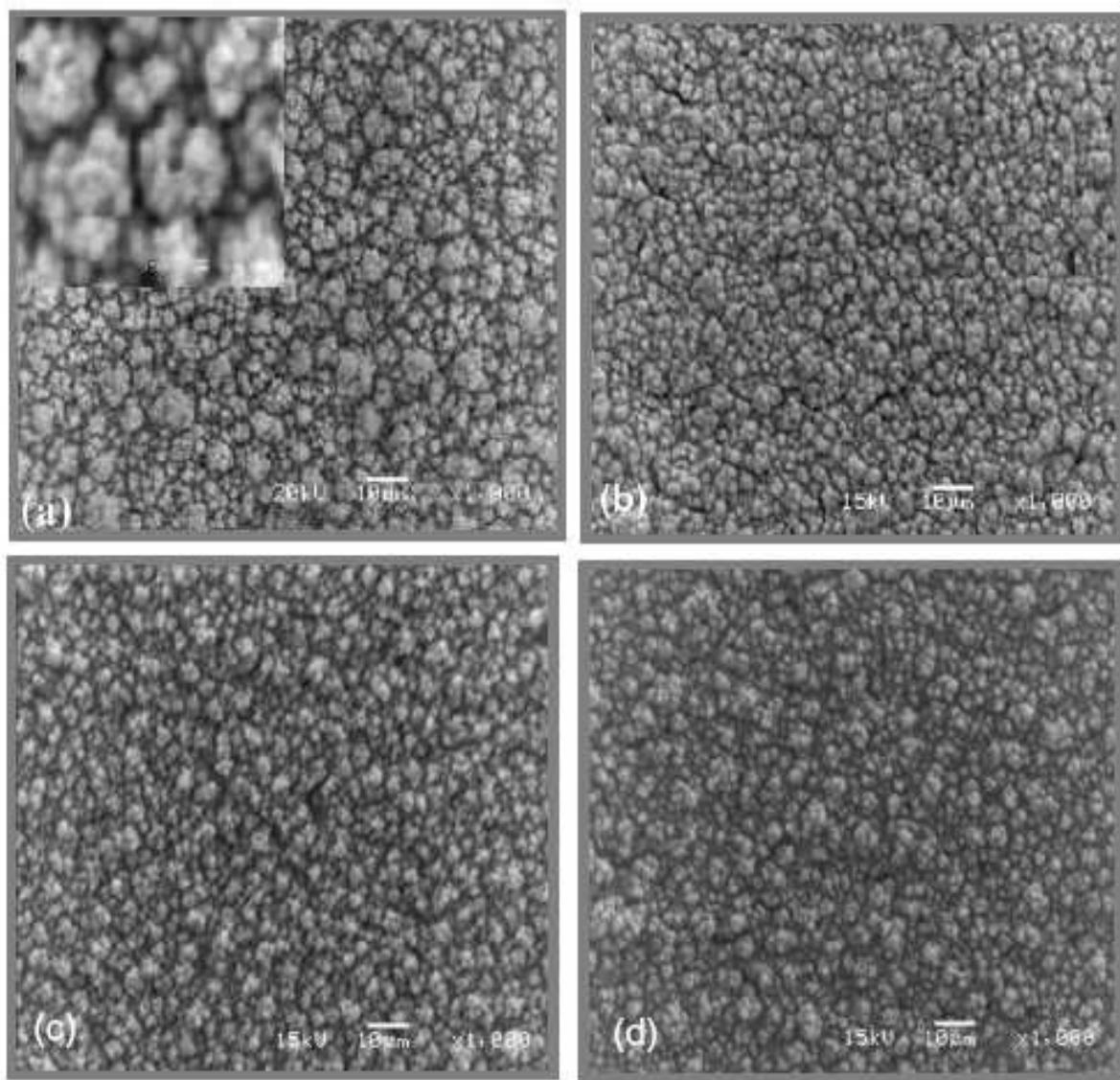


*Figure IV-4: SEM pictures of (a) SnO₂, (b) 1 at. % Cu-doped SnO₂ (c) 2 at. % Cu-doped SnO₂ and (d) 4 at. % Cu-doped SnO₂.*

### IV.2.1.2. X-ray Diffraction

The XRD measurements were performed on undoped and Cu-doped $SnO_2$ before and after annealing. The as-deposited films at 400 °C are amorphous, but annealing these films at 550 °C in air lead to a crystalline structure. Fig. IV-5 displays the XRD patterns of $SnO_2$ and $SnO_2$ doped with 4 at. % Cu compared with Pt-coated alumina substrate pattern.

In both cases the tetragonal rutile-type $SnO_2$ phase is observed and the peak positions of the films are found to be in good agreement with JCPD 77-0450. It can be noted that no shift in the $SnO_2$ peak positions or any Cu phase (i.e., Cu oxides or ternary compounds with Cu) is observed due to the doping procedure. This observation leads to the conclusion that doping of $SnO_2$ with CuO has occurred.

There are two possible doping mechanisms of $SnO_2$ with CuO: A. substitutional and B. interstitial.

**A.** In the case of substitutional doping some $Sn^{4+}$ ions are replaced with $Cu^{2+}$(Eq.IV-1) based on the comparable radii of $Sn^{4+}$ and $Cu^{2+}$ (0.69 Å and 0.73 Å, respectively). The oxygen-ion vacancies ($V_o^{\cdot\cdot}$) created by substitutional doping of $Sn^{4+}$ with $Cu^{2+}$ are charge compensated by electron holes ($h^\cdot$), if the sample is annealed in air. The electron holes compensate the $Cu_{Sn}^{''}$ point defect charge and are required for the site balance (Eq.IV-2, Kröger-Vink notations).

**B.** In the second case $Cu^{2+}$ ions can occupy the interstitial sites of the $SnO_2$ lattice (Eq.IV-3), inducing an increase of the concentration of tin ion vacancies ($V_{Sn}^{''''}$).

**A.** Substitutional:

$$CuO \xrightarrow{\quad SnO_2 \quad} Cu_{Sn}^{''} + O_o^x + V_o^{\cdot\cdot} \qquad \text{Eq. IV-1}$$

$$CuO + \frac{1}{2}O_2 \rightarrow Cu_{Sn}^{''} + 2O_o^x + 2h^\cdot \qquad \text{Eq. IV-2}$$

**B.** Interstitial:

$$2CuO \xrightarrow{\quad SnO_2 \quad} 2Cu_i^{\cdot\cdot} + 2O_o^x + V_{Sn}^{''''} \qquad \text{Eq. IV-3}$$
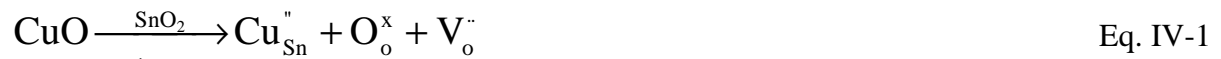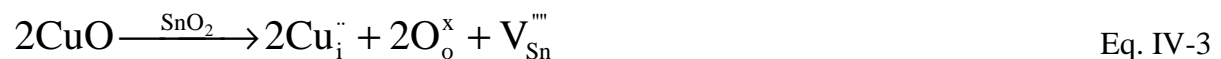
The crystallite size for doped and undoped samples was calculated using the Debye-Scherrer formula [94] for the (110), (101) and (211) peaks:

$$D = K\lambda/\beta\cos\theta \hspace{8cm} \text{Eq. IV-4}$$

Where D is the crystallite size (nm), $\lambda$ the radiation wavelength (0.15406 nm for Cu $K_\alpha$), $\beta$ the full-width at half maximum height FWHM of the X-ray line (radians), and $\theta$ is the diffraction peak angle. The average grain size D is found to be in the range 7-10 nm for $SnO_2$ and Cu-doped $SnO_2$. The XRD results confirm that the grains have a nanometer size and are in good agreement with the TEM results.

In conclusion, we have found that all the films crystallize in the tetragonal rutile phase. The copper dopant has a minor effect on the microstructure with no copper phase detected or particle size modification.
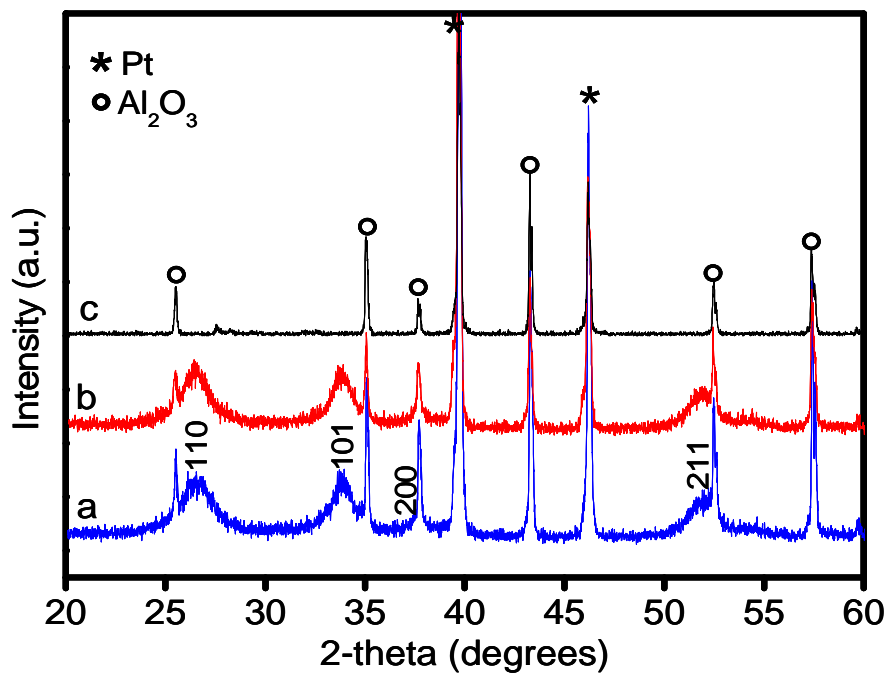


*Figure IV-5: XRD patterns of (a) SnO₂, (b) SnO₂ doped with 4 at. % Cu and (c) Pt-coated alumina substrate.*

### IV.2.1.3.    Transmission Electron Microscopy and Energy Dispersive X-ray Analysis

Due to its resolution the SEM technique did not allow to have a view of the particles at their atomic level, so, it was decided to employ the TEM technique for this purpose.

The TEM pictures of $SnO_2$ (Fig. IV-6a) revealed that the crystallite dimensions are in the range of nm. A very precise determination of the crystallite size cannot be made because they are not well separated being comprised in agglomerates. The grain size of undoped $SnO_2$ seems to be similar to that of Cu-doped $SnO_2$ (Fig. IV-6b).

It is concluded from the TEM evaluation that small amounts of copper have little influence on the film morphology and the particle size, thus supporting the results found in the previous SEM and XRD studies.
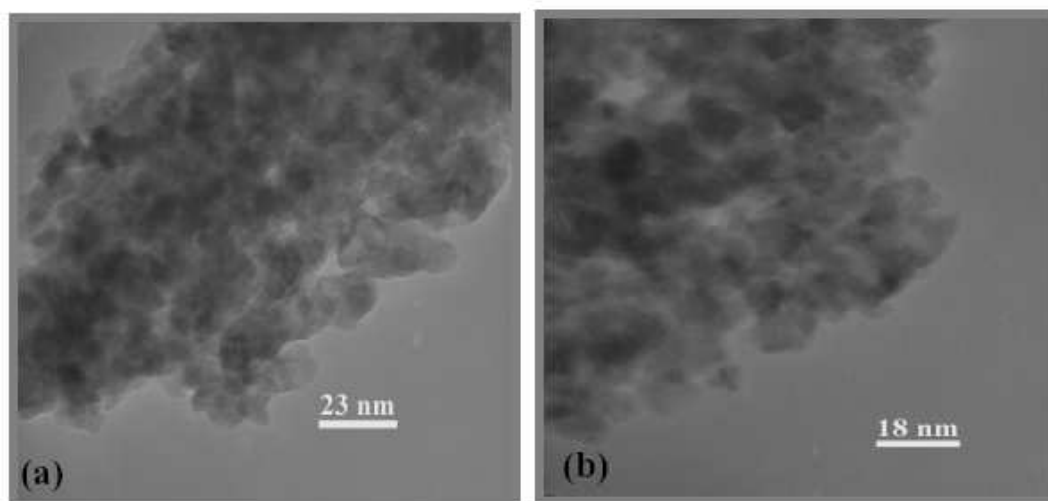


*Figure IV-6: TEM picture of a grinded: (a) SnO₂ film and (b) SnO₂ film doped with 4 at. %*
*Cu deposited at 400 °C (2ml/h for 1h) and annealed at 550 °C for 2h in air.*

To confirm the composition of the films and the presence of the dopant, the EDX analysis was employed for $SnO_2$ and for 4 at. % Cu-doped $SnO_2$ and Fig. IV-7 presents an EDX spectrum of $SnO_2$ doped with 4 at. % of Cu.  As it can be seen peaks associated with Sn, Cu, and O elements are present. The other noticed peaks, i.e., C and Au peaks are due to the grid on which the sample was laid.
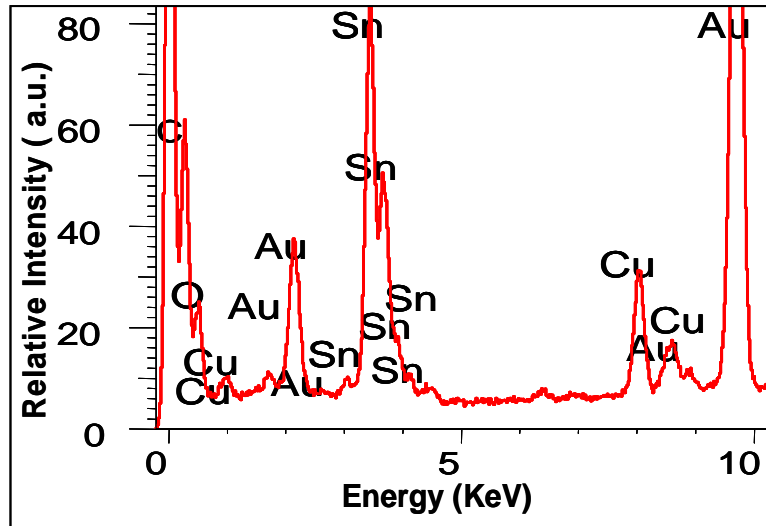
*Figure IV-7: EDX spectrum of SnO₂ doped with 4 at. % Cu deposited at 400 °C (2ml/h for 1h) and annealed at 550 °C for 2h in air.*

### IV.2.1.4.   Raman Spectroscopy

The Raman spectra of $SnO_2$ and Cu-doped $SnO_2$ (1 and 4 at. % Cu) films are presented in Fig. IV-8. The tetragonal rutile $SnO_2$ unit cell contains two tin ions and four oxygen ions and belongs to the space group $D_{4h}^{14} (P_{42/mnm})$. It displays four Raman active modes in the bulk of $SnO_2$: $A_{1g}$, $E_g$, $B_{1g}$, and $B_{2g}$ modes. Three Raman peaks for $SnO_2$ (Fig. IV-8a) are detected at 474, 632, and 773 $cm^{-1}$, corresponding to the $E_g$, $A_{1g}$, and $B_{2g}$ vibration modes of the tetragonal rutile phase. These results are in good accordance with the literature values [120].

The $A_{1g}$ (632 $cm^{-1}$) and $B_{2g}$ (773 $cm^{-1}$) modes are related to the expansion and contraction vibration modes of Sn-O bonds, while $E_g$ (474 $cm^{-1}$) mode is related to the vibration mode of oxygen ions. The $B_{1g}$ mode has an intensity so weak that it is not commonly detected [121], which is also proved by our spectra. Another Raman peak at 313 $cm^{-1}$ is also remarked in addition of the fundamental Raman peaks of rutile $SnO_2$. This Raman peak corresponds to the infrared (IR) active $E_u^{(3)}$TO mode corresponding to the transverse optical phonons. Abello et al. [121] explained that this IR active mode is induced when the particle size effect takes place. Similar results were reported recently by Sun et al. [122] for rutile $SnO_2$ nanobelts and by Liu et al. [123] for rutile $SnO_2$ nanorods.

So, considering the obtained results it can be concluded that all the peaks present in the Raman spectrum correspond to the tetragonal rutile phase of $SnO_2$. This result is in accordance with our previous XRD results.

Comparing the Raman spectra of the undoped $SnO_2$ and $SnO_2$ doped with different amounts of copper oxide, it is observed that for $SnO_2$ doped with 1 at. % Cu (Fig.IV-8 b) no significant shift of the peak position takes place. In addition, an important shift of the $SnO_2$ $A_{1g}$ band from 632 $cm^{-1}$ to 628 $cm^{-1}$ for $SnO_2$ doped with 4 at. % Cu (Fig. IV-8 c) is observed. This can be ascribed to the contribution of CuO modes to $SnO_2$ modes taking into account that the CuO $B_g$ mode is between 626-636 $cm^{-1}$ [124,125]. A decrease in the intensity of the peaks accompanied by an increase of their width, along with the increase of the copper content can be remarked. This can be due to the slightly decreased particle sizes, showed also by the SEM studies.
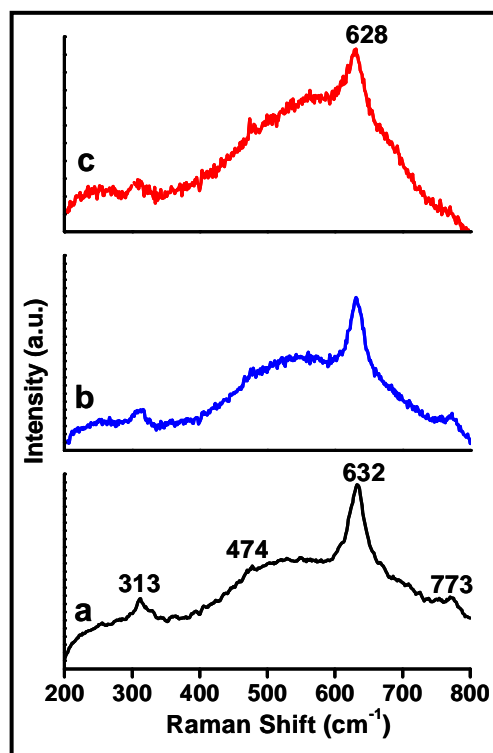


*Figure IV-8: Room-temperature Raman spectra of (a) $SnO_2$ (b) $SnO_2$ doped with 1 at. % Cu and (c) 4 at. % Cu films deposited at 400 °C (2ml/h for 1h) and annealed at 550 °C for 2h in air.*

## IV.2.2. Gas Sensing Properties

As presented in the introduction the response of a sensor is enhanced by a proper choice of dopants or additives. The resistance of $SnO_2$ films increases a few orders of magnitude when doped with CuO. The increase in the resistance due to the Cu dopant was observed also by several authors [107,117,126] and can be explained by the formation of oxygen ion vacancies as described by Eq. IV-5.

$$CuO \rightarrow Cu_{Sn}^{''} + O_o^x + V_o^{..}$$                                    Eq. IV-5

Where, in the Kröger-Vink notation: $Cu_{Sn}^{''}$ - is a copper ion sitting on a tin lattice site, with two negative charges; $O_o^x$ - is an oxygen ion sitting on an oxygen lattice site, with neutral charge while $V_o^{..}$ - is an oxygen ion vacancy, with double positive charge.

Tamaki et al. [107] investigated the addition of various metal ions to $SnO_2$ and they observed that the sensitivity to $H_2S$ increases when decreasing the cation electronegativity (increasing basicity) of the additive (Fig. 2). In particular the doping with $Cu^{2+}$ enhances greatly the sensitivity (S = 3.5 X $10^4$ for 50 ppm $H_2S$ at 200°C) to this gas.
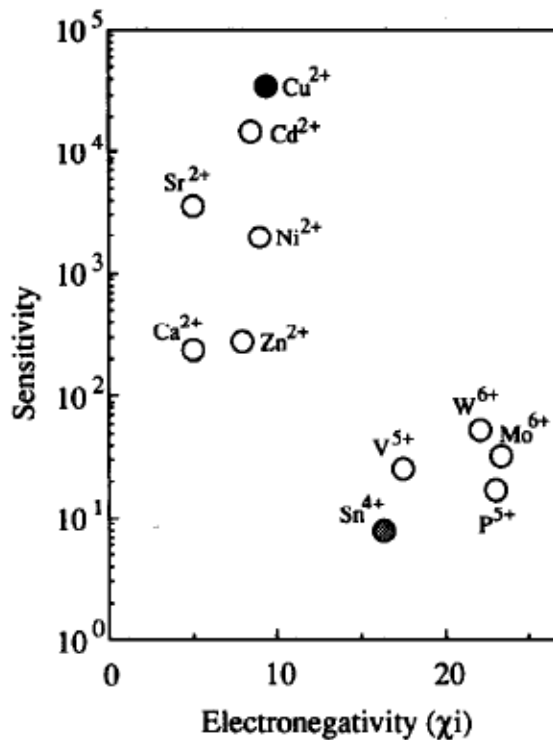


*Figure IV-9: The sensitivity of metal-oxide-added SnO₂ sensor as a function of the electronegativities of the added cations [107].*

In the next paragraph we will discuss the sensor performance in the detection of $H_2S$ as a function of the operating temperature.

In this study thin films of $SnO_2$, deposited by ESD method, are doped with copper (1, 2, and 4 at. %) in order to improve the sensitivity, especially to $H_2S$ but also to $SO_2$ and $NO_2$.

### IV.2.2.1. Influence of the operating temperature on the $H_2S$ sensor response

To determine the temperature corresponding to the maximum $H_2S$ sensitivity, the films were exposed to 10 ppm $H_2S$ in the temperature range of 100 to 300 °C. For each day of measurements the temperature was set to a constant value between 100 and 300 °C by steps of 50 °C. Before starting the measurements, the films were regenerated in synthetic air for 60 min and then exposed for 30 min to $H_2S$. This cycle was repeated 4 or 5 times during a day and then the next temperature was set for the following day. The same procedure was used every day until the whole range of temperature was explored.

The dependence of the $H_2S$ sensitivity ($R_{air}/R_{H_2S}$) to the temperature is shown in Fig. IV-10.
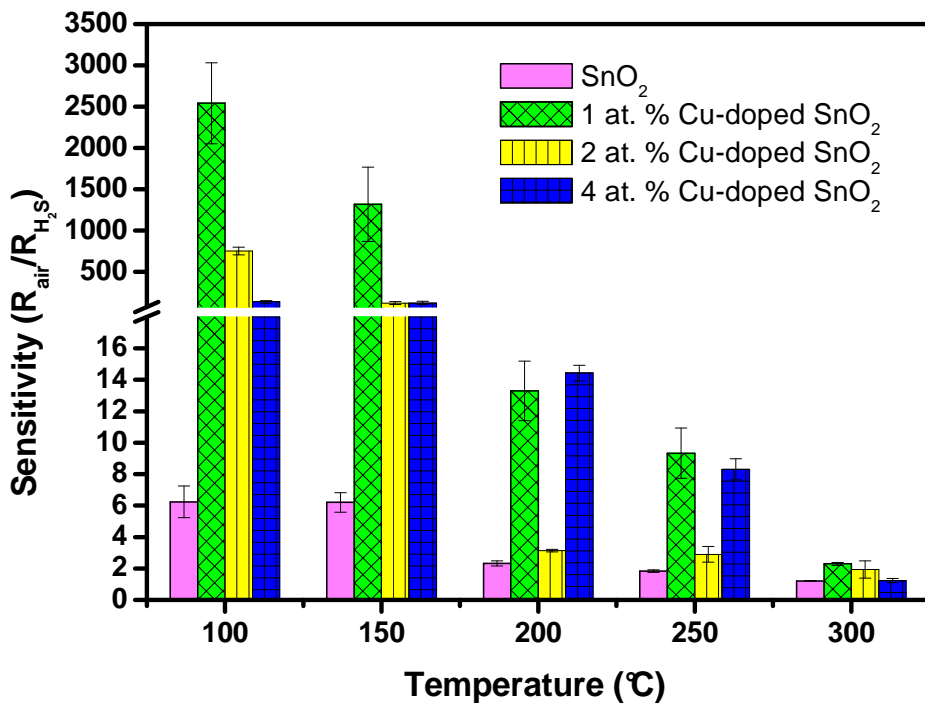


*Figure IV-10: SnO$_2$ and Cu-doped SnO$_2$ sensitivities to 10 ppm H$_2$S as a function of the operating temperature.*

As it can be observed, the $H_2S$ sensitivity of $SnO_2$ decreases when increasing the operating temperature, presenting a maximum of about 6 for 100 °C. In the present study, the Cu-doped $SnO_2$ layers show the same behaviour but with a much higher sensitivity. Our results are in accordance with the literature which shows that the maximum sensitivity for Cu-doped $SnO_2$ films is found between 50 and 200 °C depending on the preparation method of the sensor [36,107,118,127].

To discuss the influence of the copper doping on the sensitivity and also for a better view, the graph from Fig. IV-10 has been represented also as sensitivity as a function of the copper concentration for different operating temperatures (Fig. IV-11).
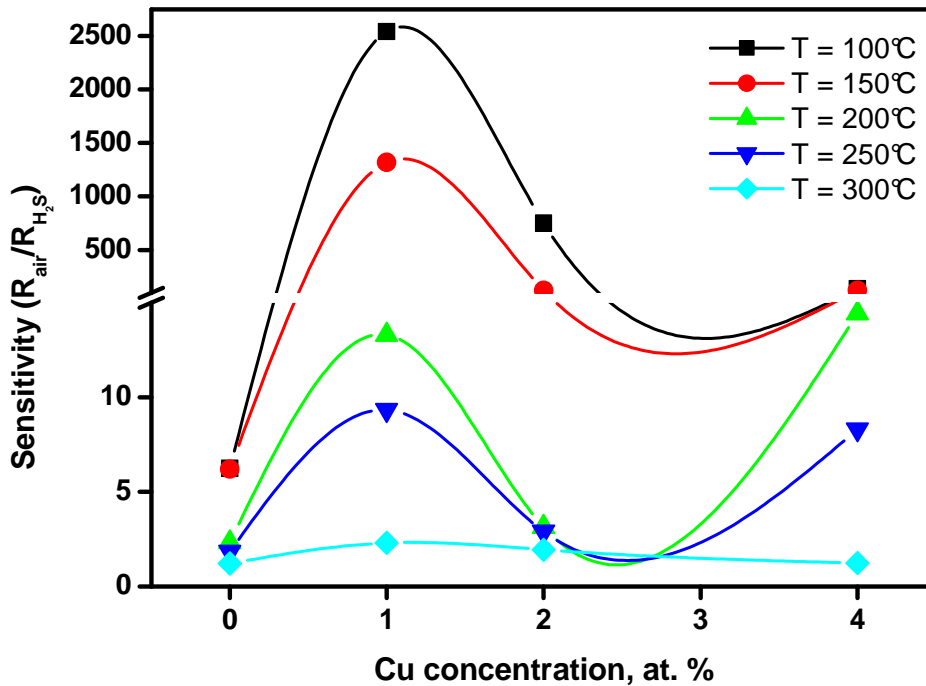


*Figure IV-11: Sensitivity of $SnO_2$ to 10 ppm $H_2S$ as a function of the copper concentration for different operating temperatures.*

In this graph three different behaviour regions can be distinguished: (a) between 0 and 1 at. % Cu the sensitivity increases for the entire temperature range, (b) between 1 and 2 at. % Cu the sensitivity decreases for all the temperature ranges and (c) between 2 and 4 at. % Cu the sensitivity varies (decreases, increases) depending on the operating temperature.

### (A) Between 0 and 1 at. % Cu

For compositions between 0 and 1 at. % Cu the sensitivity increases in the entire temperature range.For all the Cu-doped $SnO_2$ compositions the sensitivity to $H_2S$ is higher than for undoped $SnO_2$ and the response value depends mainly on the Cu percentage and on the operating temperature.

To explain the modification of the film resistance during $H_2S$ exposure several mechanisms can be presented:

First, the adsorption mechanism can be proposed, as presented in detail in Chapter V. Briefly, the adsorbed oxygen on the surface of undoped or doped $SnO_2$ films reacts with $H_2S$, realising electrons into the conduction band and the resistance is decreased.

Moreover, the copper has a tendency to reside at the layer surface and to cover the $SnO_2$ grains. For this reason the copper can play an important catalytic role in the reaction with $H_2S$.

In this way, Morrison [33] proposed two mechanisms of catalyst control on gas sensors: the spillover mechanism and the Fermi level energy control mechanism. In the spillover mechanism the surface catalyst dissociates the gas molecule, and reactive atoms formed are spilled over on the semiconductor surface and influence the conductivity.

Recently Chowdhuri et al. [128] have proposed this mechanism to explain the CuO-$SnO_2$ response to $H_2S$. They used bilayer structure of $SnO_2$ and ultra-thin CuO dotted islands, and they stated that CuO initiated the hydrogen spillover. The hydrogen is weakly chemisorbed on the surface and interacts with the oxygen removed from the uncovered $SnO_2$.

The Fermi level mechanism assumes that the $H_2S$ converts the Cu or CuO in CuS (Eq. IV-6) which has a metallic conductivity (high conductivity) and the response is greatly improved. The formation of CuS has been confirmed by X-ray diffraction [109], X-ray photoelectron spectroscopy [108], and Raman spectroscopy [126] measurements.

$$CuO + H_2S \rightarrow CuS + H_2O \hspace{4cm} Eq.\ IV\text{-}6$$

In addition, the fact that the response of Cu-doped $SnO_2$ decreases sharply when the operating temperature is higher than 150 °C can be due to the CuS crystal structure instability, which begins to transform at 103 °C into $Cu_2S$, an ionic conductor with high resistance [129].

On subsequent exposure to $O_2$ the CuS is transformed back to CuO according to the Eq. IV.-7.

$$CuS + 3/2\ O_2 \rightarrow CuO + SO_2 \qquad\qquad \text{Eq. IV-6}$$

The amount of Cu affects the dispersion of Cu in the way that the higher the Cu content is, the lower the dispersion is. So, in consequence the catalytic effect is different depending on the amount of dopant, which influences further the response.

### (B) Between 1 and 2 at. % Cu

For compositions between 1 and 2 at. % the sensitivity decreases in the entire temperature range.

### (C) Between 2 and 4 at. % Cu

The behaviour in this concentration range is not the same for the entire temperature range. For 100 °C the sensitivity decreases, for 150 °C the sensitivity is constant and for 200 and 250 °C the sensitivity increases to reach the 1 at. % Cu-doped $SnO_2$ level. For 300 °C the sensitivity is constant. Other authors have reported similar results but no explanation has been presented [130,131]. We believe that for high concentration of Cu (4 at. %) a CuO second phase is formed as showed by Raman studies. This phase could not be seen in the XRD spectra due to the detection limit of the instrument.

All these mechanisms can play an important role and the one which is predominant depends mainly on the amount of Cu or (and) CuO in the films and of the operating temperature.

Considering the obtained results in this work the optimum operating temperature has been selected to be 100 °C and this temperature will be used to further study the sensor response as function of the gas concentration and also to evaluate the cross-sensitivity to the other gases, i.e., $SO_2$ and $NO_2$.

### IV.2.2.2. Influence of the gas concentration on the H₂S sensor response

Several papers in the literature [107-109,128,130] present the H₂S response as a function of the gas concentration for a range between 5 and 1250 ppm.

In our work we prefer to evaluate the response of the films to smaller concentrations of H₂S (from 1 to 10 ppm, with steps of 3 ppm) considering that the limit allowed in the atmosphere is 10 ppm and that concentrations higher than 250 ppm are lethal [10].

During a day the film was exposed a few times to 1 ppm H₂S followed by regeneration with synthetic air and this operation was repeated daily until the entire concentration range was studied. The relation between the sensor response and the gas concentration was evaluated at 100 °C by varying the concentration between 1 to 10 ppm H₂S (Fig. IV-12). As it is observed for $SnO_2$ and also for all the compositions (1, 2, and 4 at. %) of Cu-doped $SnO_2$, the sensitivity increases with the increase of the concentration from 1 to 10 ppm H₂S.

From all the studied samples the 1 at. % Cu-doped $SnO_2$ presents the maximum sensitivity (2500 for 10 ppm H₂S) followed by 2 at. % Cu-doped $SnO_2$ (752 for 10 ppm H₂S), by 4 at. % doped-$SnO_2$ (138 for 10 ppm H₂S) and $SnO_2$ (6.25 for 10 ppm H₂S). The same order in the response is also observed for the other studied concentrations. It is obvious that all Cu-doped tin oxide films are more sensitive to H₂S compared with the undoped tin oxide films.
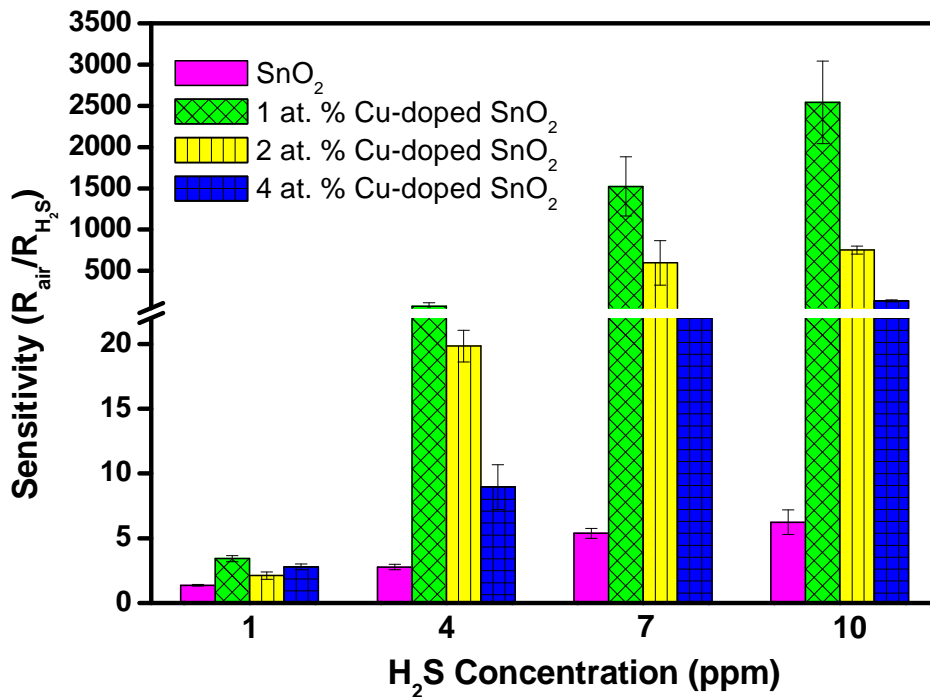


***Figure IV-12: SnO₂ and Cu-doped SnO₂ sensitivities as a function of the H₂S concentration at 100 °C operating temperature.***

Taking into account the results it can be concluded that the present films exhibit a higher sensitivity, i.e., 2500, for low concentrations (1-10 ppm $H_2S$) and lower operating temperature (100°C) compared with films made with different deposition techniques [108].

### IV.2.2.3. $H_2S$ gas sensor cross-sensitivity to $SO_2$ and $NO_2$

Taking into account that in the atmosphere many pollutant gases are present at the same time, the possibility of detecting a specific desired gas is of great interest. Therefore, the sensitivity to other gases, i.e., $SO_2$ and $NO_2$ has been also studied to verify the $H_2S$ cross-sensitivity of the present sensor layers. As $H_2S$, $SO_2$ is a reducing gas, resulting in a decrease of the film resistance during gas exposure, while $NO_2$ is an oxidising gas leading to an opposite behaviour, i.e., increase of the film resistance.

### A. *Sensor response to $SO_2$*

The undoped tin oxide films are almost insensitive to 20 ppm $SO_2$ (Fig. IV-13) and doping with different amounts of copper did not improve the sensitivity.

### B. *Sensor response to $NO_2$*

The $SnO_2$ films present a negligible response to 1 ppm $NO_2$ (Fig. IV-13), but for all Cu-doped samples the sensitivity is improved, and the maximum is found for 1 at. % Cu, (9.7), followed by 4 at. % Cu (3) and 2 at. % Cu (1.2) in comparison with pure $SnO_2$ (1.02). The influence of the copper amount to the $NO_2$ sensitivity is similar with the behaviour presented under $H_2S$, i.e., three regions of interest (0 to 1 at. % Cu the sensitivity increases, 1 to 2 at. % Cu the sensitivity decreases and between 2 to 4 at. % Cu the sensitivity increases or is constant).

As we can know, the improvement of the $SnO_2$ response to $NO_2$ by doping with Cu has not yet been presented in the literature, but Zhang et al. [132] showed that the enhancement of the Cu-doped $SnO_2$ response to another oxidizing gas, i.e., nitrogen monoxide (NO), is due to the cuprous ions $Cu^+$, which coexists with cupric ions $Cu^{2+}$ (Eq. IV-8) during the gas exposure. Considering that NO in the presence of oxygen from air oxidizes to nitrogen oxide ($NO_2$) according to Eq. IV-9, it is assumed that the detection mechanism of $NO_2$ is similar with the NO detection mechanism presented in [132].

$2CuO \rightarrow Cu_2O + 1/2O_2$                                                                          Eq. IV-8

$2NO + O_2 \rightarrow 2NO_2$                                                                                  Eq. IV-9
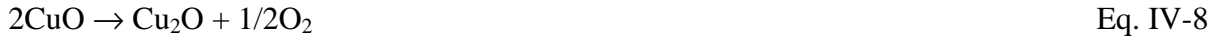
As it can be observed in Fig. IV-13, the sensitivity of all the films at 100 °C to 10 ppm $H_2S$ is higher than the sensitivity to 20 ppm $SO_2$ and to 1 ppm $NO_2$, suggesting no-cross sensitivity of $H_2S$ to these two gases. Taking into account this observation, it is evident that the films can be selective in the case that $H_2S$ has to be detected from a mixture composed of $H_2S$, $SO_2$, and $NO_2$.
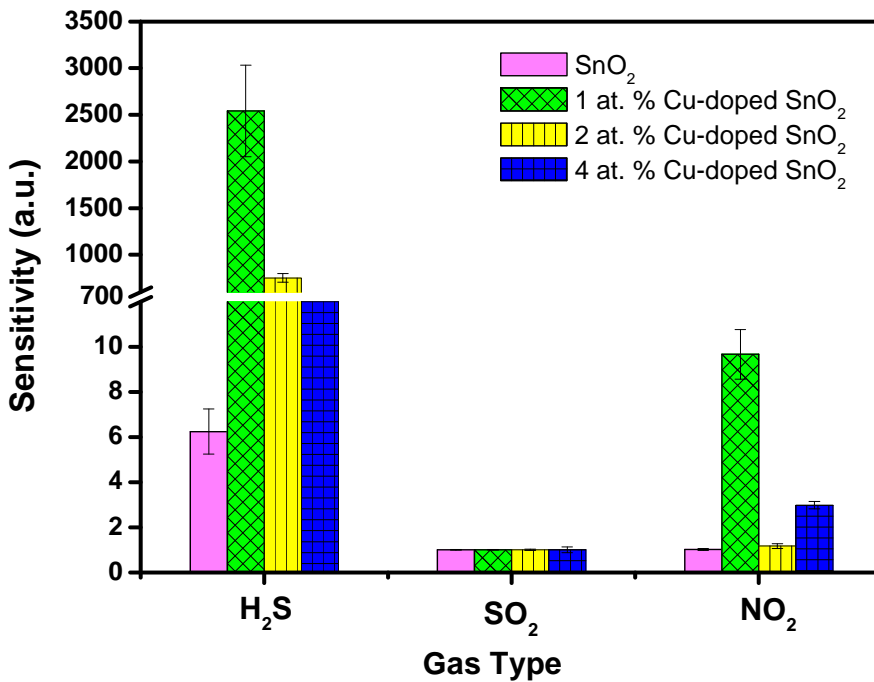


*Figure IV-13: SnO₂ and Cu-doped SnO₂ sensitivities to 10 ppm H₂S, 20 ppm SO₂ and 1 ppm NO₂ at 100 °C operating temperature.*

All the gas-sensing measurements have been repeated at least three times in order to ensure reproducibility. Furthermore, the measurement average error estimation has a value of 7 %.

## IV.3.  CONCLUSIONS

In this chapter it was presented the deposition of $SnO_2$ and Cu-doped $SnO_2$ films, their morphological characterization, and their gas sensing performance under $H_2S$, $SO_2$ and $NO_2$.

Varying the deposition parameters, i.e., temperature, time, and flow rate, $SnO_2$ thin films with different morphologies, thicknesses, and particle sizes were obtained, as revealed by SEM studies. The morphological analysis allowed the selection of the deposition parameters, permitting to obtain porous, adherent, homogeneous thin films. The microstructure evaluated by XRD and Raman Spectroscopy showed the tetragonal rutile structure, required for gas sensing layers. The TEM and XRD studies revealed the nanometer size of the grains.

The Cu-doping proved to have a minor effect on the morphology and the microstructure of the $SnO_2$ films, as shown by SEM, TEM, and XRD analysis. On the contrary, doping the $SnO_2$ films with small amounts of Cu improved greatly the sensitivity to low concentrations of $H_2S$ and also the sensitivity to $NO_2$. So, this result proves that the selection of the copper dopant was suitable for the present application.

The studies of the film sensitivity to $H_2S$ as a function of the temperature revealed that the temperature corresponding to the maximum $H_2S$ response is 100 °C. For all the studied compositions, the films doped with 1 at. % Cu proved to be the most sensitive to $H_2S$ and the sensitivity decreases when higher amounts of copper are used. No cross-sensitivity of $H_2S$ to other gases ($SO_2$, $NO_2$) has been observed at the optimum selected operating temperature, the sensor response to these two last gases being much smaller compared with the $H_2S$ response.

In conclusion, we showed that the ESD technique is an useful technique, which allowed the deposition of $SnO_2$ and Cu-doped $SnO_2$ films with controlled morphology, which allows us to propose the fabrication of a selective sensor, able to detect $H_2S$ from a mixture of $H_2S$, $SO_2$, and $NO_2$.

Another important feature of the present films is that the gas detection temperature is low, i.e., 100 °C, compared with other metal oxides, hence, in this way the energy consumption can be reduced.

# CHAPTER V:

## GAS SENSORS BASED ON ZINC OXIDE

# V. GAS SENSORS BASED ON ZINC OXIDE

## V.1. INTRODUCTION

Because of its semiconducting, optical, piezoelectrical properties, ZnO has been used as gas sensor [133] and in different other applications such as solar cell electrode [134,135], optical waveguide device [136], light emitting device [137], catalyst [138] etc.

Until now, different physical and chemical techniques [139,139-141] more or less sophisticated and expensive, have been used to prepare ZnO [140-143]. From our knowledge, there is no paper in the literature describing the gas sensing properties of ZnO deposited by the Electrostatic Spray Deposition technique. The ESD method was selected for the deposition of ZnO films taking into account the advantages presented in Chapter III. For example, the control of the surface morphology is of particular interest for gas sensor [139] applications, where a porous morphology is desired in order to increase the gas adsorption and implicitly the sensor response to a specified gas [6].

The aim of this chapter is to present the optimisation of the deposition process of porous ZnO films using the ESD method and tuning the deposition parameters (flow rate and time). The film structural and morphological characterization has been performed with different techniques. The ZnO film application as gas sensor for the detection of $NO_2$, $H_2S$, and $SO_2$ is also presented [144].

ZnO is one of the earliest materials used as chemoresistive sensor [25] to detect different pollutant gases including CO [145], $C_2H_5OH$ [146], $H_2$ [147], $O_2$ [41], and $O_3$ [148]. There are only few papers in the literature [149,150], which describe the gas sensing properties of ZnO to detect $NO_2$ and $H_2S$ [151]. So, it is interesting to present the response to these two gases using films of ZnO prepared by a technique not previously employed for this kind of application.

# V.2. RESULTS AND DISCUSSIONS

## V.2.1. Morphology and Structure Characterizations

### V.2.1.1. Scanning Electron Microscopy

The ZnO films were deposited at 350 °C. The selection of the temperature has been made according to the literature which presented the successfully deposition of porous ZnO films at 350 °C [86].

*A. Flow rate effect*

Firstly, the influence of the flow rate on the film morphology is presented. The morphology of the films was studied by SEM and the micrographs of the ZnO films deposited at 350 ºC for 1h with 1ml/h and 2ml/h are depicted in Fig. V-1a respectively Fig. V-1b. The films exhibit a porous morphology comprising in spherical particles. Furthermore, when increasing the flow rate from 1ml/h to 2 ml/h, an increase in the particle size from 1-2 μm to 1-5 μm is noticed. This result is in good accordance with the formula deduced by Ganán-Calvo (Eq.III-1) [139-141]. The pictures show also a substrate not fully covered, especially when the flow rate is small. This can be due to the complete evaporation of the solvent. For this reason the films deposited with high flow rate, i.e., 2ml/h were selected for further studies.

*B. Deposition time effect*

Other observation concerns the increase of the deposition time from 1h (Fig. V-1b) to 2h (Fig. V-1c) which shows that the film becomes more porous. Taking into account the porous morphology and the good coverage of the substrate, the film shown in Fig. V-1c has been selected for further microstructure and gas sensing characterization. The as-presented film shows a porous morphology, which consists of large spherical grains (which are actually agglomerates of tinny particles) with sizes ranging from 1 to 7 μm. To ensure reproducibility, 5 other films with the same operating conditions have been prepared.

The thickness of the layer was determinated from the film cross-sectional SEM picture (Fig. V-1d) and was estimated around 7 μm with good adherence, coverage of the substrate, and with no observed cracks.
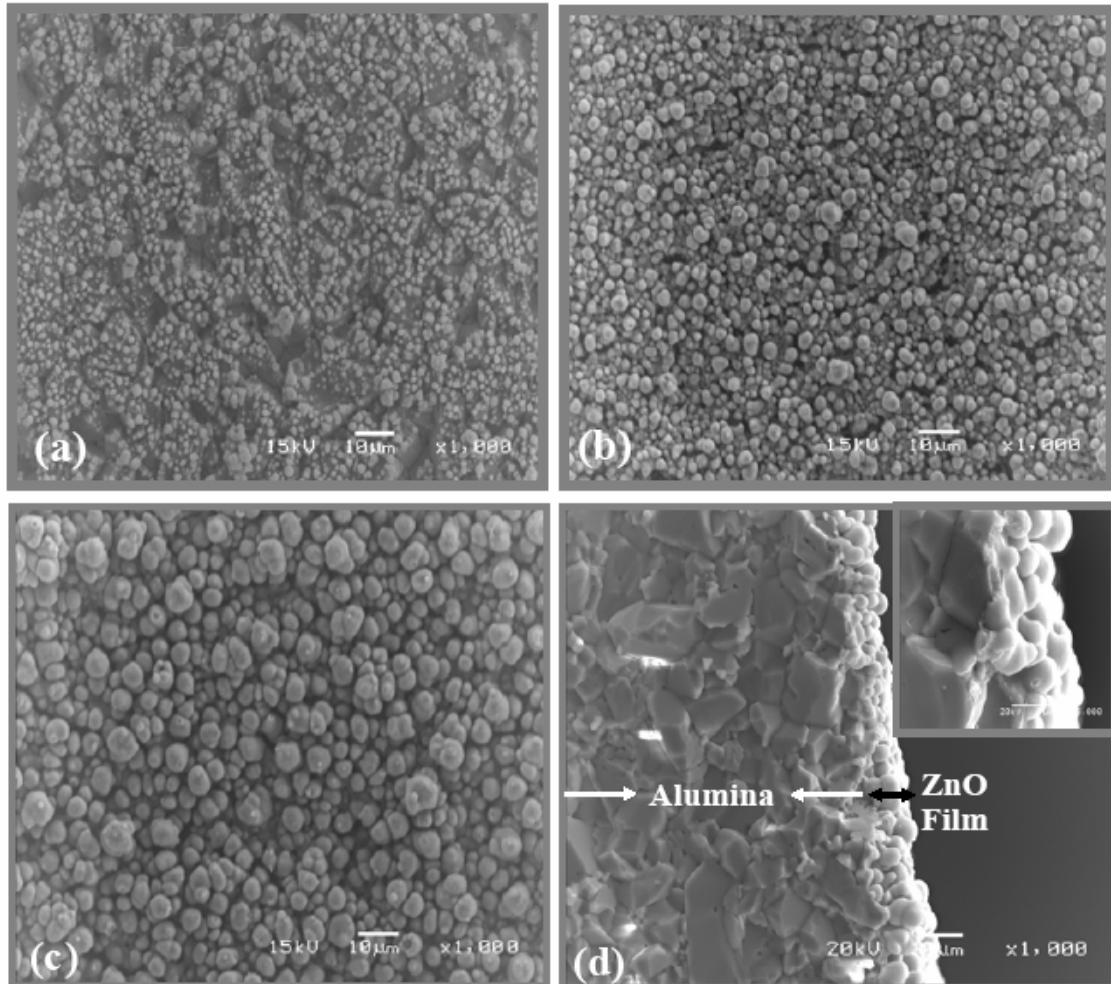


*Figure V-1: SEM picture of a ZnO film deposited on Pt-coated alumina at 350 ºC and (a) 1ml/h for 1h; (b) 2ml/h for 1h; (c) 2ml/h for 2h top view and (d) 2ml/h for 2h cross-sectional view.*

In order to examine the composition of the films, the EDX analysis was performed on a ZnO film deposited at 350 ºC (2ml/h for 2h) and annealed for 2h at 600 ºC. Fig. V-2 shows the EDX spectrum, in which characteristic peaks of Zn and O belonging to the ZnO structure can be observed. The other noticed peaks, i.e., C and Cu peaks are due to the grid on which the sample was laid.
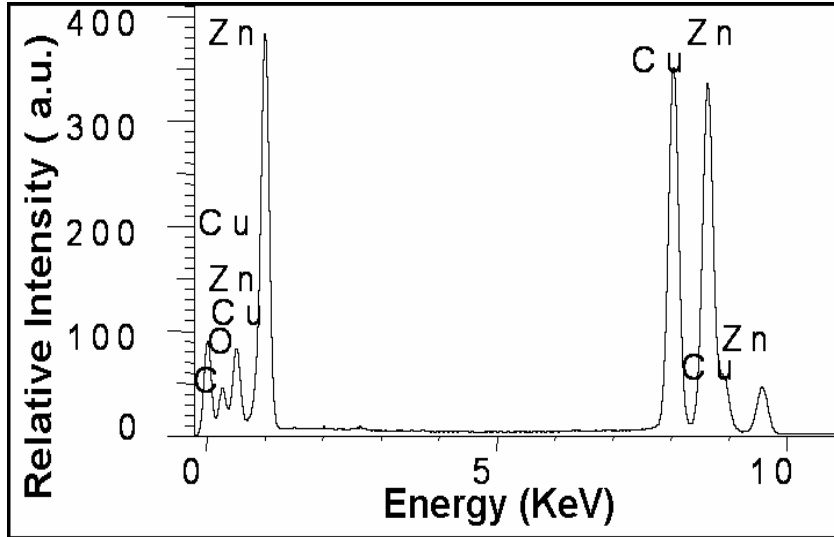
*Figure V-2: EDX spectra of a grinded ZnO film deposited on Pt-coated alumina at 350 ºC (2 ml/h for 2h) and annealed at 600 ºC for 2h.*

### V.2.1.2. X-ray Diffraction

The phase composition of the as prepared films and the effect of the thermal treatment on the film crystallinity was examined by the XRD technique.

The XRD pattern (within the 2θ range of 30-70º) of a ZnO film deposited on Pt-coated alumina at 350 ºC (2ml/h for 2h) and annealed for 2h at 600 ºC are shown in Fig. V-3. All the diffraction peaks (Fig. V-3b) were indexed with the hexagonal wurtzite structure (space group P6$_3$mc). Some of the peaks, corresponding to the diffraction planes (200), (112) and (201) overlapped with those of the Pt-alumina substrate (Fig. V-3c). No impurity peaks have been detected in the present XRD pattern, suggesting good quality of the ZnO films.

The calculated distance values between the atom planes are in good agreement with JCPDS 76-0704 (Table V-1). If the d-values before and after annealing are compared, it is noticed that in the second case the d-values decrease suggesting a better crystallinity and an increase in the particle sizes. Comparing the diffraction peaks of the non-annealed film (Fig. V-3a) with those of the film annealed at 600 ºC in air (Fig. V-3b) it is observed that the intensity of the peaks increases while their width decreases after the thermal treatment, which means that the crystallinity has been improved and in the same time the grain size is increased.

The crystallite sizes were calculated with the Debye-Scherrer (Eq.IV-4) formula using the full-width at half maximum of the peaks corresponding to the planes (110), (002), and (101). The particle sizes were found to vary between 12 and 18 nm for the as-deposited films and between 17 and 21 nm for the annealed films. This result confirms the previous observation of particle growth.

From the present XRD study it is concluded that the ZnO films are crystallized in the hexagonal wurtzite phase and that they present grains in the nanometer range, properties demanded for gas sensor applications.
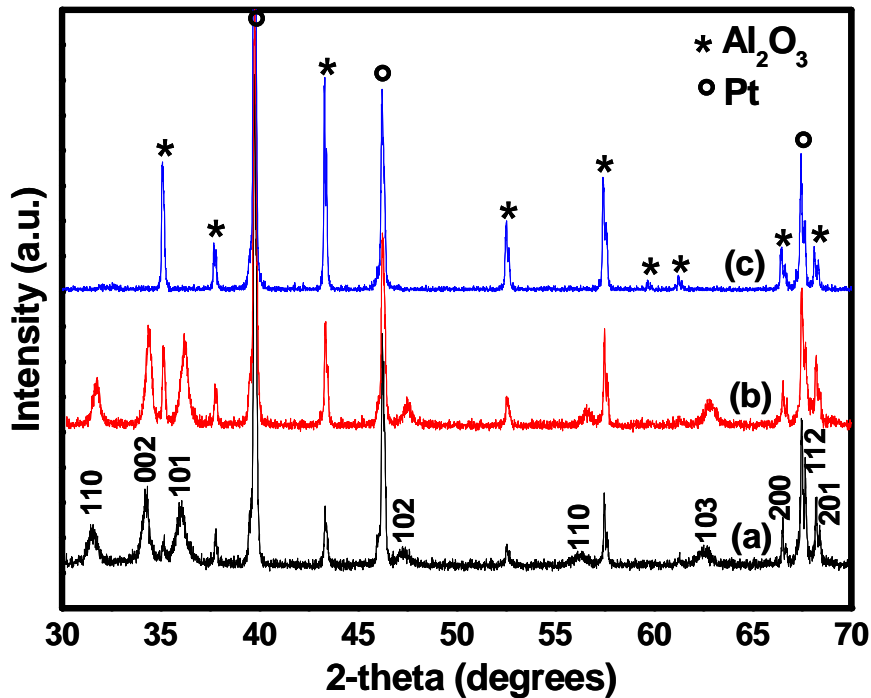


***Figure V-3: XRD pattern of a ZnO film deposited on Pt-coated alumina at 350 ºC (2 ml/h for 2h) and annealed at 600 ºC for 2h.***

| ESD deposited ZnO | | | JCPDS 76-0704 |
|---|---|---|---|
| Non-annealed film | Annealed film | | |
| d-Value(Å) | d-Value(Å) | (hkl) | d-Value(Å) |
| 2.8319 | 2.8164 | 100 | 2.8171 |
| 2.6157 | 2.6047 | 002 | 2.6064 |
| 2.4901 | 2.4787 | 101 | 2.4784 |
| 1.9204 | 1.9123 | 102 | 1.9132 |
| 1.6339 | 1.6272 | 110 | 1.6265 |
| 1.4838 | 1.4772 | 103 | 1.4790 |

***Table V-1: The comparison between d-values of the as-deposited ZnO film at 350 ºC and annealed at 600 ºC with the d values taken from JCPDS 76-0704.***

### V.2.1.3. Raman Spectroscopy

Fig. V-4 presents the Raman spectrum of a ZnO film deposited at 350 ºC (2ml/h for 2h) and annealed in air at 600 ºC.

The hexagonal ZnO belongs to the space group $C_{6v}^4$ and the group theory predicts the existence of the following optical modes: $\Gamma = 1A_1(z) + 2B_1 + 1E_1(x,y) + 2E_2$. The $A_1$ and $E_1$ modes are polar and split into transverse (TO) and longitudinal optical (LO) phonons due to the macroscopic electric fields associated with the LO phonons. Both $A_1$ and $E_1$ modes are Raman and IR active. The two non-polar IR inactive $E_2$ modes [$E_2^{(1)}$, $E_2^{(2)}$] are Raman active. The $B_1$ modes are IR and Raman inactive [152,153].

In the present films, the second order Raman mode from 329 cm$^{-1}$ arises from the zone-boundary phonons $2E_2$ ($E_{2H}$-$E_{2L}$) of ZnO [154]. The 385 cm$^{-1}$ mode corresponds to $A_1$ symmetry with TO mode [154]. The dominant peak at 437 cm$^{-1}$ is assigned to the optical phonons high $E_2$ mode and corresponds to the band characteristic for hexagonal wurtzite ZnO [155,156]. The high Raman active $E_2$ mode indicates the high crystallinity of the films. The 578 cm$^{-1}$ mode is attributed to $A_1$(LO) which is due to structural point defects (oxygen vacancies, zinc interstitial, or free electronic charge carriers) [154]. In this case, we cannot exactly say which one of these defects are present in the ZnO films because no specific measurements have been done to characterize the ZnO defect structure.

Literature [157] shows that the $A_1$(LO) mode can be placed at different frequencies varying from 591 to 574 cm$^{-1}$ due to the anisotropic short-range forces in the uniaxial ZnO lattice, hence the present obtained result (574) cm$^{-1}$ is in good agreement with the literature data.

So, the above-presented results confirm the hexagonal wurtzite structure and the crystallinity of the ZnO films, which is in good agreement with the previous XRD results.
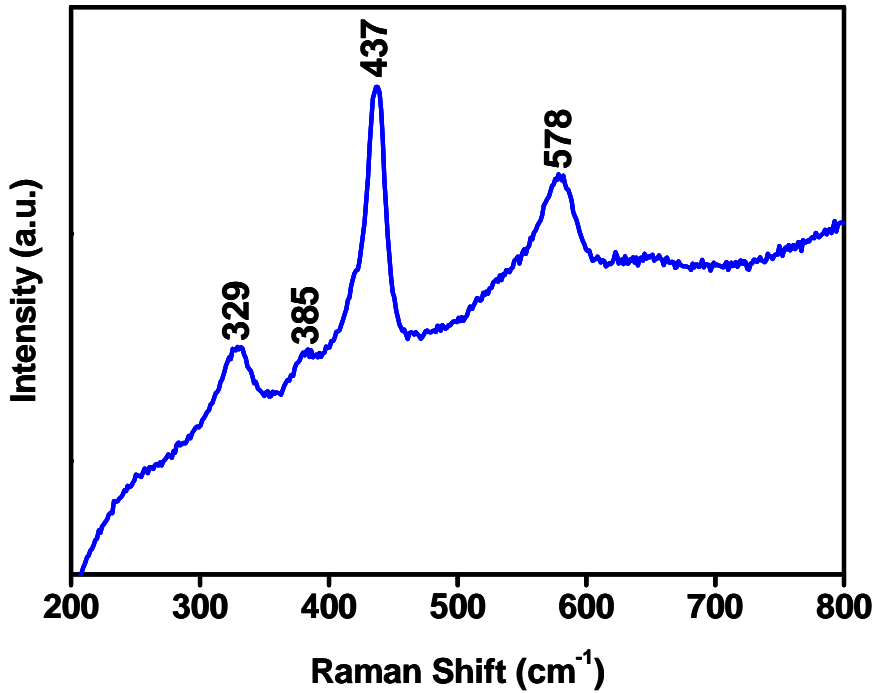
*Figure V-4: Room temperature Raman spectrum of a ZnO film deposited on Pt-coated alumina at 350 ºC (2 ml/h for 2h) and annealed at 600 ºC in air for 2h.*

## V.2.2. Gas sensing properties

### V.2.2.1. Influence of the operating temperature on the NO$_2$ sensor response

The sensitivity (S) of the ZnO films deposited at 350°C (2ml/h for 2h) was studied first as a function of the operating temperature (200-450 °C) for fixed NO$_2$ (1 ppm) or H$_2$S (12 ppm) concentrations as shown in Fig. V-5. The sensor response (S) was defined as the ratio of R$_g$/R$_a$ for NO$_2$ (oxidizing gas) and R$_a$/R$_g$ for H$_2$S (reducing gas), where R$_a$ represents the electrical resistance of the film in synthetic air and R$_g$ represents the resistance of the film during the gas exposure.

As it can be observed, the 1 ppm NO$_2$ response presents a maximum for 300 °C, when the temperature changes from 200 °C to 300 °C, the sensor sensitivity increases from 1.31 to 1.84, which is the maximum response. Increasing the temperature beyond 300 °C the sensitivity decreases, reaching a value of 1.28 at 450 °C.
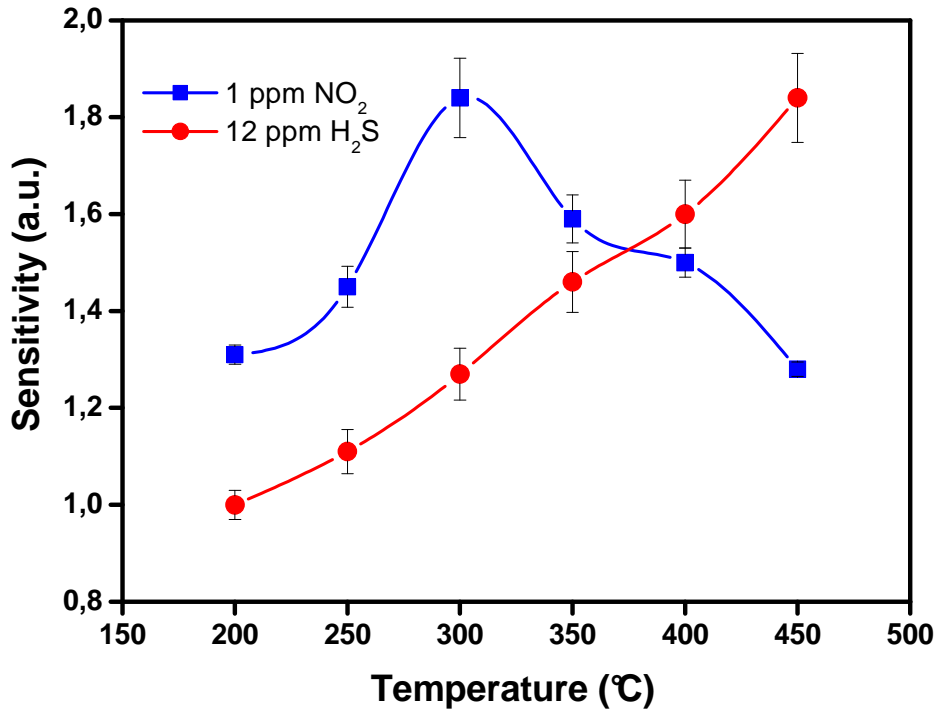
*Figure V-5: The sensitivity of ZnO sensor to 1 ppm NO₂ and 12 ppm H₂S at various operating temperatures.*

The gas detection mechanism can be explained by the surface reaction between adsorbed oxygen and the gas to be detected.

In a first step, the molecular oxygen is adsorbed on the ZnO surface (Eq. V-1) and it depletes electrons from the conduction band. Due to this phenomenon the oxygen is chemisorbed in the form of $O_2^-, O^-, O^{2-}$ depending on the operating temperature as shown in Eqs. V-1-4 [40-42] and also depending on the grain size and film porosity [158].

$$O_{2(gas)} \Leftrightarrow O_{2(ads)} \qquad\qquad\qquad\qquad\qquad\qquad\qquad \text{Eq. V-1}$$

$$O_{2(ads)} + e^- \Leftrightarrow O_{2(ads)}^- \qquad\qquad T < 100°C \qquad\qquad\qquad \text{Eq. V-2}$$

$$O_{2(ads)}^- + e^- \Leftrightarrow 2O_{(ads)}^- \qquad\qquad T = 100\text{-}300°C \qquad\qquad \text{Eq. V-3}$$

$$O_{(ads)}^- + e^- \Leftrightarrow O_{(ads)}^{2-} \qquad\qquad T > 300°C \qquad\qquad\qquad \text{Eq. V-4}$$

In a second step, when the film is exposed to $NO_2$, which is an oxidising gas, the molecules can directly be adsorbed onto the surface by extracting electrons from the conduction band (Eq. V-5), or they can interact with the chemisorbed oxygen on the surface (Eqs.V-6-7) [149,159,160].

$$NO_{2(gas)} + e^- \rightarrow NO_{2(ads)}^- \qquad \text{Eq. V-5}$$

$$NO_{2(gas)} + O_{2(ads)}^- + 2e^- \rightarrow NO_{2(ads)}^- + 2O_{(ads)}^- \qquad \text{Eq. V-6}$$

$$NO_{2(gas)} + O_{(ads)}^- \rightarrow NO_{(ads)}^+ + 2O_{(ads)}^- \qquad \text{Eq. V-7}$$

As shown by these equations, conduction electrons are consumed in the reactions, which explain the increase of the ZnO resistance during the $NO_2$ exposure. The maximum $NO_2$ sensitivity is shown at 300 °C by a clear peak. At this temperature the ionised oxygen ($O^-$) is the predominant specie (Eq. V-3) and in the reaction with $NO_2$, nitrosil ($NO^+$) species are formed according to the Eq. V-7, which seems advantageous to obtain a better response.

### V.2.2.2. Influence of the operating temperature on the $H_2S$ sensor response

Concerning the 12 ppm $H_2S$ response (Fig. V-5) the sensitivity increases with the increase of the temperature in the studied range, reaching a maximum value of 1.8 at 450 °C. On the contrary of the $NO_2$ behaviour, an increase of the ZnO film sensitivity ($R_a/R_g$) is observed upon $H_2S$ exposure, which can be justified by its reaction with chemisorbed oxygen (Eq.V-8), inducing the release of electrons into the conduction band [40].

$$H_2S_{(gas)} + O_{(ads)}^- \Leftrightarrow H_2SO_{(ads)} + e^- \qquad \text{Eq. V-8}$$

Dayan et al. [147] have explained that the intrinsic defects on the ZnO surface can also have an influence in the detection mechanism. The interstitial zinc atoms can be ionised and electrons are formed inducing a decrease in the resistance (Eq. V-9).

$$Zn_i^{..} + e^- \Leftrightarrow Zn_i^{.} \qquad \text{Eq. V-9}$$

Xu et al. [161] described a more complex mechanism of $H_2S$ detection in which water and sulphur dioxide are formed besides electron creation. (Eqs.V-10-12).

$$H_2S_{(gas)} \Leftrightarrow H_2S_{(ads)} + e^-$$ 　　　　　Eq. V-10

$$H_2S_{(gas)} + O_{2(ads)}^{x-} \Leftrightarrow H_2S_{(ads)} + O_{2(gas)} + xe^-$$ 　　　　　Eq. V-11

$$2H_2S_{(ads)} + 3O_{2(ads)}^{x-} \Leftrightarrow 2SO_{2(gas)} + 2H_2O + 3xe^- \qquad x = 1, 2$$ 　　　Eq. V-12
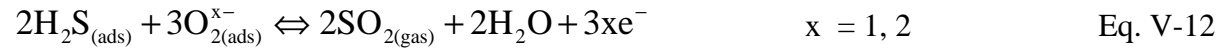
Comparing the maximum sensitivity values (1.84 for 1 ppm $NO_2$ and 1.8 for 12 ppm $H_2S$) we can say that the ZnO sensor is more sensitive to $NO_2$ at lower concentration and lower operating temperature.

Taking into account that the maximum sensitivity (with a peak) of ZnO is obtained at 300 °C for 1ppm $NO_2$ and at 450 °C for 12 ppm $H_2S$ (with no peak), the optimum operating temperature of 300 °C was chosen to study further the $SO_2$ response and the influence of the gas concentration on the film sensitivity.

The ZnO films were tested at 300 °C to 20 ppm $SO_2$ and they exhibit no sensitivity.

**V.2.2.3.　Influence of the gas concentration on the $NO_2$ sensor response**

The sensitivity as a function of $NO_2$ concentration (1 to 5 ppm) at 300 °C is reported in Fig. V-6. The sensitivity shows a clear almost linear (from 1.76 to 3.6) increase, with the increase of the gas concentration from 1 to 5 ppm $NO_2$.

**V.2.2.4.　Influence of the gas concentration on the $H_2S$ sensor response**

The sensitivity of the films was also studied as a function of the $H_2S$ concentration (1-12 ppm) at 300 °C (Fig. V-7). The sensitivity increases slightly almost linearly (from 1.02 to 1.24), when increasing the gas concentration from 1 to 12 ppm $H_2S$.
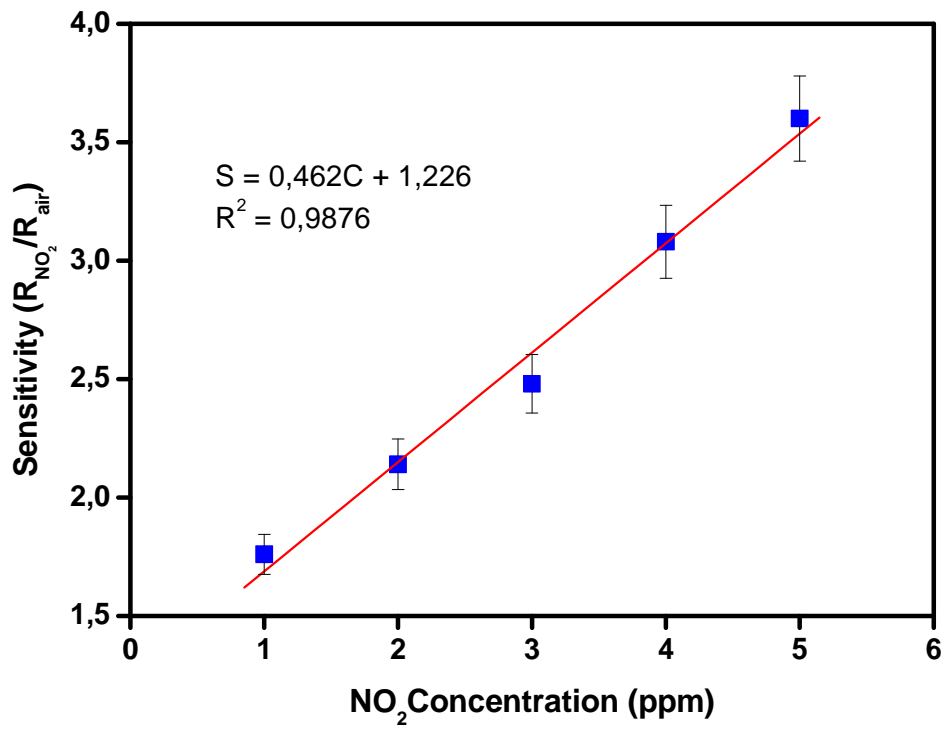
*Figure V-6: The sensitivity of the ZnO sensor at 300 °C to various concentrations of NO₂.*
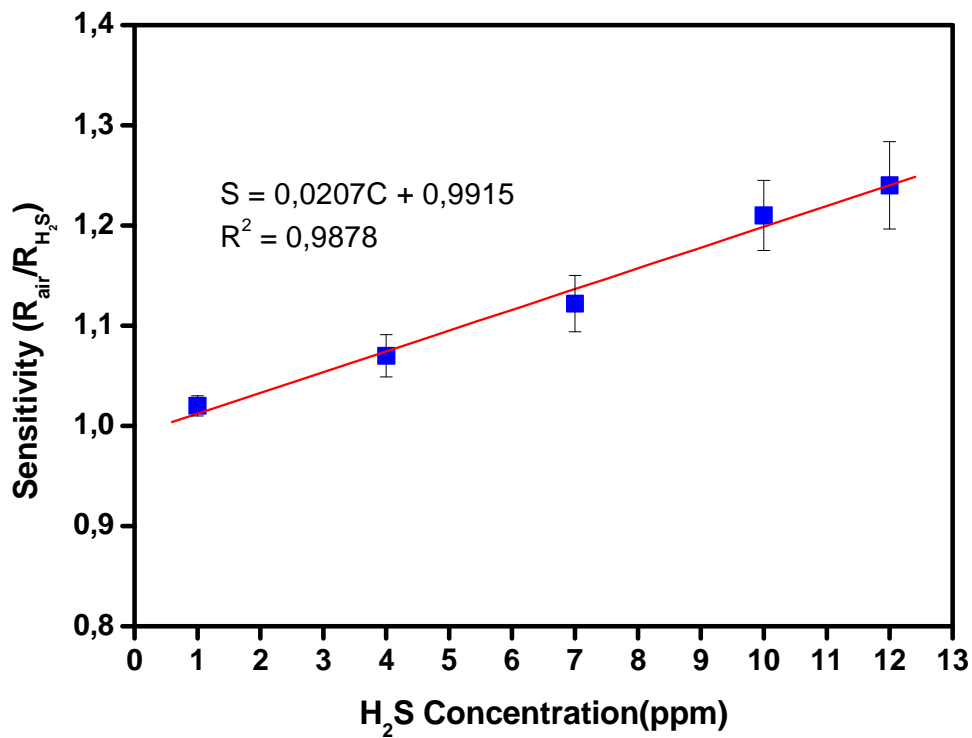


*Figure V-7: The sensitivity of the ZnO sensor at 300 °C to various concentrations of H₂S.*

**V.2.2.5. NO₂ gas sensor cross-sensitivity to H₂S and SO₂**

Considering that in the atmosphere there are many different pollutant gases, the possibility to detect a specified desired gas is of great interest.

Because ZnO presents a maximum sensitivity at 300 °C for $NO_2$, it is necessary to verify whether any cross-sensitivity to $H_2S$ and $SO_2$ exists.

In Fig. V-8, the sensitivity of ZnO films at 300 °C to 1 ppm $NO_2$ (1.84) is much higher than that of 10 ppm $H_2S$ (1.21) and 20 ppm $SO_2$ (1.02), revealing that there is no $NO_2$ cross-sensitivity with the other two gases. It can be predicted also that the ZnO films can be selective sensors if $NO_2$ has to be detected from a mixture comprising these three gases.
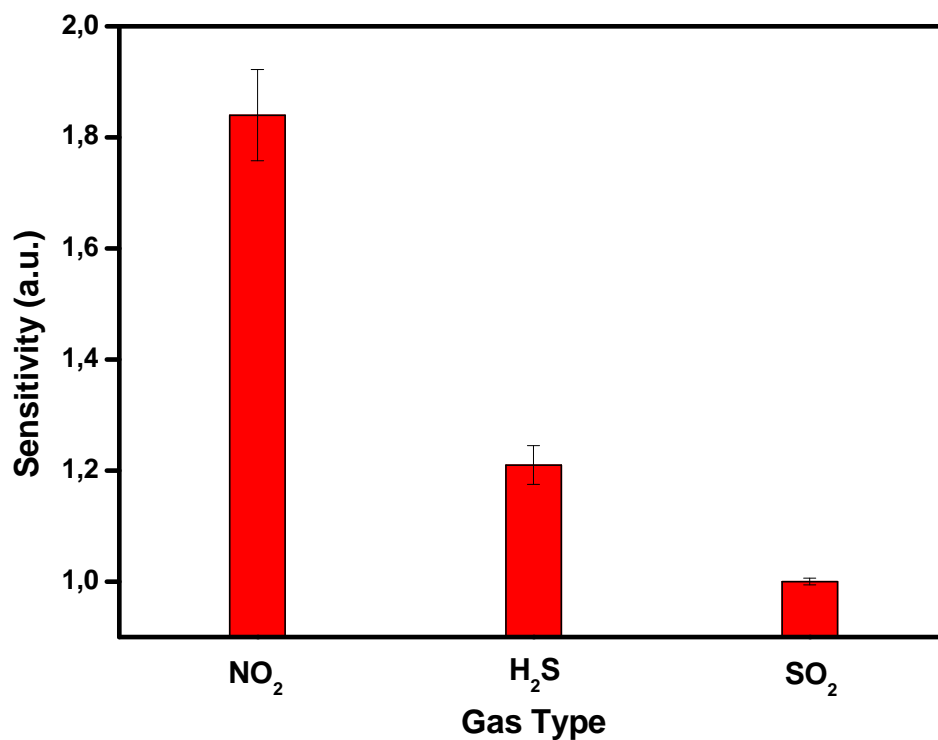


*Figure V-8: ZnO sensitivity to 1 ppm NO₂, 10 ppm H₂S and 20 ppm SO₂ at 300 °C operating temperature.*

All the gas-sensing measurements have been repeated at least three times in order to ensure reproducibility. Furthermore, the measurement error estimation has a minimum of 1.5% and does not exceed 5%.

## V.3.   CONCLUSIONS

In this work we have presented the optimisation of the deposition process of ZnO films using the ESD technique along with their morphological, structural, and gas sensing characterization.

The zinc oxide films have been deposited at 350 °C by tuning the deposition time and the flow rate. The SEM characterization allowed the selection of the best deposition parameters to obtain porous, homogeneous, well-covered ZnO films. The obtained layers are pure, they crystallize in the hexagonal wurtzite structure and they present grains in the nanometer range as showed by XRD and Raman methods.

The films are able to detect a low concentration of $NO_2$ (1ppm) at 300 °C and the sensitivity follows a clear and almost linear dependence on the concentration. The cross-sensitivity to 12 ppm $H_2S$ shows a lower response of the films to this gas compared with that of 1ppm $NO_2$. Furthermore, the films show no response to 20 ppm $SO_2$.

The results of this work indicate that the ESD technique is a reliable method for the preparation of nano-porous zinc oxide, which can detect a low concentration of $NO_2$ with no-cross sensitivity to $H_2S$ and $SO_2$.

# CHAPTER VI:

## GAS SENSORS BASED ON INDIUM OXIDE

# VI.  GAS SENSORS BASED ON INDIUM OXIDE

## VI.1.  INTRODUCTION

Properties as high transparency in the visible region and high electrical conductivity make $In_2O_3$ a suitable material for application in solar cells [162,163], optoelectronic devices [164], liquid-crystal displays [165], etc. Several deposition techniques have been used for the deposition of $In_2O_3$ films including Chemical Vapour Deposition [166], RF and DC sputtering [167,168], sol gel [169,170], and spray pyrolysis [171,172]. To our knowledge there is no paper in the literature describing the deposition of indium oxide using Electrostatic Spray Deposition technique [173].

During recent years $In_2O_3$ became a very interesting material for gas sensor applications, being the best material which allows detection of ozone in the ppb range [174,175] and presents high-selectivity detection of CO in the presence of $H_2$ [176].  Many papers have presented the $In_2O_3$ sensor as a detector for $NO_2$ [32,177-179] and only a few showed the $H_2S$ sensing properties of $In_2O_3$ [161,180] but none of them using electrostatically sprayed indium oxide. Several authors [30,181] showed that the response of $In_2O_3$ to $NO_2$ is improved by doping with $SnO_2$. The amounts of dopant presented in these papers are between 50 and 65 wt. %. Considering that, using such high amounts of $SnO_2$, mixtures will be obtained instead of solid solutions.  So, in this study smaller quantities, i.e., 2 at. % Sn are preferred.

In this chapter the deposition of $In_2O_3$ and Sn-doped $In_2O_3$ films using the ESD technique is presented. The film morphological and structural features are examined employing different characterization techniques. In addition, the layer sensing responses to $H_2S$, $SO_2$ and $NO_2$, which have not yet been described in the literature, will be presented.

## VI.2.   RESULTS AND DISCUSSIONS

### VI.2.1. Morphology and Structure Characterizations

#### VI.2.1.1.        Scanning Electron Microscopy

Considering the previous studies concerning the optimization of the film deposition process (Chapters IV and V), it is obvious that films with porous morphology are obtained at deposition temperatures between 350 and 400 °C using flow rates between 1 and 2 ml/h and deposition times from 1 to 2 h. Therefore, it has been decided to deposit $In_2O_3$ films at 400 °C (1.5 ml/h for 1 h) and the obtained morphology is the desired one. Five more films were deposited with these deposition parameters in order to ensure reproducibility.

A typical surface morphology of an indium oxide film deposited at 400 ºC on Pt-coated alumina is presented in Fig. VI-1a. The as-deposited films were annealed in air for 2h at 500 ºC (Fig. VI-1b) to facilitate the removal of any possible organic residue remained from the precursor solution and also for sintering. Literature shows [182] that a temperature of 500 ºC is sufficient to obtain crystalline indium oxide films [183]. Because the electrical response of the indium oxide sensor is usually investigated in the temperature range of 20-500ºC [178,184,185] an annealing temperature of 500 ºC also ensures the morphology and the microstructure stability of the films. In fact, higher annealing temperatures than 500 °C were not used in order to avoid the increase of the particle size [32,186], or the decrease in crystallinity [32], which further induces a decrease in the gas sensor response [32,186,187].

Fig. VI-1 reveals that the morphology of the non-annealed film (Fig. VI-1a) does not change significantly after the thermal treatment at 500 ºC (Fig. VI-1b) and only a slight increase of the particle size is noticed. Fig.VI-1b shows that the film has a porous morphology. The formation of this type of morphology is due to the high evaporation rate of the solvent, which occurs partially during the flight of the solution towards the substrate, especially for the present high deposition temperature, but also partially during the solution impact on the heated substrate. The evaporation of the solvent has as a result the shrinkage of the droplets, hence, the higher the deposition temperature is, the smaller the particles will be. Due to the high rate of solvent evaporation the Rayleigh limit is reached and the droplets are disrupted into very tiny particles [188].

The film comprises aggregates with dimensions between 5 and 10 μm. These aggregates are agglomerations of very fine particles and their size distribution is almost uniform. The particle agglomeration can be due to the process of "preferential landing" of the droplets, described already in Chapter III. This process causes the agglomeration of the particles especially when the incoming droplets are small (high deposition temperature). The roughness of the alumina substrate surface also enhances preferential landing and leads to the formation of more particle agglomerates [189].
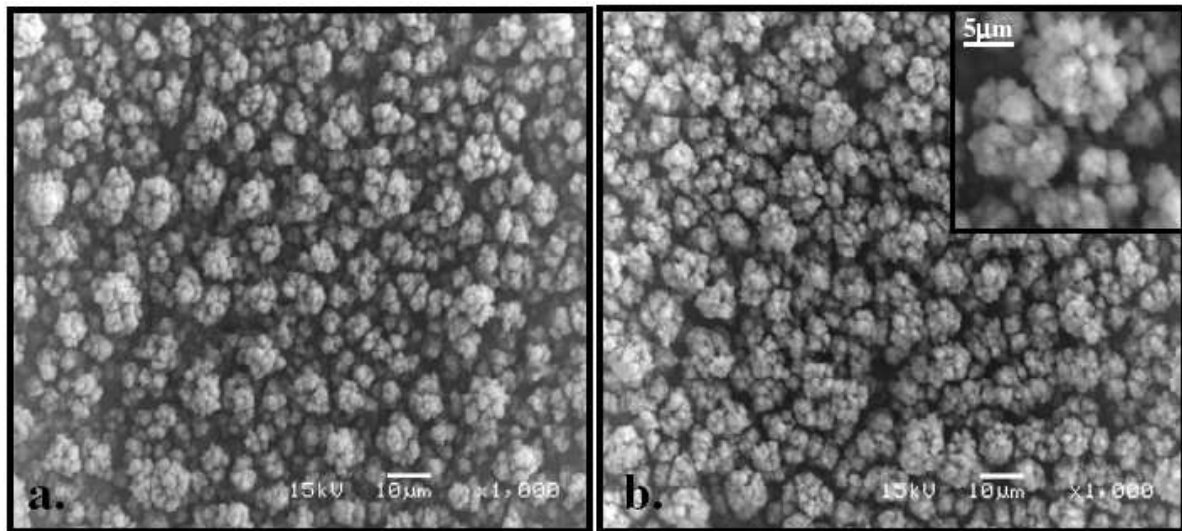


**Figure VI-1***: SEM pictures of an In₂O₃ film deposited at (a) 400 ºC (1.5 ml/h for 1h) and (b) deposited at 400 ºC and annealed at 500 ºC in air for 2h.*

### VI.2.1.2. X-ray Diffraction

The phase composition of the non-annealed films and the effect of the thermal treatment on their crystallinity were examined with the XRD technique. The influence of the tin oxide dopant on the microstructure is also presented.

The XRD patterns of the In₂O₃ films deposited at 400 ºC and annealed at 500 ºC are depicted in Fig. VI-2a. The as-deposited films were amorphous and after the thermal treatment they became crystalline. The observed sharp diffraction peaks indicate a high degree of crystallinity. The XRD pattern shows the main peaks at 4.135Å (211), 2.919Å (222), 2.527Å (400) and 1.787 Å (440). Other peaks corresponding to the planes (411), (332), (431), (521), (433), (611) and (541) are observed but their intensity is lower comparing to that

of the (222) peak. Furthermore, the peaks from (400), (411) and (433) overlap with the alumina substrate ones (Fig. VI-2c). These results matched with those of the cubic structure of indium oxide (called also the C-type rare-earth oxide structure) with the lattice constant a = 10.112 Å are in good agreement with data reported in JCPDS 06-0416. No peaks of impurities are observed.

The degree of the $In_2O_3$ film texture was calculated as ratio I (400)/I (222) of the most intensive peaks in the XRD pattern of $In_2O_3$ and was found to be 0.29. This result suggests that the film is randomly orientated with respect to the substrate and has no preference for any particular orientation [186].

Other information in the present XRD pattern concerns the influence of the tin dopant on the indium oxide microstructure. The XRD pattern of $In_2O_3$ compared with that of tin oxide- doped $In_2O_3$ shows no shift in the $In_2O_3$ peak positions and no Sn phase formation (i.e., Sn oxides or ternary compounds with Sn) (Fig. VI-2 b). Two doping mechanism of $In_2O_3$ with $SnO_2$ are possible: A. substitutional and B. interstitial. In the case of substitutional doping some $Sn^{4+}$ ions take the place of $In^{3+}$ (Eq. VI-1), while in the second case $Sn^{4+}$ ions can occupy the interstitial sites of the $In_2O_3$ lattice (Eq. VI-2).

A. Substitutional:

$$2SnO_2 \xrightarrow{\phantom{xx}In_2O_3\phantom{xx}} 2Sn_{In}^{\cdot} + 3O_o^x + \frac{1}{2}O_2 + 2e^{'} \qquad \text{Eq. VI-1}$$

B. Interstitial:

$$2SnO_2 \xrightarrow{\phantom{xx}In_2O_3\phantom{xx}} 2Sn_i^{\cdots\cdots} + 2V_{In}^{'''} + 3O_o^x + 2e^{'} + \frac{1}{2}O_2 \qquad \text{Eq. VI-2}$$
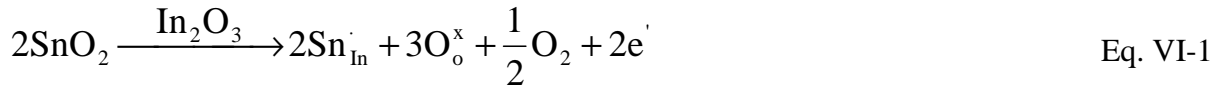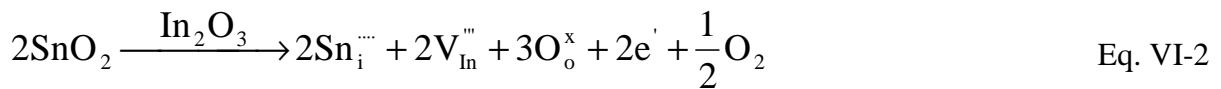
Where, in the Kröger-Vink notation: $Sn_{In}^{\cdot}$ - is a tin ion sitting on an indium lattice site, with positive charge; $O_o^x$ - is an oxygen ion sitting on an oxygen lattice site, with neutral charge; $V_o^{\cdot\cdot}$ - is an oxygen ion vacancy, with double positive charge; $Sn_i^{\cdots\cdots}$ - is a tin interstitial ion, with four positive charges; $V_{In}^{''''}$ - is an indium ion vacancy, with three negative charges. Between the two presented doping mechanisms, usually the substitutional one is much common to occur because it is much difficult to occupy interstitial position. In addition, more defects are formed, as suggested by Eq. VI-2, which is energetically unfavourable.

The average crystallite size was calculated with the Scherrer's equation [190] using the full width at half-maximum of all peaks except the peaks which overlap with the substrate ones. The average crystallite size of $In_2O_3$ and Sn-doped $In_2O_3$ was found to be similar (about 25 nm) with particles exceeding sizes from 20 to 31 nm.
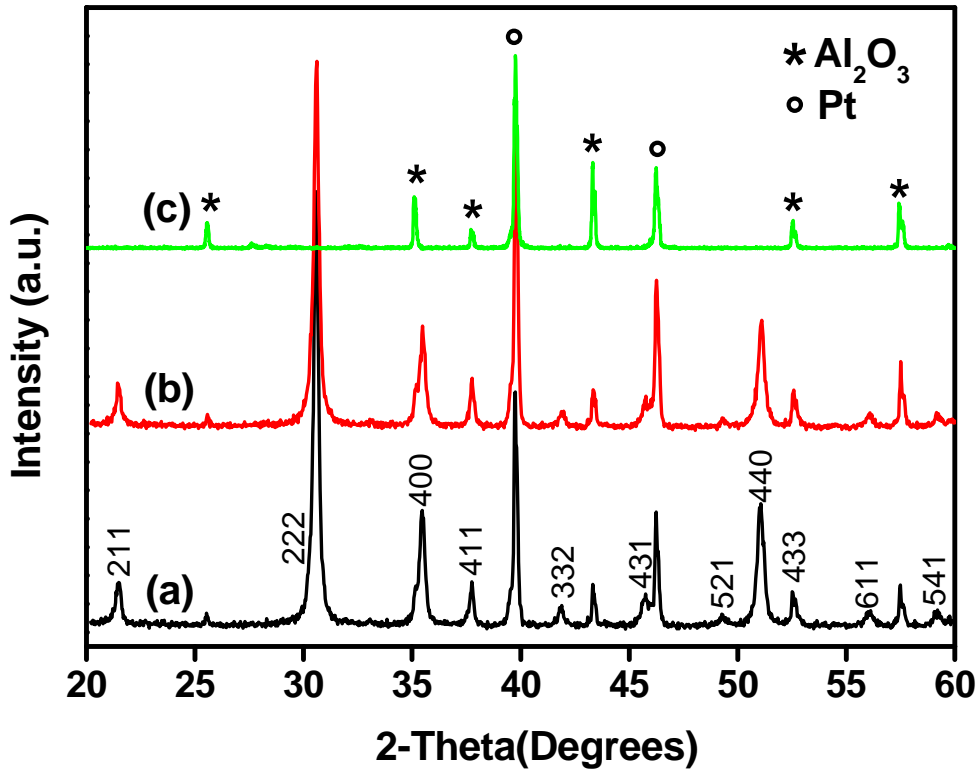


*Figure VI-2: XRD patterns of (a) $In_2O_3$ (b) Sn-doped $In_2O_3$ film deposited on Pt-coated alumina at 400ºC and annealed at 500ºC in air for 2h and (c) Pt-coated alumina substrate.*

From the XRD studies it is concluded that the $In_2O_3$ films crystallize in the cubic phase, which is the phase most studied in the literature for gas sensor applications. No tin phases are detected after the $In_2O_3$ doping procedure, and no significant microstructural changes are observed.

### VI.2.1.3.    Transmission Electron Microscopy and Energy Dispersive X-ray Analysis

The transmission electron micrographs of $In_2O_3$ (Fig.VI-3a) show an irregular shape of the grains. The crystallite size distribution is almost uniform with grain size of about 25 nm,

which is in agreement with the results obtained by XRD evaluation (20-31 nm). Particles exhibiting a size of almost 50 nm, have however been observed.

The grain size depends mainly on the precursor solution flow rate and its properties, especially conductivity, according to Eq. III-1.

The TEM picture in Fig. VI-3b reveals the lattice fringes for a few $In_2O_3$ grains, showing the nanocrystalline phase of the film. One of the main lattice fringes observed in Fig. VI-3b belongs to the (222) lattice plane of the cubic $In_2O_3$ nanocrystal.
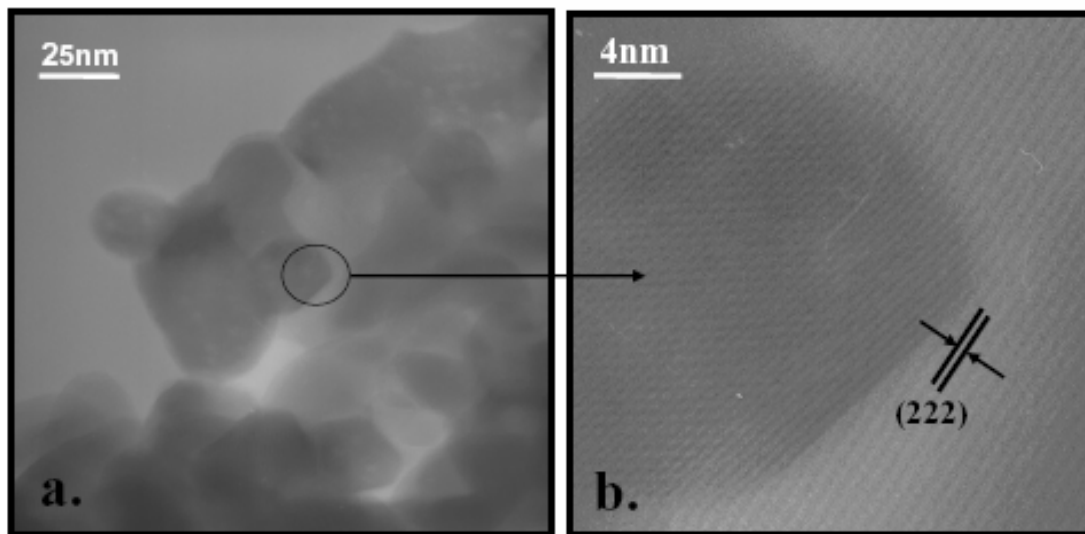


***Figure VI-3: TEM photographs of a grinded In₂O₃ film deposited on Pt-coated alumina at 400 ºC and annealed at 500 ºC in air for 2h using (a) low and (b) high magnification.***

From a TEM study it is concluded that the $In_2O_3$ films crystallize in the cubic phase and that they comprise crystallites in the range of nanometers, result in good accordance with the XRD data.

In order to examine the chemical composition of the films an EDX analysis was performed on a grinded $In_2O_3$ film deposited at 400 ºC and annealed for 2h at 500 ºC in air. Fig.VI-4 shows the EDX spectrum, in which characteristic peaks of In and O belonging to the $In_2O_3$ structure can be observed. The other peaks, i.e., C and Cu peaks are due to the grid on which the sample was laid. No Cl peaks, which could be due to the precursor solution, are detected in the EDX spectrum suggesting the purity of the films.

*Figure VI-4: EDX spectrum of a grinded In$_2$O$_3$ film deposited on Pt-coated alumina at 400ºC (1.5 ml/h for 1h) and annealed at 500 ºC in air for 2h.*

### VI.2.1.4.   Raman Spectroscopy

The Raman spectrum of the In$_2$O$_3$ film deposited at 400 ºC and annealed at 500 ºC is shown in Fig. VI-5a. Cubic In$_2$O$_3$ belongs to the C-type rare-earth oxide structure and for this type of structure the factor group analysis predicts 4A$_g$ (Raman) + 4E$_g$ (Raman) + 14T$_g$ (Raman) + 5A$_u$ (inactive) + 5E$_u$ (inactive) + 16T$_u$ (I. R.) modes [191]. Characteristic Raman peaks of In$_2$O$_3$ appeared at 135, 307, 365, 496 and 627 cm$^{-1}$, respectively, as shown in Fig. VI-5. All the present modes correspond to the band position reported in the literature for cubic indium oxide [192,193].

The influence of the tin doping on the In$_2$O$_3$ microstructure has also been investigated. Comparing the Raman spectrum of In$_2$O$_3$ film (Fig.VI-5a) with the Sn-doped In$_2$O$_3$ film (Fig.VI-5b), it is observed that after doping the mode intensity is smaller and their width larger. These observations suggest a decrease in the crystallinity and in the grain size. It is seen also that the peaks are not shifted and that no tin oxide peaks appear, confirming that no separate phase is formed. The small mode, which appears at 419 cm$^{-1}$ in the Sn-doped In$_2$O$_3$ spectrum, is due to the alumina substrate as indicated.

The Raman studies confirm the XRD results, i.e., crystallization of the In$_2$O$_3$ in cubic structure with no appearance of other phases due to doping. In addition, the Raman technique provides supplementary information compared with XRD, i.e., a small decrease in the grain size when doping indium oxide with tin oxide.

*Figure VI-5: Room temperature Raman spectra of (a) In₂O₃ and (b) Sn-In₂O₃ films deposited on Pt-coated alumina at 400 ºC and annealed at 500 ºC in air for 2h.*

## VI.2.2. Gas sensing properties

### VI.2.2.1.    Influence of the operating temperature on the H₂S sensor response

For the determination of the temperature corresponding to the H₂S sensitivity maximum, the films were exposed to 10 ppm H₂S in the temperature range of 100 °C to 300 °C by steps of 50 °C. For each day of measurements the temperature was set to a constant value increasing from 100 °C and increasing to 300 °C. Before starting the measurements, the films were regenerated in synthetic air for 60 min and then exposed to H₂S for 30 min. This cycle was repeated 4 or 5 times during a day and then the next temperature was set for the following day. The same procedure was employed every day until all the ranges of temperature were explored.

The In₂O₃ dependence of the H₂S sensitivity ( $R_{air}/R_{H_2S}$ ) to the operating temperature is shown in Fig. VI-6. Because the sensitivity differences between the successive exposure cycles, only three significant cycles are shown.

For the first gas exposure cycle, the 10 ppm H₂S response presents a maximum at 200°C. When the temperature changes from 100 °C to 200 °C, the sensor sensitivity increases

from 6.4 to 175, which is the maximum. Increasing the temperature beyond 200 °C the sensitivity decreases, reaching a value of 1.15 at 300 °C. Literature shows [180] that the maximum $H_2S$ sensitivity using $In_2O_3$ films is observed between 200 and 250 °C, which is in good accordance with the present results. The detection mechanism of $H_2S$ is similar with that presented for ZnO in Chapter V (Eq. V-10 to V- 12).

The other two cycles presented in Fig. VI-6 show the same behaviour as the first cycle, but their sensitivity is clearly much lower than the first one. For example, a comparison of maximum sensitivities at 200 °C, reveals that the first cycle has a sensitivity of 175, while the third one has only a response of 17. This behaviour can be due to an incomplete recovery of the film resistance in air ($R_{air}$) after $H_2S$ removal, influencing in this way the sensitivity ($R_{air}/R_{H_2S}$) of the next cycle. If the regeneration is complete (overnight), the $H_2S$ response is reproducible, and the cycles show almost the same sensitivity and behaviour.
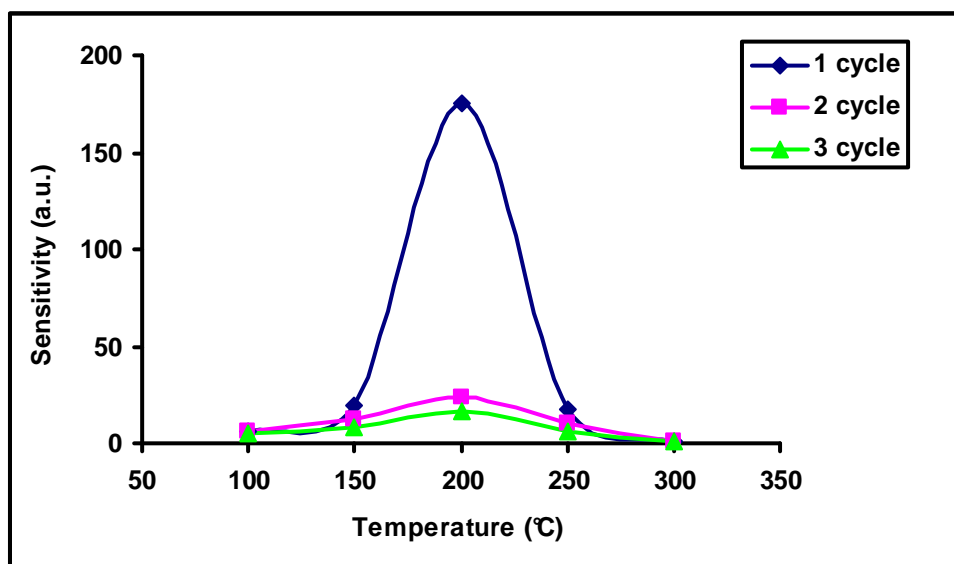


*Figure VI-6: $In_2O_3$ sensitivity to 10 ppm $H_2S$ as a function of the operating temperature.*

In Fig. VI-7 the sensitivity of Sn-doped $In_2O_3$ to 10 ppm $H_2S$ is shown. For the first cycle of gas exposure, the 10 ppm $H_2S$ response presents a maximum for 200 °C. When the temperature changes from 100 °C to 200 °C, the sensor sensitivity increases from 1.7 to 8.3, which is the maximum. Increasing the temperature more than 200°C the sensitivity decreases, reaching a value of 1.06 at 300 °C. If compared, the maximum sensitivity at 200 °C for the first cycle of gas exposure with the other two cycles, it is clear that the sensitivity is much lower, i.e., 8.3 for the first cycle respectively 2.6 for the last one.

It is clear that the $H_2S$ maximum sensitivity for the second and third cycles is shifted to 250 °C, compared to the first cycle where the maximum is found at 200 °C. This shift is attributed to the incomplete recovery of the film resistance. Considering that after each cycle, the sensitivity is lower and lower, the maximum sensitivity shifts to 250 °C where the regeneration is better (due to the higher temperature) and the difference between the cycles is not so high compared with that of 200 °C.

The same behaviour was also seen for undoped $In_2O_3$ (Fig. VI-6). The $In_2O_3$ sensitivity is much higher than for Sn-doped $In_2O_3$ one. It can be concluded that the tin oxide did not improve the sensitivity to $H_2S$, on the contrary it decreased it (Fig. VI-7).
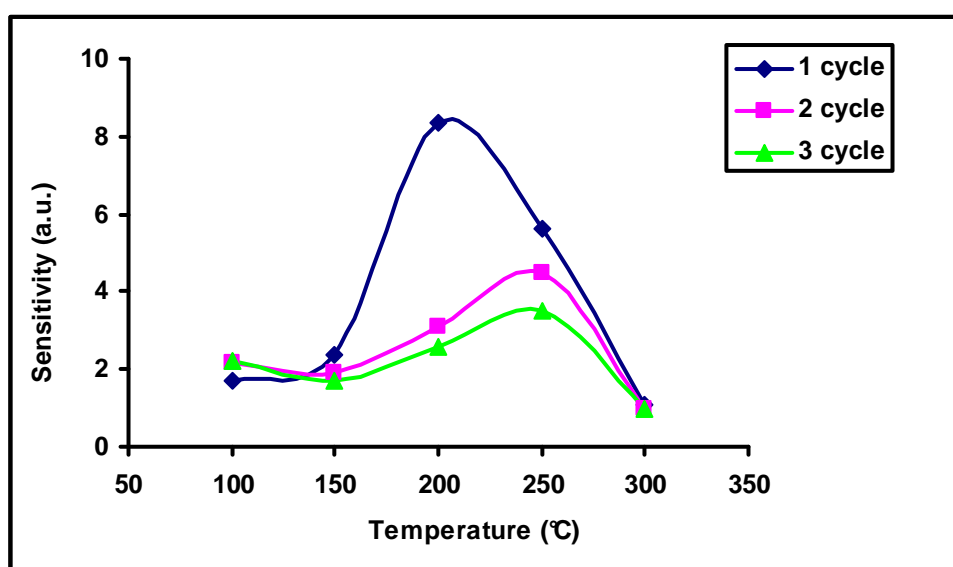


***Figure VI-7: Sn-doped $In_2O_3$ sensitivity to 10 ppm $H_2S$ as a function of the operating temperature.***

Because the highest $H_2S$ sensitivity is exhibited by $In_2O_3$ films at 200 °C, this temperature was selected for further study of the influence of the gas concentration on the sensitivity and also to evaluate the response to $SO_2$ and $NO_2$.

## VI.2.2.2. Influence of the gas concentration on the $H_2S$ sensor response

The sensitivity of undoped $In_2O_3$ and Sn-doped $In_2O_3$ films as a function of the $H_2S$ concentration (1-10 ppm) at 200 °C was also studied (Fig. VI-8 and Fig. VI-9). For all the films the sensitivity increases when the gas concentration increases from 1 to 7 ppm $H_2S$ and when increasing beyond 7 ppm the $H_2S$ concentration, the films show an opposite behaviour.

To explain this characteristic, firstly, it is assumed that the film saturates starting at 7 ppm $H_2S$. Other authors [180] reported saturation of $In_2O_3$ films starting with a concentration of 20 ppm $H_2S$. In a second part, a possible desorption of the gas molecules can explain partly our results.

For undoped and Sn-doped $In_2O_3$, the same sensitivity differences between the first and the last two gas exposure cycles is observed.
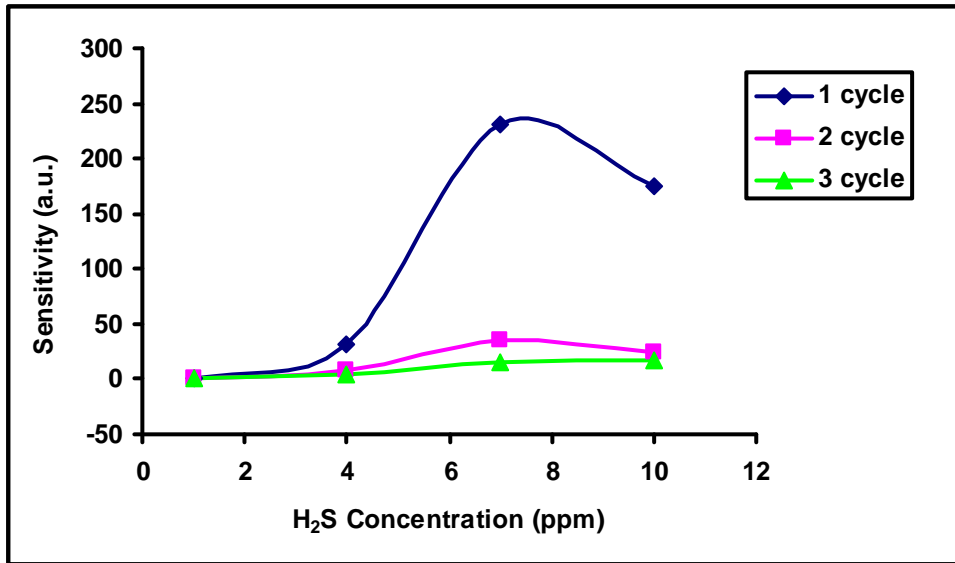


*Figure VI-8: In$_2$O$_3$ sensitivity as a function of H$_2$S concentration at 200 °C operating temperature.*
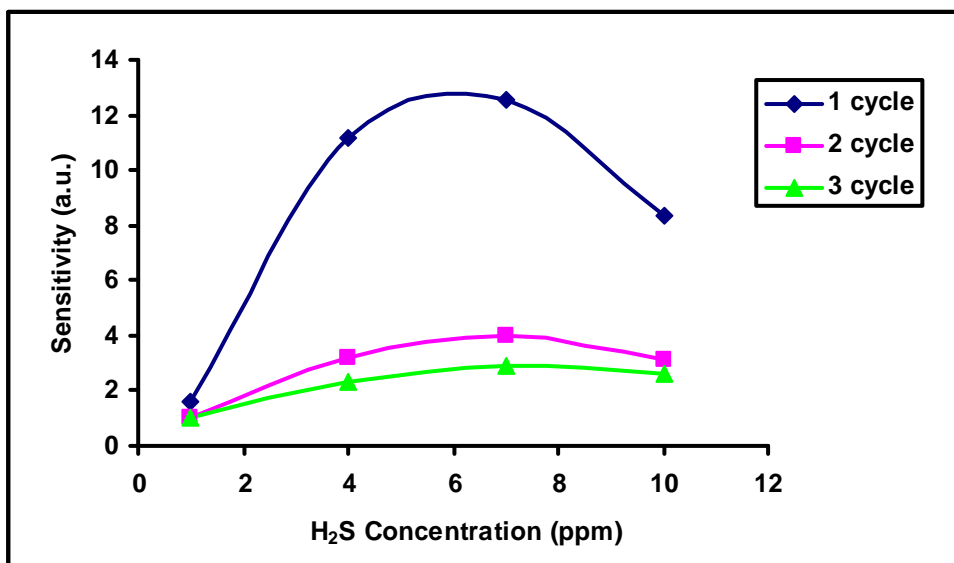


*Figure VI-9: Sn-doped In$_2$O$_3$ sensitivity as a function of H$_2$S concentration at 200 °C operating temperature.*

### VI.2.2.3.   H$_2$S gas sensor cross-sensitivity to SO$_2$ and NO$_2$

#### A.   *Sensor response to SO$_2$*

The response of In$_2$O$_3$ and Sn-doped In$_2$O$_3$ to 20 ppm SO$_2$ at 200 °C is showed in Fig. VI-10 and an improvement of the SO$_2$ sensor sensitivity by doping with tin oxide is observed.
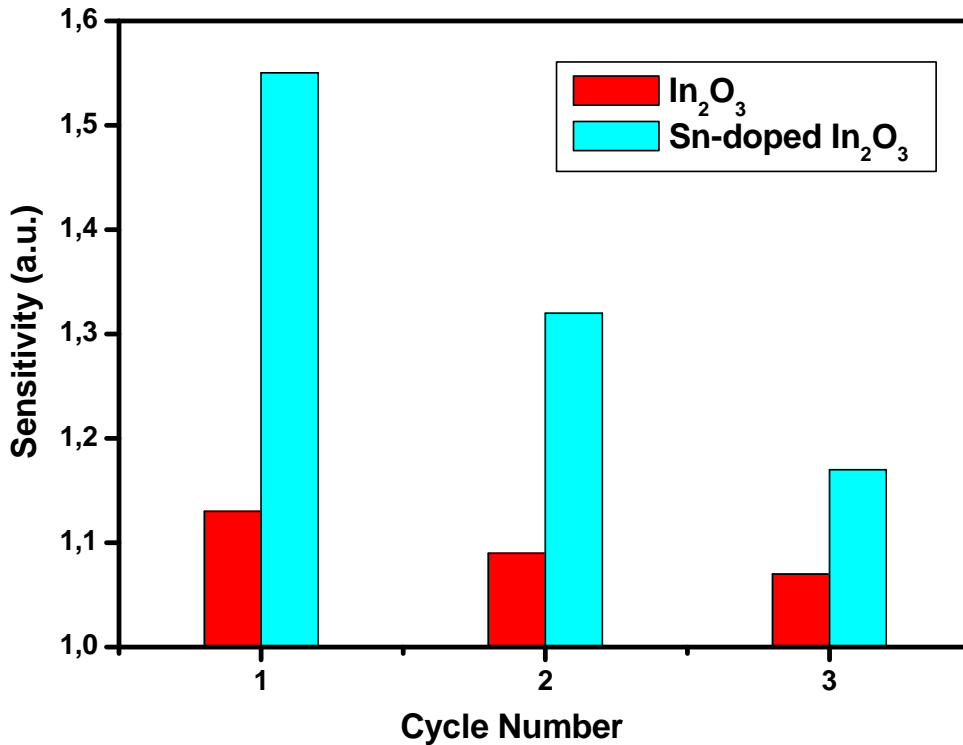


*Figure VI-10: In$_2$O$_3$ and Sn-doped In$_2$O$_3$ sensitivity to 20 ppm SO$_2$ at 200 °C operating temperature.*

#### B.   *Sensor response to NO$_2$*

The sensitivity of In$_2$O$_3$ and Sn-doped In$_2$O$_3$ to 1 ppm NO$_2$ at 200 °C is presented in Fig. VI-11. The sensitivity to NO$_2$ is improved by doping with tin oxide, which has also been reported in the literature [30,114,181]. The NO$_2$ detection mechanism is similar with that presented for ZnO in Chapter V (Eqs. V-5 to 7).

The same gas response differences between the first and the next two gas exposure cycles are observed for SO$_2$ and NO$_2$, like for H$_2$S.
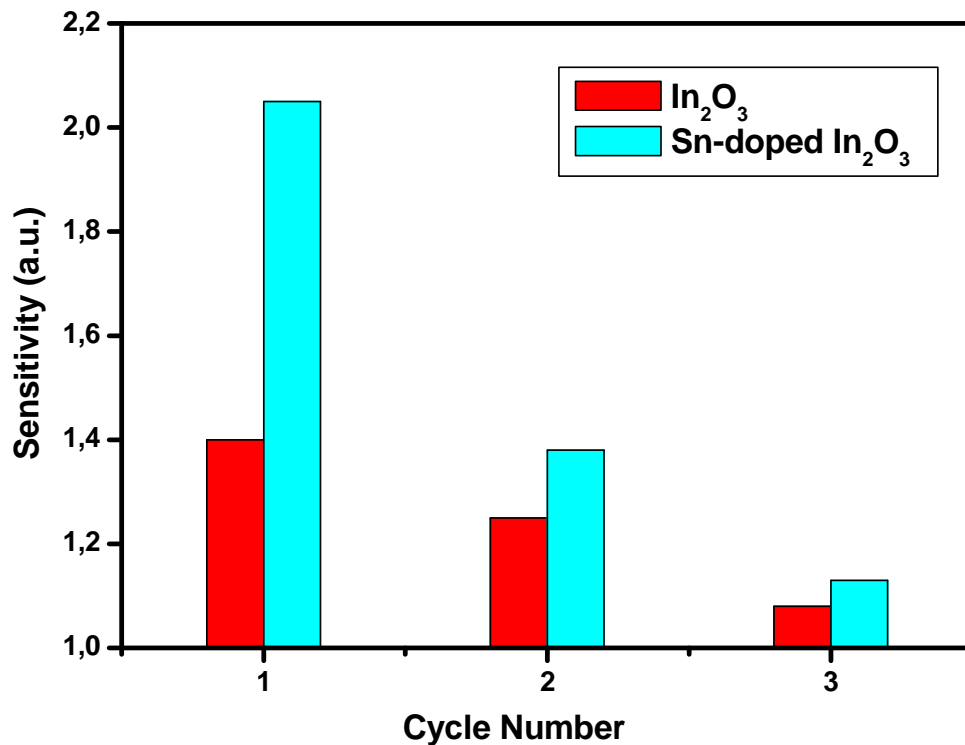
*Figure VI-11: In$_2$O$_3$ and Sn-doped In$_2$O$_3$ sensitivity to 1 ppm NO$_2$ at 200 $^{\bullet}$C operating temperature.*

### C. H$_2$S sensor cross-sensitivity to SO$_2$ and NO$_2$

In Fig. VI-12 the first cycle response of In$_2$O$_3$ and Sn-doped In$_2$O$_3$ to 10 ppm H$_2$S, 20 ppm SO$_2$ and 1 ppm NO$_2$ is presented. It is obvious that the undoped and Sn-doped In$_2$O$_3$ sensitivity to H$_2$S is much larger than the sensitivity to the other two gases, indicating no H$_2$S cross-sensitivity. However, it is also observed that the undoped In$_2$O$_3$ films are more sensitive to H$_2$S, while the Sn-doped In$_2$O$_3$ films are more sensitive to SO$_2$ and NO$_2$. Because of the very low sensitivities to SO$_2$ and NO$_2$ of the doped films, this behaviour will not influence the cross-sensitivity to H$_2$S detection.
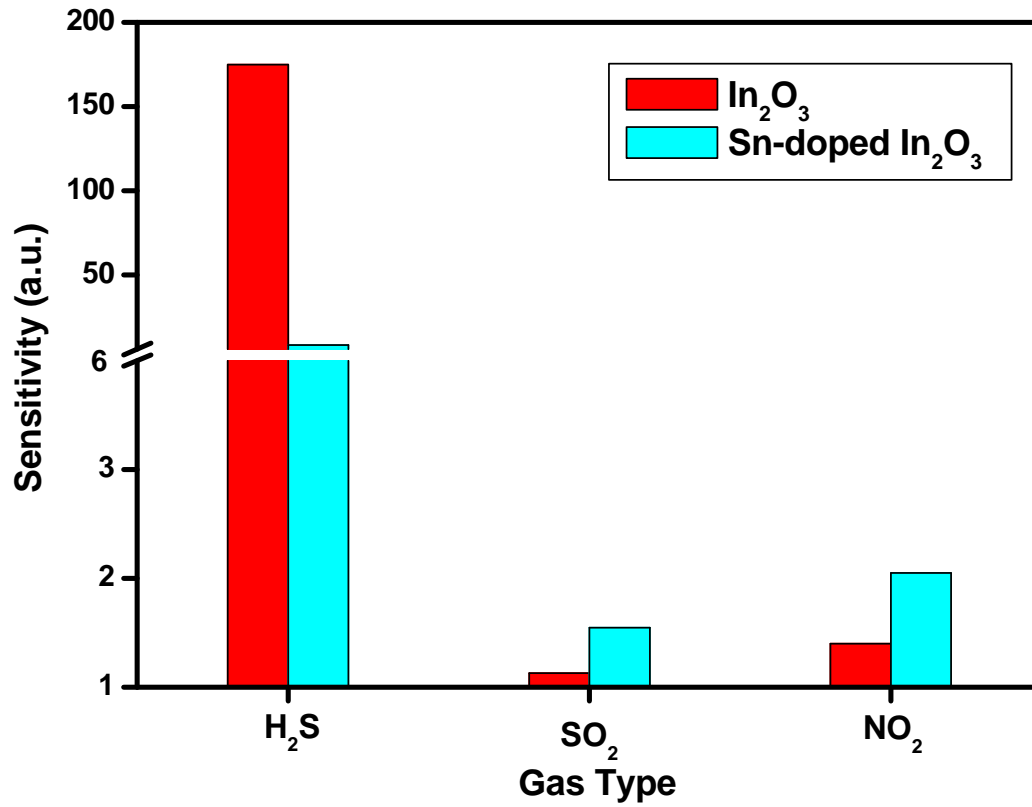
*Figure VI-12: In$_2$O$_3$ and Sn-doped In$_2$O$_3$ sensitivity to 10 ppm H$_2$S, 20 ppm SO$_2$ and 1 ppm NO$_2$ at 200 •C operating temperature.*

## VI.3.   CONCLUSIONS

Porous films of $In_2O_3$ and Sn-doped $In_2O_3$ for gas sensors have been deposited at 400°C on Pt partially-coated alumina substrates using a simple and efficient ESD technique. As shown by XRD and Raman measurements, the $In_2O_3$ films are crystallized in the cubic phase and no modification of the microstructure is observed after the doping procedure (Sn phases or impurities).

Comparing with other semiconducting-based metal oxide sensors, the present films (especially undoped $In_2O_3$) were able to detect low concentrations of $H_2S$ (10 ppm) at low operating temperature (200 °C). Unfortunately, the $H_2S$ response is not fully reproducible using the presented experimental conditions, since after each successive gas exposure cycle the sensitivity decreases considerably. However, upon full regeneration the reproducibility is very much improved, but it takes a long time.

The $H_2S$ sensor response studied as a function of the concentration may indicate that the film is assumed to saturate starting at 7 ppm, so for higher gas concentrations than 7 ppm, a desorption of the gas molecules can be taken into account.

Doping with Sn improves the $In_2O_3$ sensitivity to $SO_2$ and $NO_2$ but the overall sensitivity is much smaller than that to $H_2S$.

The film response to $H_2S$ is the highest at 200 °C with no cross-sensitivity to the other two studied gases, but the reproducibility problem must be solved, by changing the working procedure or perhaps by modifying the morphology, microstructure or by adjusting the type or amount of dopant.
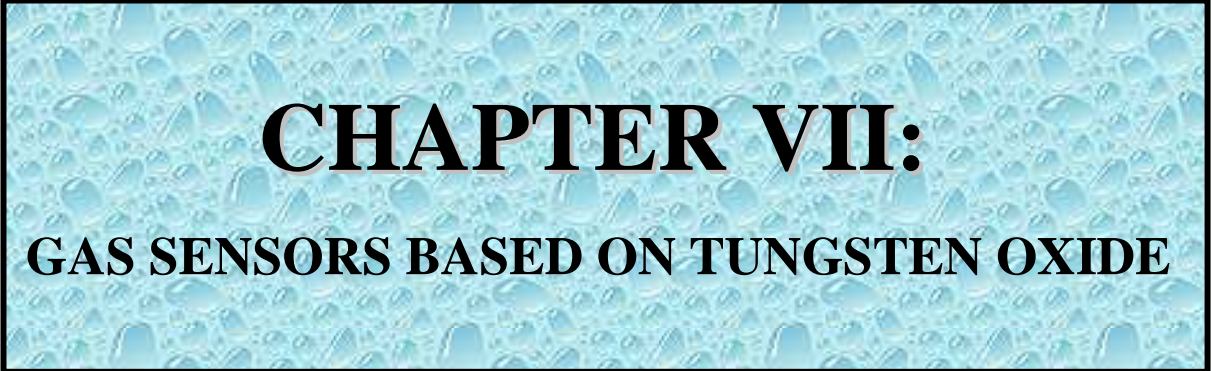
# CHAPTER VII:

## GAS SENSORS BASED ON TUNGSTEN OXIDE

# VII. GAS SENSORS BASED ON TUNGSTEN OXIDE

## VII.1. INTRODUCTION

A tungsten trioxide gas sensor was first reported by Shaver, who observed that the resistance of the $WO_3$ film changes upon hydrogen exposure [194]. Over the time, $WO_3$ proved to be an attractive material for gas sensor applications, mainly used for the detection of $NO_2$ [195-197] but also employed for the detection of other gases, such as $H_2S$ [198] , $SO_2$ [199] , $O_2$ [200] etc. Various methods have been used to improve the gas sensitivity of $WO_3$, including especially the modification of the morphology and the microstructure (i.e., grain size, film thickness, phase) by using different deposition techniques, or by doping with different compounds.

Several techniques have been used to deposit $WO_3$ films including chemical vapour deposition [201], sol-gel [195,202], sputtering [203,204], and spray pyrolysis [205,206]. In this Chapter the Electrostatic Spray Deposition technique is reported for the first time for the deposition of $WO_3$ films [207]. This method was selected for the preparation of $WO_3$ layers, considering that it allows an easy control of the film morphology and composition.

Because the $WO_3$ precursors are particularly unstable, we have tested several ones in order to obtain good quality $WO_3$ films. After the selection of the suitable precursor, the films were deposited varying the temperature. The morphology and microstructure of the layers has been evaluated using different techniques, i.e., SEM, XRD, TEM, and Raman Spectroscopy. The $WO_3$ response to different pollutant gases, $H_2S$, $SO_2$, and $NO_2$, have been presented as a function of the operating temperature, and also as a function of the gas concentration.

## VII.2.  RESULTS AND DISCUSSIONS

### VII.2.1.  Choice of the precursor solution

Because of the instability of the $WO_3$ precursors, several ones have been tested in order to obtain good quality films, for several ESD experimental conditions (flow rate, nozzle-to-substrate distance, and deposition time) [208].

Firstly, the **_tungsten ethoxide_** precursor has been used. It presents the advantage to be commercially available and, moreover, the obtained $WO_3$ films are pure as shown by the XRD pattern from Fig. VII-1 a. The precursor has the disadvantage of being expensive and sensitive towards moisture.
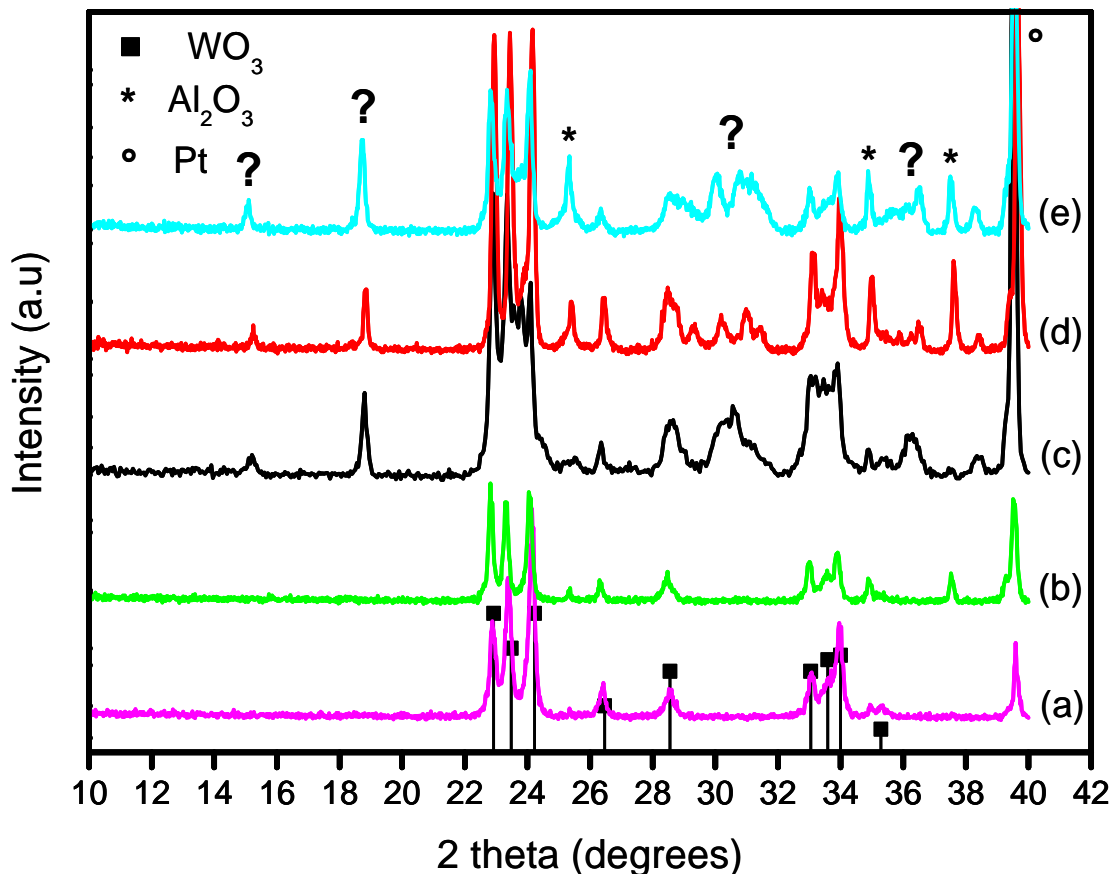


***Figure VII-1: XRD patterns of $WO_3$ obtained from different precursor solutions:***

***(a) W(EtOH)$_6$ (b) PTA (c) WCl$_6$ (d) WOCl$_4$ (e) (NH$_4$)$_2$WO$_4$.***

Then the ***peroxotungstic acid (PTA)*** precursor was tested. Because the material is not commercially available it had to be prepared according to the flow chart presented in Chapter III (Fig. III-7). Evaporating the peroxotungstic acid solution different powders were obtained depending on the evaporation temperature. When the solution was slowly dried at room temperature *(**20-25°C)** crystalline white powders were obtained corresponding to a $WO_3 \cdot H_2O_2 \cdot H_2O$ phase (Fig. VII-2), described in the literature [209]. This powder did not dissolve in ethanol, so it could not be sprayed to obtain $WO_3$ films.
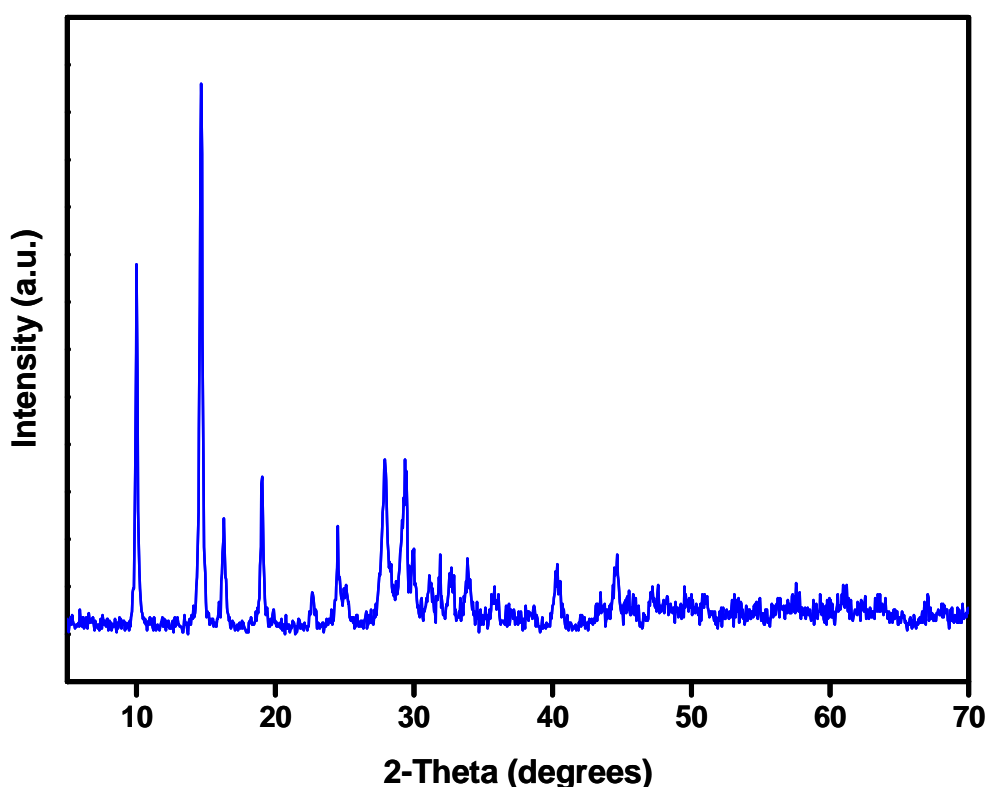


***Figure VII-2: XRD pattern of WO₃·H₂O₂·H₂O powder obtained by drying the PTA solution at room temperature.***

The PTA solution was also evaporated at **60** °**C** and orthorhombic hydrate tungsten oxide ($WO_3 \cdot 1/3H_2O$) was obtained as observed in the XRD spectra presented in Fig. VII-3 [210]. This compound is a yellow crystalline powder insoluble in ethanol, and therefore, not suitable to obtain $WO_3$ films with the ESD technique.

If fast evaporation of the solution was employed (about **90** °**C**) a yellow-orange amorphous powder, soluble in alcohol, was obtained. Upon spraying this solution, a pure $WO_3$ layer was obtained as showed by XRD spectra (Fig. VII-1b).
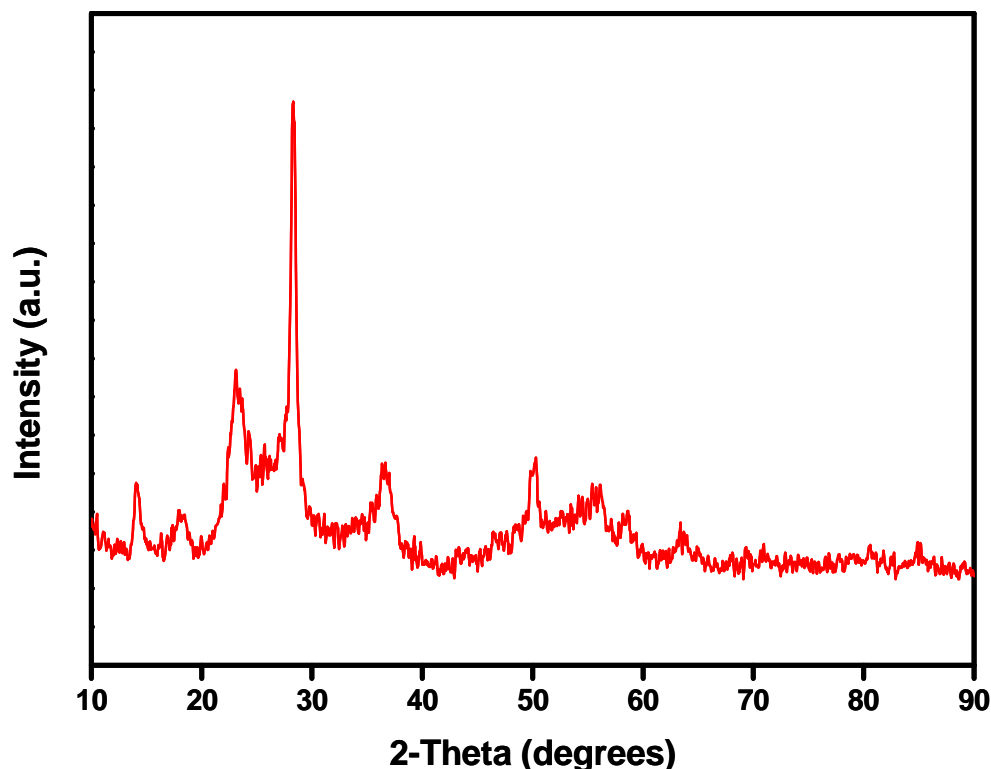
*Figure VII-3: XRD pattern of WO$_3$·1/3H$_2$O powder obtain by drying the PTA solution at 60°C.*

The peroxotungstic acid precursor which allows the deposition of pure WO$_3$ films is not commercially available. It could be a cheap precursor but it has to be fabricated and the preparation process cannot easily be controlled, demanding further studies. It has been observed that during the time the prepared powder initially soluble in ethanol became insoluble probably due to the adsorption of water from the atmosphere, which modifies the powder chemical composition.

The ***tungsten chloride***, ***tungsten oxochloride*** and ***ammonium tungstate*** have also been tested. They are sensitive to moisture and especially the first one is more reactive and very fast reduced by organic solvents, giving blue solutions of W$^{5+}$, hence other chemical processes have to be applied to stabilize the solution (as shown in Chapter III.2.4).

Furthermore, upon spraying these three solutions the following problem has been found: in contact with the metallic nozzle or other metallic parts of the syringe, the solution colour changed from colourless to blue (i.e., W$^{6+}$ is reduced to W$^{5+}$). It has been noticed that the WO$_3$ film contains unknown impurities as shown by XRD measurements (Fig. VII-1 c, d, e).

So, it was decided to do not employ these precursor solutions for the deposition of $WO_3$, considering that the obtained films are not pure.

Taking into account the advantages and disadvantages of the used precursors it is believed that tungsten ethoxide is the most suitable one for the preparation of $WO_3$ films, considering its purity and its commercially availability.

## VII.2.2. Morphology and Structure Characterizations

### VII.2.2.1. Scanning Electron Microscopy and Energy Dispersive X-ray Analysis

Because the temperature is the parameter influencing mostly the morphology of the films, the temperature was varied between 200 and 400 °C in order to obtain porous $WO_3$ films.

Fig.VII-4 shows the differences in the morphology of the $WO_3$ films deposited at different substrate temperatures ranging from 200 to 400 ºC. Four types of film morphology can be deposited by the ESD method and they are described by Chen et al. [83] as dense, dense with incorporated particles, dense bottom layer with a porous top layer, and fractal-like porous depending on the deposition temperature.

The film deposited at 200 ºC (Fig. VII-4 a) is a smooth dense film. This morphology can be obtained from the incomplete evaporation of the droplets solvent when arriving on the substrate. The film shows cracks, which can be due to the stress built-up during the drying process in air.

When the film is deposited at 300 ºC (Fig. VII-4 b) the morphology changes to dense with incorporated particles and consists mainly of large particles (5-10 µm) which are uniformly distributed. Moreover, the particles seem to be embedded in a dense matrix and no cracks are observed in this case. We suppose that the droplets arriving on the substrate are still wet due to the incomplete solvent evaporation.

Choosing a deposition temperature of 350 ℃ (Fig. VII-4c) the morphology reveals a porous layer with a dense bottom layer. This film comprises particles with diameters of 1-5 µm and aggregates (10 µm) which are agglomerates of very small particles.

If the deposition takes place at 400 ℃ (Fig. VII-4d) highly porous $WO_3$ films are formed due to the complete solvent evaporation before arriving at the substrate surface. The film comprises agglomerates of very fine particles. The particle agglomeration is ascribed to "preferential landing" of the aerosol droplets [189]. This type of morphology is preferred for gas sensing applications, but, unfortunately, this film reveals poor adhesion to the substrate.

It is concluded that increasing the deposition temperature the porosity increases as well, while the particle size decreases. Considering the influence of the deposition temperature on the morphology of the films, it is clear that upon increasing the temperature from 200 ℃ to 400 ℃ the film morphology changes from dense to a highly porous one. A compromise between the porosity and adhesion was done, and films deposited at 350 °C (Fig. VII-4c) were chosen for further structure and gas sensing investigations. To ensure the reproducibility 5 films were prepared using the selected deposition parameters.
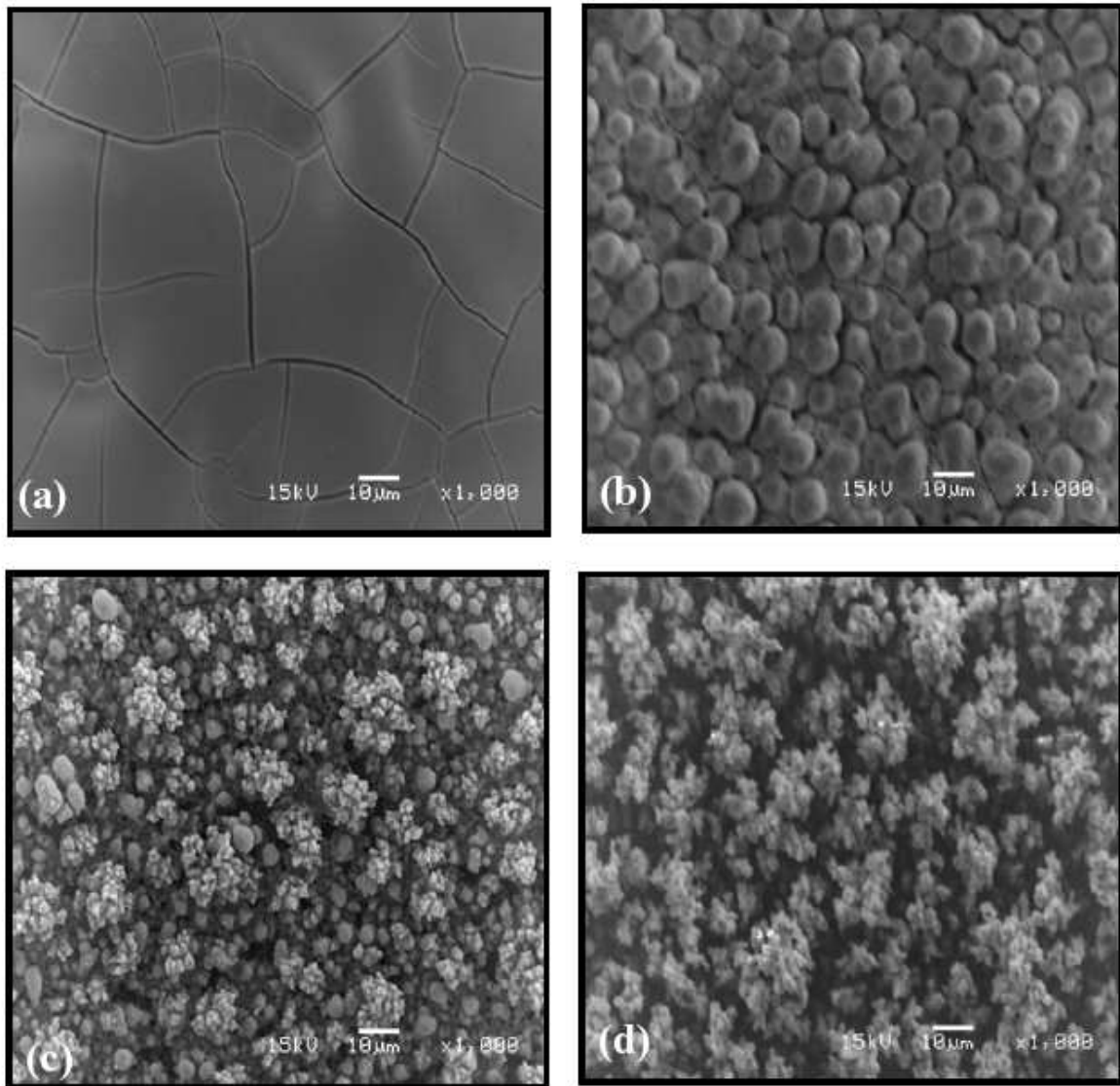
*Figure VII-4: SEM pictures of WO₃ films deposited with 1ml/h for 1h using different deposition temperatures: (a) 200 ℃, (b) 300 ℃, (c) 350 ℃, (d) 400 ℃.*

Fig. VII-5 shows the EDX spectrum of a WO₃ film deposited at 350 ℃ and annealed at 500 ℃ for 2h in air. Only peaks related with tungsten (W) and oxygen (O) are present confirming the film composition without any impurities.
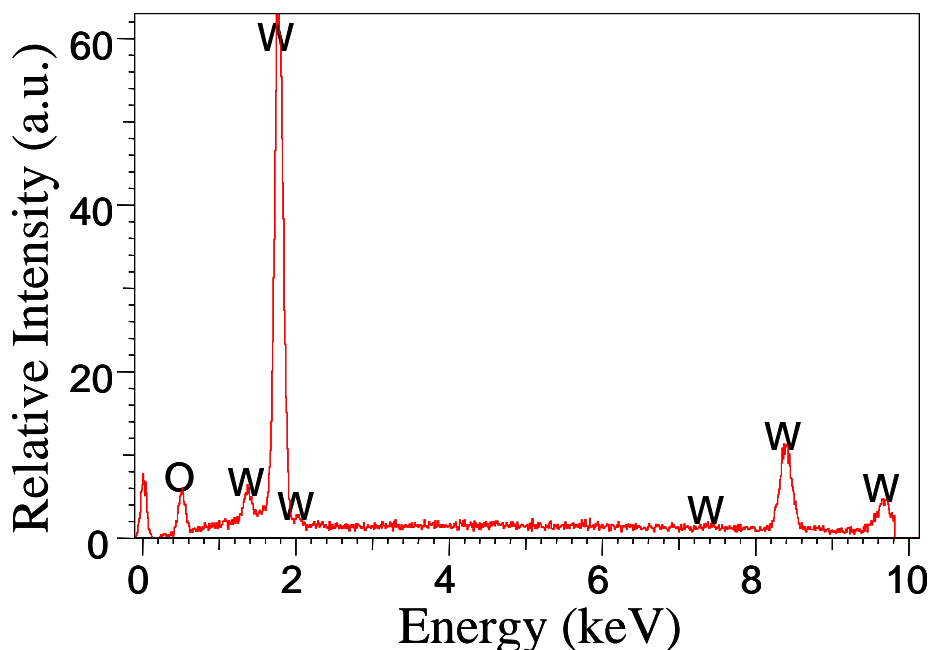
*Figure VII-5: EDX spectrum of a WO₃ film deposited at 350 °C (1ml/h for 1h) and annealed at 500°C for 2h in air.*

### VII.2.2.2. X-ray Diffraction

The phase composition of the non-annealed films and the effect of the thermal treatment on the film crystallinity, were examined by the XRD technique. The non-annealed films exhibit a black colour and after annealing, when the organic rests of the precursor solution are removed, the colour changes to yellow-green, which is specific for $WO_3$.

The XRD pattern of a $WO_3$ film as-deposited at 350 °C (Fig.VII-6a) and annealed at 500 °C (Fig.VII-6b) in comparison with the Pt-alumina substrate pattern (Fig.VII-6c) is shown in Fig.VII-6. It is noticed that after annealing the $WO_3$ films become more crystalline with three predominant peaks, i.e., (200), (020) and (002). The lattice constants calculated from the positions of the diffraction peaks are found to be a = 7.678 Å, b = 7.548 Å, and c = 7.342 Å, which is in good agreement with the JCPDS 72-0677 for monoclinic $WO_3$.

Three distinct XRD peaks for the monoclinic form have been reported in the literature at $2\theta$ equal to 23.14°, 23.70°, and 24.40° corresponding to d = 0.385, 0.375, 0.364 nm [211]. These peaks correspond to the (200), (020), and (002) planes. In the present pattern the peaks corresponding to these planes are found to be equal to 0.384, 0.377, and 0.367 nm. The other peaks in the present XRD pattern can be assigned also to the monoclinic structure of $WO_3$. No peaks of impurities are observed suggesting a good quality of the films. The monoclinic phase, which is the stable phase at room temperature, has a pseudo-cubic structure with a slight distortion of the cubic $ReO_3$-type lattice. The crystal structure is characterised by tungsten atoms, surrounded by six oxygen atoms forming a distorted octahedron.

The crystallite size of the particles comprising the film was calculated using the Debye-Scherrer formula (Eq. IV-4) and the average crystallite size estimated using the FWHM's of the peaks (200), (020) and (002) is found to be in the range of 25-30 nm.
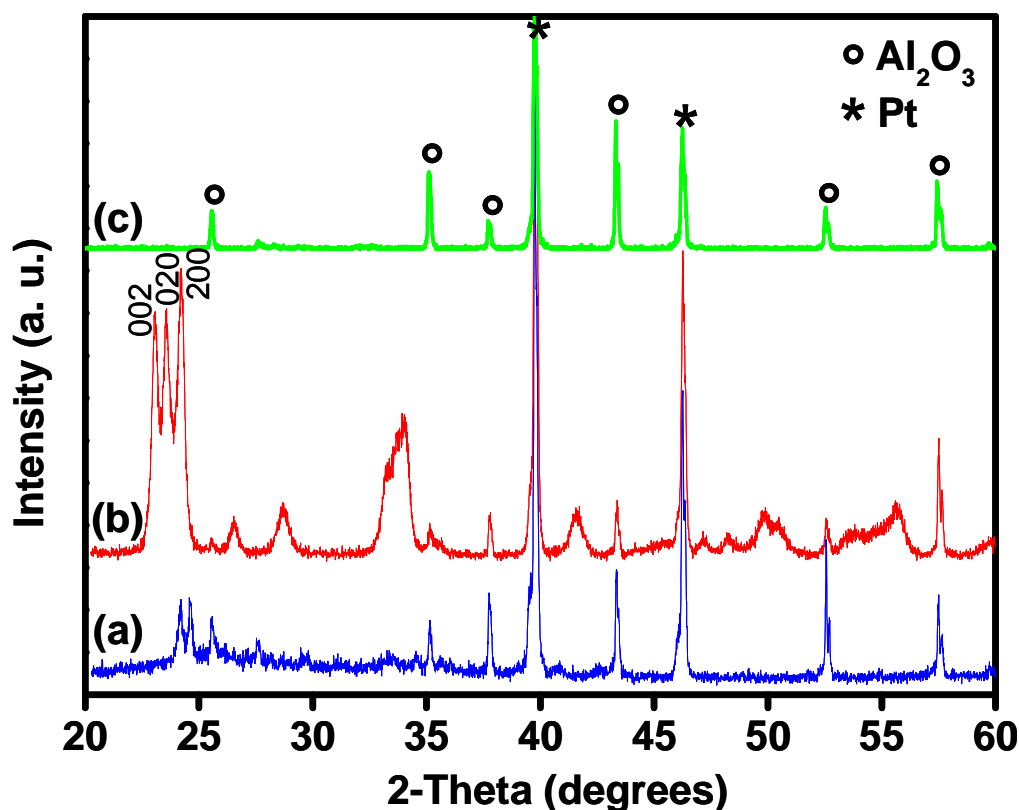


*Figure VII-6: XRD patterns of (a) WO$_3$ film as-deposited at 350 °C (1ml/h for 1h) and (b) annealed at 500 °C for 2h in air, (c) Pt-coated alumina substrate.*

It is concluded from the XRD spectra that the $WO_3$ films crystallize in the monoclinic phase, which is the most stable phase at room temperature. Furthermore, the layers are pure and they comprise crystallites with nanometer size.

### VII.2.2.3.    Transmission Electron Microscopy

Fig. VII-7 shows the TEM micrograph of the $WO_3$ grinded film deposited at 350 °C and annealed at 500 °C for 2h in air. The TEM photographs illustrate that the crystallites are in the nanometer scale, which is reasonably in agreement with the results obtained from the XRD evaluation.
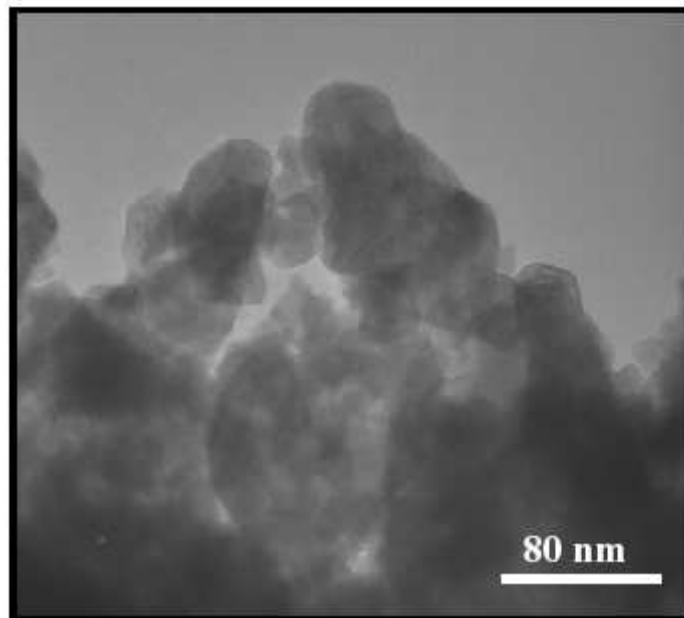


*Figure VII-7: TEM micrograph of a grinded $WO_3$ film deposited at 350 °C (1ml/h for 1h) and annealed at 500 °C for 2h in air.*

### VII.2.2.4.    Raman Spectroscopy

Fig. VII-8 shows the Raman spectra of $WO_3$ as-deposited at 350 °C (Fig. VII-8a) and annealed at 500 °C for 2h in air (Fig. VII-8b). The peak intensity of the non-annealed film is low (Fig. VII-8a) and increases after the thermal treatment (Fig. VII-8b) due to the improvement of the crystallinity and the increase of the particle size. The monoclinic phase belongs to the $P2_1/n$ ($C_{2h}^5$) space group, which has 96 modes of which 48 are Raman active. The low-frequency modes at 136 $cm^{-1}$ and 187 $cm^{-1}$ are attributed to the vibration modes of $(W_2O_2)_n$ chains [210]. The peak at 273 $cm^{-1}$ is related to the W-O-W banding mode of bridging oxide ions, while the peaks at 716 $cm^{-1}$ and 810 $cm^{-1}$ are assigned to the W-O-W stretching mode (tungsten oxide network) [212]. The longer W-O-W bonds are the source of the 716 $cm^{-1}$ peak, while the shorter W-O-W bonds are responsible for the stretching mode at 810 $cm^{-1}$.

The results are in good agreement with the literature values obtained for the monoclinic $WO_3$ phase [210,213] and also with the XRD results.
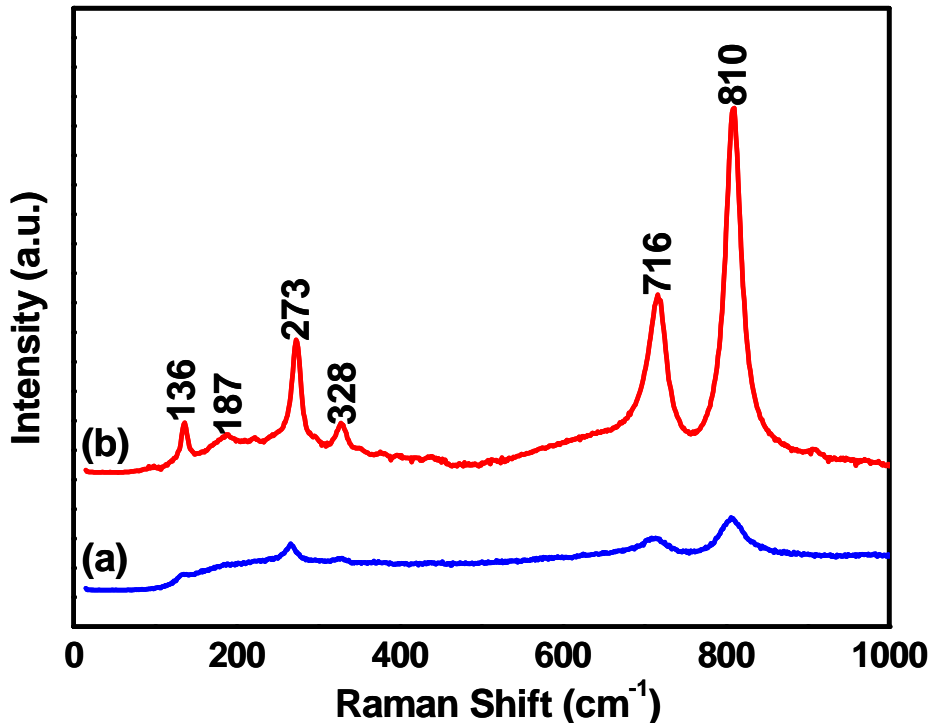


*Figure VII-8: Room-temperature Raman spectra of (a) as-deposited WO₃ film at 350 °C (1ml/h for 1h) and (b) the same film but annealed at 500 °C for 2h in air.*

## VII.2.3.  Gas sensing properties

### VII.2.3.1.  Influence of the operating temperature on the H₂S sensor response

To determine the temperature corresponding to the H$_2$S sensitivity maximum, the films were exposed to 10 ppm H$_2$S in the temperature range from 100 to 300 °C. The same gas concentration has been also chosen by other authors [198,214]. For each day of measurements the temperature was set to a constant value starting with 100 °C and increasing to 300 °C by subsequently steps of 50 °C. Before starting the measurements, the films were regenerated in synthetic air for 60 min and subsequently they were exposed to H$_2$S for 30 min. This cycle was repeated 4 or 5 times during a day and then the next temperature was set for the following day. The same procedure was used every day until the full range of temperature was explored.

The dependence of the H$_2$S sensitivity ($R_{air}/R_{H_2S}$) on the temperature is shown in Fig. VII-9. The 10 ppm H$_2$S response presents a maximum at 200 °C, when the temperature changes from 100 °C to 200 °C, the sensor sensitivity increases from 6 to 1180, which represents the maximum. Increasing the temperature beyond 200 °C, the sensitivity decreases, reaching a value of 1 at 300 °C. The same maximum temperature for H$_2$S response has been reported earlier in the literature [215].

The H$_2$S maximum response obtained using the present ESD films is higher than the response of other films prepared by other methods [214]. On contrary, Solis et al. [198] have presented a WO$_3$ sensor offering higher sensitivity than the present films, but the resistance recovery to its initial value was possible only by applying a heating pulse at 250 °C, which represents a strong inconvenience.

The detection mechanism of H$_2$S is based on the surface reaction between the adsorbed oxygen and the gas.

In a first step molecular oxygen is adsorbed on the WO$_3$ surface, thereby depleting electrons from the conduction band, and due to this fact oxygen is chemisorbed in the form of O$_2^-$ and O$^-$, depending mainly on the operating temperature, as shown by Eq. VII-1 and Eq. VII-3.

In a second step H$_2$S reacts with the different types of chemisorbed oxygen.  In this way the following reactions occur for temperatures less than 100°C:

$$O_{2(g)} \leftrightarrow O_{2(ads)}^- \qquad\qquad T< 100\ °C \qquad\qquad Eq.\ VII\text{-}1$$

$$2H_2S_{(g)} + 3O_{2(ads)}^- \leftrightarrow 2H_2O + 2SO_2 + 3e^-$$ 

<div align="right">Eq. VII-2</div>

Where (g) represents the gas phase and (ads) the adsorbed species. Due to the interaction of $H_2S$ with adsorbed oxygen ($O_2^-$), the electrons are released into the conduction band according to Eq. VII-2, improving the sensitivity. It can be seen that besides electron formation, water and sulphur dioxides are also formed.

For temperatures between 100 and 300 °C the detection mechanism of $H_2S$ can be explained using the next reactions (Eq. VII-3 and VII-4):

$$O_{2(ads)}^- + e^- \leftrightarrow 2O_{(ads)}^- \qquad\qquad T = 100 \text{ -}300 \text{ °C}$$

<div align="right">Eq. VII-3</div>

$$H_2S_{(ads)} + O_{(ads)}^- \leftrightarrow H_2O + S + e^-$$

<div align="right">Eq.VII-4</div>

We can see that electrons are formed besides water and sulphur.

As suggested in the literature [214] another mechanism, which can play a role in the detection of $H_2S$, is the reaction of $H_2S$ with the lattice oxygen from $WO_3$ (Eq. VII-5). This reaction leads to the formation of additional surface oxygen vacancies.

$$3WO_3 + 7H_2S \rightarrow 3WS_2 + SO_2 + 7H_2O$$

<div align="right">Eq. VII-5</div>

The reduction of $W^{6+}$ to $W^{4+}$ takes place on the film surface and the oxygen is released from the surface, introducing electrons in the conduction band and enhancing in this way the sensitivity.

Because the film presents the maximum sensitivity at 200 °C it can be assumed that the detection mechanism presented in Eq. VII-3 and Eq. VII-4 is the predominant one.

Considering the obtained results, the optimum operating temperature has been selected to be 200°C and this temperature was used to further study the sensor response as a function of the concentration and also to evaluate the $H_2S$ cross-sensitivity to other gases, i.e., $SO_2$ and $NO_2$.
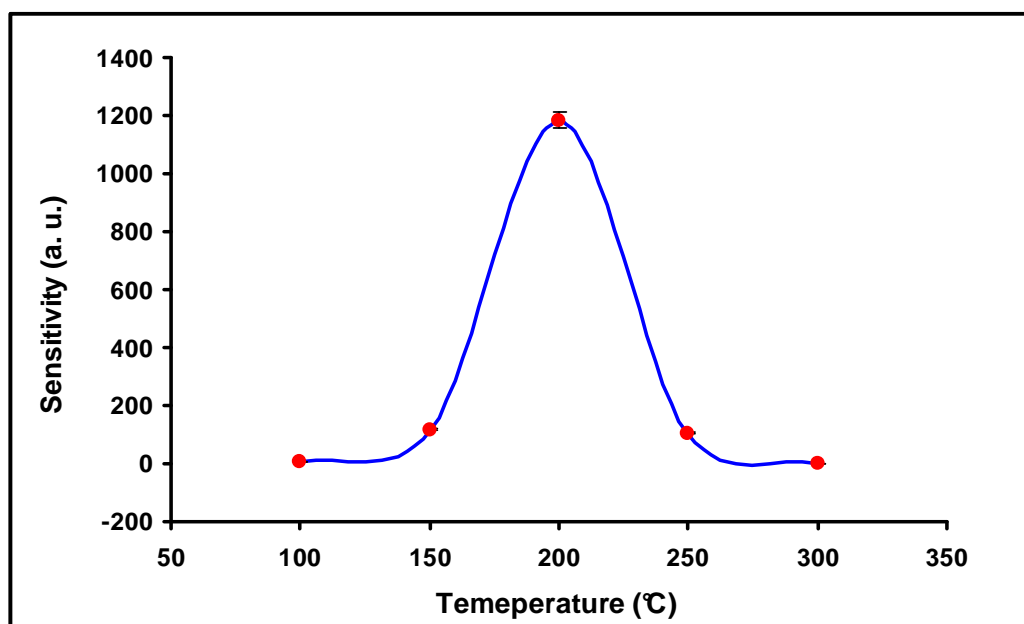
*Figure VII-9: WO$_3$ sensitivity to 10 ppm H$_2$S  as a function of the operating temperature.*

At 200 °C, after gas removal, the regeneration of the film resistance is complete and the sensitivity is showing the same value after each exposure cycle, which means that the response is reproducible.

### VII.2.3.2.    Influence of the gas concentration on the H$_2$S sensor response

The response of WO$_3$ films to different concentrations of H$_2$S (1,4,7,10 ppm) has been studied. During a day the films were exposed a few times to 1 ppm H$_2$S, followed by regeneration with synthetic air. This procedure was repeated daily until the full concentration range was studied.

The relation between the gas sensor response and the gas concentration was evaluated at 200°C by varying the concentration between 1 and 10 ppm H$_2$S (Fig. VII-10). Two behaviour regions can be distinguished: in the first one (between 1 and 7 ppm) the sensitivity increases slowly from 6 to 283, while between 7 and 10 ppm H$_2$S the sensitivity increases much faster, i.e., from 283 to 1180.
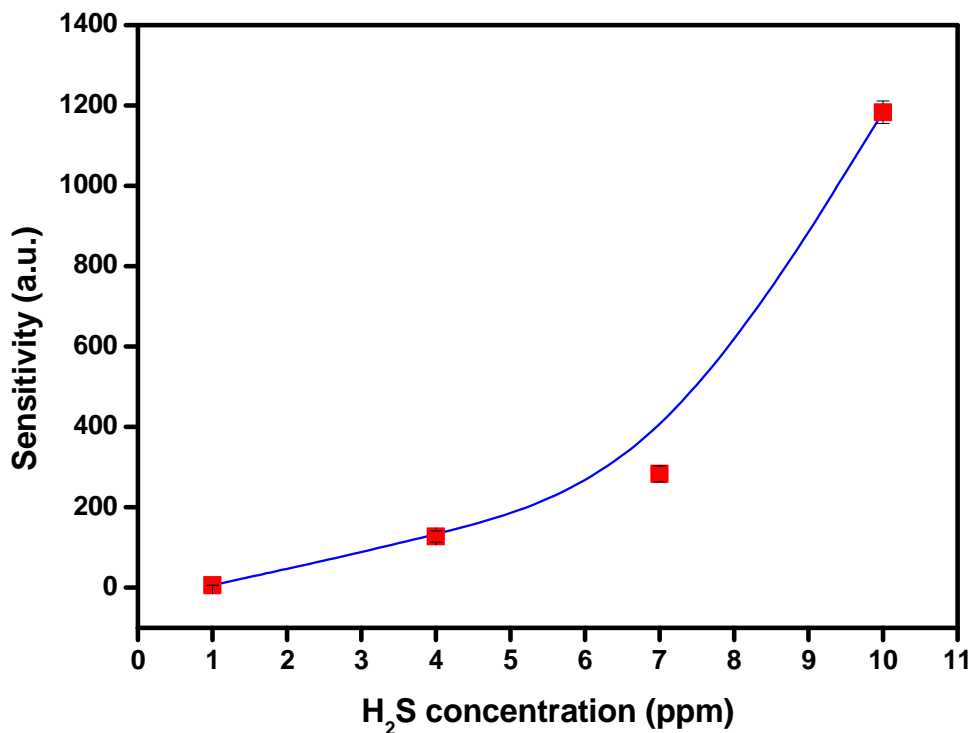
*Figure VII-10: WO₃ sensitivity as a function of H₂S concentration at 200 °C operating temperature.*

### VII.2.3.3.  Influence of the operating temperature of the NO₂ sensor response

The dependence of $NO_2$ sensitivity ($R_{NO_2}/R_{air}$) to the temperature is shown in Fig. VII-11.  As it can be observed, the 1 ppm $NO_2$ response presents a maximum at 150 °C, when the temperature changes from 50 °C to 150 °C, the sensor sensitivity increases from 2.8 to 29.4, which represents the maximum. Increasing the temperature beyond 150 °C the sensitivity decreases, reaching a value of 2.5 at 250 °C. The maximum $NO_2$ sensitivity presented in the literature is found between 100 and 300 °C and typically at 150 °C, as reported by Blo et al. [195].

The detection mechanism of $NO_2$ is similar to that presented for ZnO in Chapter V (Eqs. V- 5 to V-7). In addition, it is considered also that at low operating temperatures $NO_2$ gas adsorbed on the $WO_3$ surface forms nitrite type absorbents ($ONO^-$) and dissociates into nitrosyl type absorbents ($NO^-$, $NO^+$) [216]. So, the response of the sensor is related to the catalytic reaction of $WO_3$ with adsorbed $NO_2$. The release of electrons from the surface increases the film sensitivity.

The important parameters, which influence the sensor properties, can be connected with its morphology and microstructure. The porous structure enhances the adsorption of the gas molecules so improving the sensitivity. The particle size plays also a very important role in the sensitivity enhancement, i.e., when the particle size decreases the sensitivity increases.
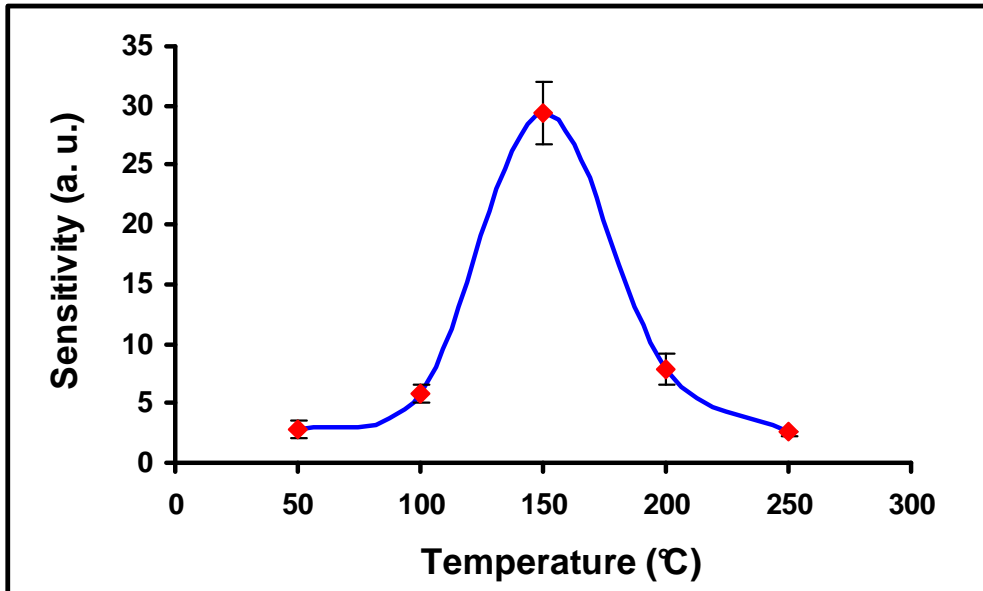


*Figure VII-11: WO$_3$ sensitivity to 1 ppm NO$_2$ as a function of the operating temperature.*

The optimum temperature of 150 °C has been selected to further study the influence of the concentration.

### VII.2.3.4.    Influence of the gas concentration on the NO$_2$ sensor response

The relation between the gas sensor response and the gas concentration was evaluated at 150 °C by varying the concentration between 0.25 and 1 ppm NO$_2$ (Fig. VII-12). It is observed that the sensitivity increases linearly from 5 to 29.4 by changing the gas concentration from 0.25 to 1 ppm NO$_2$.

The NO$_2$ response of WO$_3$ films prepared by the ESD technique is much higher at a lower operating temperature, compared with other films deposited by different techniques. For example, Kawasaki et al. [217] prepared WO$_3$ thin films using Pulsed Laser Deposition technique and the maximum sensitivity reported was 17 for 200 ppm NO$_2$ at 300°C. Also,

thermally evaporated $WO_3$ revealed a sensitivity of 3.3 for 10 ppm $NO_2$ at 300 °C [116]. The disadvantage of the present $WO_3$ sensor in the detection of $NO_2$ is the strong interference with $H_2S$. At the same temperature (150 °C) the films show a higher sensitivity for $H_2S$ than for $NO_2$ (Fig. VII-9). Usually, other authors have not studied the $NO_2$ interference with $H_2S$, the $WO_3$ films being mainly employed for the detection of $NO_2$ without precautions about the $H_2S$ presence.
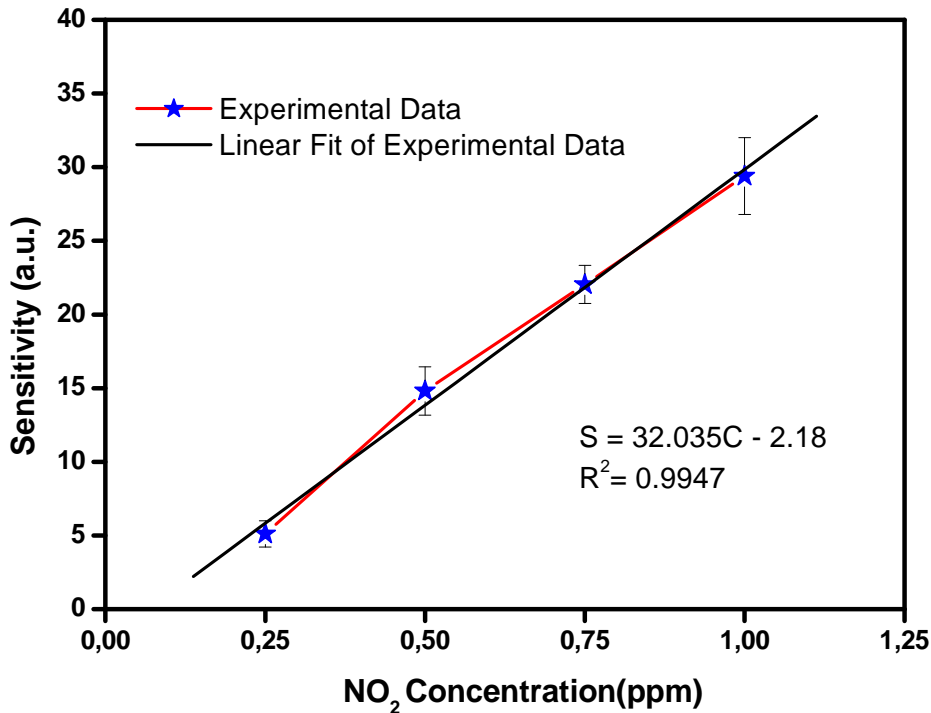


*Figure VII-12: WO₃ sensitivity as a function of NO₂ concentration at 150 °C operating temperature.*

### VII.2.3.5.   H₂S gas sensor cross-sensitivity to SO₂ and NO₂

Considering that in the atmosphere, there are many pollutant gases, the possibility of detecting a target gas is of great interest. For this reason, the $H_2S$ cross-sensitivity to $SO_2$ and $NO_2$ at 200 °C (temperature at which the $H_2S$ sensitivity is maximum) has been studied.

In Fig. VII-13 the sensitivity of $WO_3$ films at 200 °C to 10 ppm $H_2S$ (1183) is much higher than the sensitivity of 20 ppm $SO_2$ (1.91) and 1 ppm $NO_2$ (7.8), which proves that there is no cross-sensitivity of $H_2S$ with the other two gases. It can be also predicted that the present

WO$_3$ films can be selective in the detection of H$_2$S from a mixture comprising these three gases.
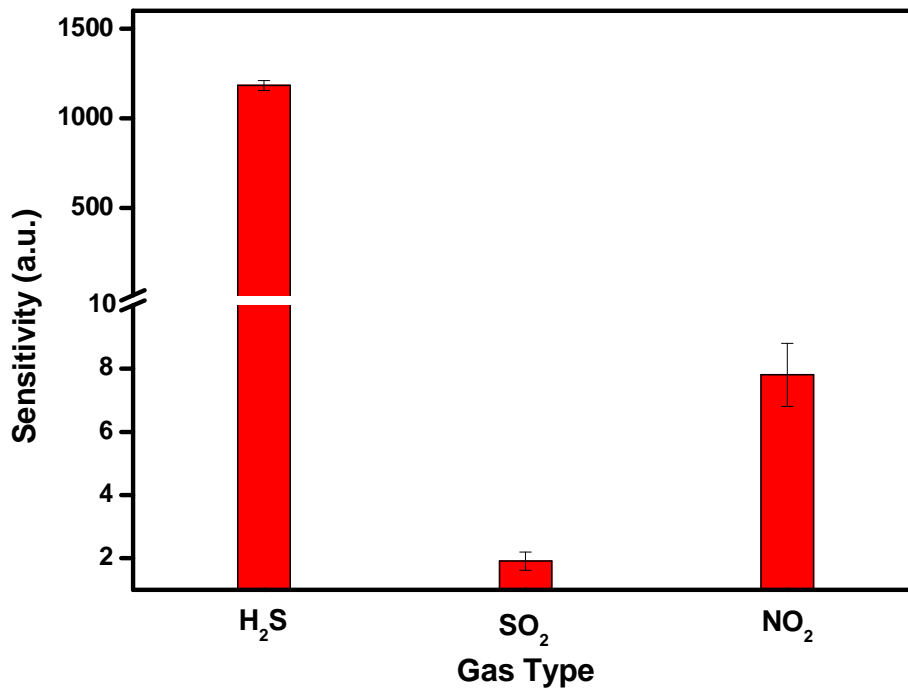


*Figure VII-13: WO$_3$ sensitivity to 10 ppm H$_2$S, 20 ppm SO$_2$ and 1 ppm NO$_2$ at 200 •C operating temperature.*

All the gas-sensing measurements have been repeated several times in order to ensure reproducibility. Furthermore, the average measurement error estimation has a minimum of 1.5 % and a maximum of about 7 %.

## VII.3. CONCLUSIONS

In this chapter the optimisation of $WO_3$ film deposition using the ESD technique is presented. Several employed precursors were used for the deposition of the films. The most suited one (tungsten ethoxide) has been selected in order to obtain pure, good quality $WO_3$ films. The SEM studies revealed that when varying the deposition temperature, different film morphologies ranging from dense to porous could be obtained. Suitable conditions for porous and adherent films have been selected for gas sensing applications. The XRD, EDX and the Raman methods revealed that the $WO_3$ films crystallized in the monoclinic phase, and that no impurities were detected, while the TEM photographs revealed the nanometer size of the grains.

Comparing the three gas responses, the films proved to have the highest sensitivity for low concentrations (10 ppm) of $H_2S$ at low operating temperature (200 °C). Moreover, the layers do not present any cross-sensitivity to 20 ppm $SO_2$ and 1 ppm $NO_2$.

The layers detect also very small quantities of $NO_2$ (less than 1 ppm) at lower operating temperature (150 °C). The results obtained are better than other results presented in the literature for a $NO_2$, sensor but unfortunately the sensors present an unpleasant interference of the $NO_2$ response with that of $H_2S$.

In this chapter it is demonstrated that the advanced deposition technique, Electrostatic Spray Deposition, can be used for the deposition of porous $WO_3$ films which are highly sensitive to $H_2S$ at low operating temperature with no cross-sensitivity to $SO_2$ and $NO_2$. Furthermore, the films are able to detect a very low concentration of $NO_2$ at lower operating temperature.

# GENERAL CONCLUSIONS

- 165 -
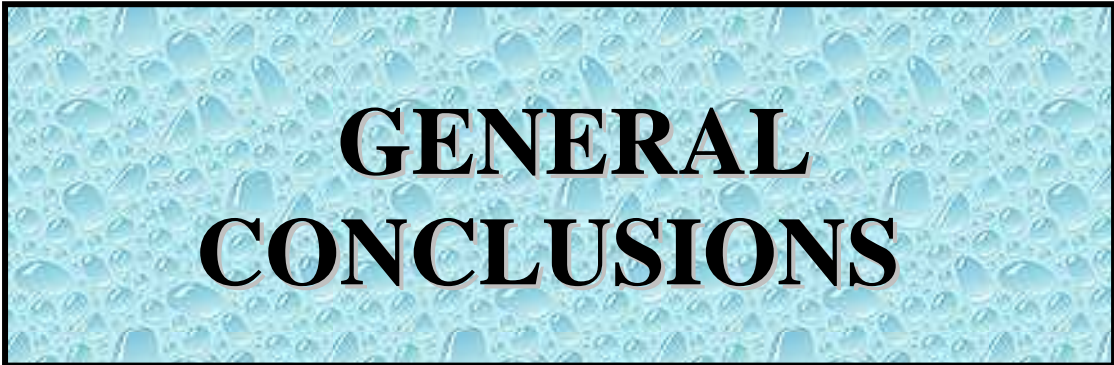
# GENERAL CONCLUSIONS

The aim of this work was to deposit and to characterize thin films of metal oxide semiconductors (tin oxide, zinc oxide, indium oxide and tungsten oxide) and to study their performances in the detection of three atmospheric pollutant gases: $H_2S$, $SO_2$ (reducing gases), and $NO_2$ (oxidizing gas).

The principal pollutants present in the atmosphere along with their negative impacts to the environment and health we have been described. Actually, to detect these pollutant gases, heavy, expensive, and time consuming systems exist. As an alternative, semiconductor metal oxide gas sensors have been fabricated and employed, which are small, simple, cheap, and present good performances for the gas detection.

Considering the literature several types of sensing materials have been selected in accordance with their affinity to detect at least one of the studied gases. Taking into account that the sensor response to a target gas can be improved by doping with a small amount of dopants, copper oxide have been selected to dope $SnO_2$ films and tin oxide to dope $In_2O_3$ films in order to improve their sensitivities to $H_2S$, respectively, to $NO_2$.

The first part of this work was dedicated to the deposition process of the films using a novel, innovative, cost-effective technique, i.e., Electrostatic Spray Deposition and also to characterize their morphology and microstucture with different techniques.

The film preparation has been optimised by varying the deposition parameters, such as temperature, time and flow rate. It has been observed that the temperature is the factor which mostly influences the film morphology allowing the deposition of dense to fractal-like porous films. The deposition time influences the layer thickness, porosity, and coverage of the substrate, while the flow rate of the precursor solution has a direct impact on the particle size.

The SEM morphological analysis permitted to select the deposition parameters necessary to obtain porous, adherent, homogeneous films suitable for gas detection.

The microstructure, evaluated with XRD and Raman Spectroscopy, revealed that the tin oxide films crystallize in the tetragonal rutile structure. Furthermore, no copper phase is formed due to the doping process, hence, no important microstructure modification has been

detected. The zinc oxide films crystallize in the hexagonal wurtzite phase and the tungsten trioxide layers in the monoclinic structure. In addition, the indium oxide films adopt the cubic phase and the doping with tin oxide has a small influence on the microstructure with a small decrease in the grain size. Moreover, it has been noted that there were no second phases detected in the deposited layers. All the samples crystallised in the adequate structure, mainly cited in the literature for sensor applications.

The above-mentioned characterization techniques permitted us to calculate the film crystallite sizes, which were found for all the doped and undoped oxides to be in the nanometer range, results in good agreement with the TEM evaluation.

The studies performed with the EDX method confirmed the film composition along with their good purity.

We can conclude from this first part that we have successfully deposited semiconductor oxide films with the desired morphology and microstructure suitable for gas sensing applications, even if some of them ($WO_3$ and $In_2O_3$) were for the first time deposited using the ESD method and required an intensive study.

In the second part of this thesis the film responses to $H_2S$, $SO_2$ and $NO_2$ was studied.

We have first evaluated the film responses to $H_2S$ in function of the operating temperature, and the maximum response obtained for $SnO_2$ was placed at 100 °C, for ZnO at 450 °C and for $WO_3$, $In_2O_3$ at 200 °C, which is in good agreement with the literature. Except ZnO films, all the layers present low temperature $H_2S$ detection which is an advantage in particular to reduce the sensor energy consumption. Between the studied films the 1 at. % Cu-doped $SnO_2$ is the most sensitive to $H_2S$, followed by $WO_3$, $In_2O_3$ and ZnO. This result validates the selection of the copper dopant in order to obtain a specific sensor able to detect $H_2S$ with a very high sensitivity.

After the selection of the optimum operating temperature the film responses in function of the concentration was studied. We have generally observed that the sensitivity improves when the gas concentration increases, except for $In_2O_3$ films, which present for $H_2S$ detection an opposite behaviour beyond 7 ppm. This phenomenon can be due to the saturation of the films and perhaps to the desorption of the gas molecules.

In addition, the evaluation of the $H_2S$ cross-sensitivity to $SO_2$ and $NO_2$ (at the optimum operating temperature) shows that all the films do not present interference with these two gases, their $H_2S$ response being higher than the $SO_2$ and $NO_2$ ones.

Secondly, the film affinity to the detection of $SO_2$ has been studied and it is found that all the films are not sensitive to this gas, showing a negligible response. The present results explain why there are only few papers related in the literature to metallic oxides devoted to the detection of $SO_2$.

Then the film responses to $NO_2$ are presented. All the films are able to detect this gas but the highest sensitivity is achieved by the $WO_3$ films, which are able to detect very low concentration of $NO_2$ (less than 1 ppm) at low operating temperature (150 °C). Unfortunately, the sensors present an interference with a $H_2S$ response and must be employed with careful selected conditions. The sensitivity of $In_2O_3$ films to $NO_2$ is improved by doping with tin oxide, confirming the choice in this study, but like for $WO_3$, $SnO_2$, and Cu-doped $SnO_2$ films, the interference with $H_2S$ response does not prevent the employment for a specific detection of $NO_2$ in a complex atmosphere. The ZnO films are the only ones which present higher $NO_2$ sensitivity than for $H_2S$ and $SO_2$ (at 300 °C), even if its $NO_2$ response is inferior to the $WO_3$ one.

In this work it has been shown that a simple and cost-effective technique can be used successfully to deposit nano-porous, homogeneous, pure, thin films of metal oxide semiconductors for gas sensing applications. It has also been proved that the selection of the present materials allowed to fabricate sensors, which can specifically detect low concentrations of $H_2S$ and $NO_2$, respectively, with no cross-sensitivity with the other studied gases. Moreover, the detection temperature was lower than for the other reported sensors, allowing energy consumption reduction.

Based on the present results summarized in Table 1, it can be proposed the realization of a miniaturized sensor array fabricated using the ESD technique and comprising 1 at. % Cu-doped $SnO_2$ (100 °C), $WO_3$ (200 °C), ZnO (450 °C) principally devoted for $H_2S$ detection, and $WO_3$ (150 °C), ZnO (300°C) for $NO_2$ detection. Even if any sensor exhibits a cross-sensitivity, the differences in the sensor gas responses exploited by an appropriate learning phase, can lead to a selective detection and quantification of an $H_2S/NO_2$ mixture.

| Films | Deposition Parameters | | | Fabrication Process | Operating Temperature | $H_2S$ Response | $NO_2$ Response | $SO_2$ Response | Reproducibillity |
|---|---|---|---|---|---|---|---|---|---|
| | T (°C) | F. R. (ml/h) | t (h) | | (°C) | 10 ppm | 1 ppm | 20 ppm | |
| $SnO_2$ | | | | | | 6.2 | 1.0 | 1 | |
| 1% Cu-$SnO_2$ | 400 | 2 | 1 | Very easy | | **2540** | 9.7 | 1 | Good |
| 2% Cu-$SnO_2$ | | | | Cheap | 100 | 750 | 1.2 | 1 | |
| 4% Cu-$SnO_2$ | | | | | | 135 | 3 | 1 | |
| ZnO | 400 | 2 | 2 | Very easy | 300 | 1.3 | 1.8 | 1 | Good |
| | | | | Cheap | 450 | 1.8 | 1.3 | - | |
| $In_2O_3$ | 400 | 1.5 | 1 | Easy | | 175 | 1.4 | 1.1 | Not Good |
| Sn-$In_2O_3$ | | | | Expensive | 200 | 8.3 | 2.0 | 1.6 | |
| $WO_3$ | 350 | 1 | 1 | Difficult | 150 | 200 | **30** | - | Good |
| | | | | Expensive | 200 | 1200 | 8 | **2** | |

*Table 1: Summarized results concerning the deposition and the gas sensing performances of the films.*

# BIBLIOGRAPHIC REFERENCES
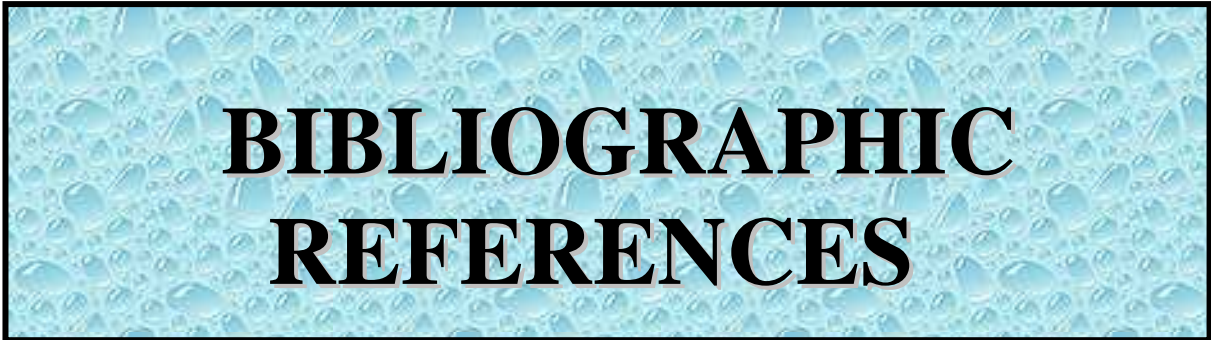
**Bibliographic references**

# BIBLIOGRAPHIC REFERENCES

[1] DO J.-S., SHIEH R.-Y., Electrochemical nitrogen dioxide gas sensor based on solid polymeric electrolyte. Sensors and Actuators B: Chemical, 1996, vol. 37, p. 19-26.

[2] HOHERÁKOVÁ Z., OPEKAR F., Au/PVC composite-a new material for solid-state gas sensors: Detection of nitrogen dioxide in the air. Sensors and Actuators B: Chemical, 2004, vol. 97, p. 379-386.

[3] HORRILLO M. C., FERNÁNDEZ M. J., FONTECHA J. L. et al., Optimization of SAW sensors with a structure $ZnO-SiO_2-Si$ to detect volatile organic compounds. Sensors and Actuators B: Chemical, 2006, vol. 118, p. 356-361.

[4] IONESCU R., HOEL A., GRANQVIST C. G. et al., Low-level detection of ethanol and $H_2S$ with temperature-modulated $WO_3$ nanoparticle gas sensors. Sensors and Actuators B: Chemical, 2005, vol. 104, p. 132-139.

[5] TANIGUCHI I., VAN LANDSCHOOT R. C., SCHOONMAN J., Fabrication of $La_{1-x}Sr_xCo_{1-y}Fe_yO_3$ thin films by electrostatic spray deposition. Solid State Ionics, 2003, vol. 156, p. 1-13.

[6] CHEN C. H., KELDER E. M., SCHOONMAN J., Unique porous $LiCoO_2$ thin layers prepared by electrostatic spray deposition. Journal Material Science, 1996, vol. 31, p. 5437-5442.

[7] LIDE D. R., Handbook of Chemistry and Physics. Crc Press Llc; 77 edition; 1997.

[8] DARA S. S., Textbook of Environmental Chemistry and its Pollution Control. Second Edition ed. Chad & Co. Ldt., New Delhi; 1997.

[9] Air Pollution at street level in European cities, European Environmental Agency (EEA), Copenhagen, ISBN 92-9167-815-5. 2007.

[10] Air pollution by ozone in Europe in Summer 2006, European Environmental Agency (EEA), Copenhagen, ISBN 978-92-9167-922-5. 2007.

[11] Analysis of greenhouse gas emissions trends and projections in Europe 2003, European Environmental Agency (EEA), Copenhagen, ISBN 92-9167-696-9. 2004.

[12] http://epa.gov/air/urbanair/. 2006.

[13] WANG Y., YAN H., WANG E., Solid polymer electrolyte-based hydrogen sulfide sensor. Sensors and Actuators B: Chemical, 2002, vol. 87, p. 115-121.

[14] KROLL A. V., SMORCHKOV V. I., NAZARENKO A. Y., Electrochemical sensors for hydrogen and hydrogen sulfide determination. Sensors and Actuators B: Chemical, 1994, vol. 21, p. 97-100.

[15] TAO W. H., TSAI C. H., $H_2S$ sensing properties of noble metal doped $WO_3$ thin film sensors fabricated by micromashining. Sensors and Actuators B: Chemical, 2002, vol. 81, p. 237-247.

[16] Air quality guidelines for Europe, World Health Organization (WHO) Regional Publications, ISBN 92-890-1358-3. 2000.

[17] European Environment Outlook, European Environmental Agency (EEA), Copenhagen, ISBN 92-9167-769-8. 2005.

[18] The European Environment, European Environmental Agency (EEA), Copenhagen, ISBN 92-9167-776-0. 2005.

[19] Emissions of acidifying substances (CSI 001), European Environment Agency (EEA), Copenhagen. 2006.

[20] STETTER J. R., PENROSE W. R., YAO S., Sensors, Chemical Sensors, Electrochemical Sensors, and ECS. Journal of the Electrochemical Society, 2003, vol. 150, p. S11-S16.

[21] STETTER J. R., PENROSE W. R., Understanding chemical sensors and chemical sensors arrays (electronic noses): past, present and future. Sensors Update, 2002, vol. 10, p. 189-229.

[22] SIMON I., BARSAN N., BAUER M. et al., Micromachined metal oxide gas sensors: opportunities to improve sensor performance. Sensors and Actuators B: Chemical, 2001, vol. 73, p. 1-26.

[23] YAMAZOE N., Towards innovation of gas sensor technology. Sensors and Actuators B: Chemical, 2005, vol. 108, p. 2-14.

[24] BRATTAIN J. B. W. H., Surface properties of germanium. Bell System Technical Journal, 1952, vol. 32, p. 1.

[25] SEIYAMA T., KATO A., FUJUSHI K. et al., A new detector for gaseous components using semiconductor thin film. Analytical Chemistry, 1962, vol. 32, p. 1502-1503.

[26] Taguchi, N. Japanese Patent. [S45-38200]. 1962.

[27] KOROTCENKOV G., Gas response control through structural and chemical modification of metal oxide films: state of the art and approaches. Sensors and Actuators B: Chemical, 2005, vol. 107, p. 209-232.

[28] WATSON J., IHOKURA K., COLES G. S. V., The tin dioxide gas sensor. Measurement Science and Technology, 1993, vol. 4, p. 711-719.

[29] WILLIAMS G., COLES G. S. V., $NO_x$ response of tin dioxide based gas sensors. Sensors and Actuators B: Chemical, 1993, vol. 15-16, p. 349-353.

[30] IVANOVSKAYA M., BOGDANOV P., FAGLIA G. et al., The features of thin films and ceramic sensors at the detection of CO and $NO_2$. Sensors and Actuators B: Chemical, 2000, vol. 68, p. 344-350.

[31] SAFONOVA O. V., DELABOUGLISE G., CHENEVIER B. et al., CO and $NO_2$ gas sensitivity of nanocristalline tin dioxide thin films doped with Pd, Ru and Rh. Materials Science and Engineering C, 2002, vol. 21, p. 105-11.

[32] STEFFES H., IMAWAN C., SOLZBACHER F. et al., Fabrication parameters and $NO_2$ sensitivity of reactively RF-sputtered $In_2O_3$ thin films. Sensors and Actuators B: Chemical, 2000, vol. 68, p. 249-253.

[33] MORRISON S. R., Selectivity in semiconductor gas sensors. Sensors and Actuators B: Chemical, 1987, vol. 12, p. 425-440.

[34] IVANOVSKAYA M., KOTSIKAU D., FAGLIA G. et al., Gas-sensitive properties of thin films heterojunction structures based on $Fe_2O_3$-$In_2O_3$ nanocomposites. Sensors and Actuators B: Chemical, 2003, vol. 93, p. 422-430.

[35] VASILIEV R. B., RUMYANTSEVA M. N., PODGUZOVA S. E. et al., Effect of interdiffusion on electrical and gas sensor properties of $CuO\backslash SnO_2$ heterostructure . Materials Science and Engineering B, 1999, vol. 57, p. 241-246.

[36] YUANDA W., MAOSONG T., XIUULI H. et al., Thin films sensors of $SnO_2$-CuO-$SnO_2$ sandwich structure to $H_2S$. Sensors and Actuators B: Chemical, 2001, vol. 79, p. 187-191.

[37] ZHAO Y., FENG Z.-C., LIANG Y., Pulsed laser deposition of $WO_3$-base film for $NO_2$ gas sensor application. Sensors and Actuators B: Chemical, 2002, vol. 66, p. 171-173.

[38] RUIZ A., DEZANNEAU G., ARBIOL J. et al., Study of the influence of Nb content and sintering temperature on $TiO_2$ sensing films. Thin Solid Films, 2003, vol. 436, p. 90-94.

[39] LALAUZE R., LE THIESSE J. C., PIJOLAT C. et al., SnO2 gas sensor. Effect of $SO_2$ treatment on the electrical properties of $SnO_2$. Solid State Ionics, 1984, vol. 12, p. 453-457.

## Bibliographic references

[40] ARSHAK K., GAIDAN I., Development of a novel gas sensor based on oxide thick films. Materials Science and Engineering B, 2005, vol. 118, p. 44-49.

[41] CHAABOUNI F., ABAAB M., REZIG B., Metrological characteristics of ZNO oxygen sensor at room temperature. Sensors and Actuators B: Chemical, 2004, vol. 100, p. 200-204.

[42] YU-DE W., ZHAN-XIAN C., YANG-FENG L. et al., Electrical and gas-sensing properties of $WO_3$ semiconductor material. Solid State Electronics, 2001, vol. 45, p. 639-644.

[43] YAMAZOE N., FUCHIGAMI J., KISHIKAWA M. et al., Interactions of tin oxide surface with $O_2$, $H_2O$ and $H_2$. Surface Science, 1979, vol. 86, p. 335-344.

[44] YAMAZOE N., KUROKAWA Y., SEIYAMA T., Effects of additives on semiconductor gas sensor. Sensors and Actuators, 1983, vol. 4, p. 283-289.

[45] HEILING A., BARSAN N., WEIMER V. et al., Gas identification by modulating temperatures of $SnO_2$-based thick film sensors. Sensors and Actuators B: Chemical, 1997, vol. 43, p. 45-51.

[46] TAKADA T., FUKUNAGA T., MAEKAWA T., New method for gas identification using a single semiconductor sensor. Sensors and Actuators B: Chemical, 2000, vol. 66, p. 22-24.

[47] XU C., TAMAKI J., MIURA N. et al., Grain size effects on gas sensitivity of porous $SnO_2$-based elements. Sensors and Actuators B: Chemical, 1991, vol. 3, p. 147-155.

[48] CARBOT A., ARBIOL J., MORANTE J. R. et al., Analysis of the nobel metal catalytic additives introduced by impregnation of as obtained $SnO_2$ sol-gel nanocrystals for gas sensor. Sensors and Actuators B: Chemical, 2000, vol. 70, p. 87-100.

[49] BARSAN N., KOZIEJ D., WEIMAR U., Metal oxide-based gas sensor research: How to? Sensors and Actuators B: Chemical, 2006, vol. 121, p. 18-35.

[50] RELLA R., SERRA A., SICILIANO P. et al., Tin oxide-based gas sensor prepared by the sol-gel process. Sensors and Actuators B: Chemical, 1997, vol. 44, p. 462-467.

[51] PARK S.-S., HACKENZI J. D., Thickness and microstructure effects on alchol sensing of tin oxide thin films. Thin Solid Films, 1996, vol. 274, p. 154-159.

[52] LANTTO V., RANTALA T. T., RANTALA T. S., Atomistic understanding of semiconductor gas sensors. Journal of the European Ceramic Society, 2001, vol. 21, p. 1961-1965.

[53] Finklea HO. Semiconductors Electrodes. In: Elsevier, ed. Amsterdam: 1988:224-226.

[54] LEGORE L. J., LAD R. J., MOULZOLF S. C. et al., Defect and morphology of tungsten trioxide thin films. Thin Solid Films, 2002, vol. 406, p. 79-86.

[55] GERAND B., NOWOGROCKI G., GUENOT J. et al., Structural study of a new hexagonal form of tungsten trioxide. Journal of Solid State Chemistry, 1979, vol. 29, p. 429-434.

[56] SIEDLE A., WOOD T. E., BROSTROM M. L. et al., Solid state polymerization of molecular metal oxide clusters: aluminium 12-tungstophosphate. Journal American Chemistry Society, 1989, vol. 111, p. 1665-1669.

[57] BALAZSI CS., FARKAS-JAHNKE M., KOTSIS I. et al., The observation of cubic tungsten trioxide at high-temperature dehydratation of tungstinc acid hydrate. Solid State Ionics, 2001, vol. 141-142, p. 411-416.

[58] VOGT T., WOODWARD P. M., HUNTER B. A., The high-temperature phases of $WO_3$. Journal of Solid State Chemistry, 1999, vol. 144, p. 209-215.

[59] KEHL W. L., HAY R. G., WAHL D., The structure of tetragonal tungsten trioxide. Journal of Applied Physics, 1952, vol. 23, p. 212-215.

[60] SALJE E., The orthorhombic phase of $WO_3$. Acta Crystallographica, 1977, vol. B 33, p. 574-577.

[61] WOODWARD P. M., SLEIGHT A. W., VOGT T., Structure refinement of triclinic tungsten trioxide. Journal of Physics and Chemistry of Solids, 1995, vol. 56, p. 1305-1315.

[62] LOOPSTRA B. O., RIETVELD H., Further refinement of the structure of $WO_3$. Acta Crystallographica, 1969, vol. B 25, p. 1420-1421.

[63] DIEHL R., BRANDT G., SALJE E., The crystal structure of triclinic $WO_3$. Acta Crystallographica, 1978, vol. B 34, p. 1105-1111.

[64] YE Z. Z., LU J.-G., CHEN H.-H. et al., Preparation and characteristics of p-type ZnO films by DC reactive magnetron sputtering. Journal of Crystal Growth, 2003, vol. 253, p. 258-264.

[65] WANG Z. L., Zinc oxide nanostructures: growth, properties and applications. Journal of Physics: Condensed Matter, 2004, vol. 16, p. R829-R858.

[66] JAFFE E., HESS A. C., Hartree-Fock study of phase changes in ZnO at high pressure. Physical Review B, 1993, vol. 48, p. 7903-7909.

[67] KARZEL H., POTZEL W., KOFFERLEIN M. et al., Lattice dynamics and hyperfine interactions in ZnO and ZnSe at high external pressures. Physical Review B, 1996, 11425-11438.

**Bibliographic references**

[68]  SHANNON R. D., New high pressure phases having the corundum structure. Solid State Communications, 1966, vol. 4, p. 629-630.

[69]  YU D., YU S.-H., ZHANG S. et al., Metastable Hexagonal $In_2O_3$ nanofibres templated from InOOH nanofibres under ambient pressure. Advanced Functional Materials, 2003, vol. 13, p. 497-501.

[70]  ERRICOA L. A., RENTERIA M., BIBILONIB A. G. et al., Electric-field gradients at 181Ta impurity sites, in $Ho_2O_3$ and $Eu_2O_3$ bixbyites. Physica B, 2007, vol. 389, p. 124-129.

[71]  CHEN C. H., BUYSMAN A. A. J., KELDER E. M. et al., Fabrication of $LiCoO_2$ thin film cathodes for rechargeable lithium battery by electrostatic spray pyrolysis. Solid State Ionics, 1995, vol. 80, p. 1-4.

[72]  CHEN C. H., KELDER E. M., SCHOONMAN J., Electrode and solid electrolyte thin films for secondary lithium-ion batteries. Journal of Power Sources, 1997, vol. 68, p. 377-388.

[73]  WILHELM O., PRATSINIS S. E., PEREDNIS D. et al., Electrospray and pressurized spray deposition of yttria-stabilized zirconia films. Thin Solid Films, 2005, vol. 497, p. 121-129.

[74]  TANIGUCHI I., VAN LANDSCHOOT R. C., SCHOONMAN J., Electrostatic spray deposition of $Gd_{0.1}Ce_{0.9}O_{1.95}$ and $La_{0.9}Sr_{0.1}Ga_{0.8}Mg_{0.2}O_{2.87}$ thin films. Solid State Ionics, 2003, vol. 160, p. 271-279.

[75]  LU J., CHU J., HUANG W. et al., Microstructure and electrical properties of $Pb(Zr, Ti)O_3$ thick film prepared by electrostatic spray deposition. Sensors and Actuators A: Phyisical, 2003, vol. 185, p. 2-6.

[76]  NOMURA M., MEESTER B., SCHOONMAN J. et al., Preparation of thin porous titania films on stainless steel substrates for heat exchange (HEX) reactors. Separation and Purification Technology, 2003, vol. 32, p. 387-395.

[77]  KIM S. G., KIM J. Y., KIM H. J., Deposition of MgO thin films by modified electrostatic spray pyrolysis method. Thin Solid Films, 2000, vol. 376, p. 110-114.

[78]  GOURAI H., LUMBRERAS M., VAN LANDSCHOOT R. C. et al., Elaboration and characterization of $SnO_2$-$Mn_2O_3$ thin layers prepared by electrostatic spray deposition. Sensors and Actuators B: Chemical, 1998, vol. 47, p. 189-190.

[79]  MATEI GHIMBEU C., VAN LANDSCHOOT R., SCHOONMAN J. et al., Preparation and characterization of $SnO_2$ and Cu-doped $SnO_2$ thin films using

electrostatic spray deposition (ESD). Journal of the European Ceramic Society, 2007, vol. 27, p. 207-213.

[80] LEEUWENBURGH S. C. G., WOLKE J. C. G., SCHOONMAN J. et al., Deposition of calcium phosphate coatings with defined chemical properties using the electrostatic spray deposition technique. Journal of the European Ceramic Society, 2006, vol. 26, p. 487-493.

[81] AVSEENKO N. V., MOROZOVA T. Y., ATAULLAKHANOV F. I. et al., Immobilization of Proteins in Immunochemical Microarrays Fabricated by Electrospray Deposition. Analytical Chemistry, 2001, vol. 73, p. 6047-6052.

[82] BUCHKO C. J., CHEN L. I., SHEN Y. et al., Processing and microstructural characterization of porous biocompatible protein polymer thin films. Polymer, 1999, vol. 40, p. 7397-7407.

[83] CHEN C. H., Thin-Film Components for Lithium-Ion Batteries. PhD thesis, ISBN 90-5651-059-2, Delft University of Technology, The Netherlands, 1998.

[84] Hartman, R. Electrohydrodynamic atomization in the cone-jet mode. PhD Thesis, Delft University of Technology, The Netherlands, 1-5. 1998.

[85] JAWOREK A., KRUPA A., Classifications of the modes of EHD spraying. Journal of Aerosol Science, 1999, vol. 30, p. 873-893.

[86] CHI D. H., BINH L. T. T., BINH N. T. et al., Band-edge photoluminescence in nanocrystalline ZnO:In films prepared by electrostatic spray deposition. Applied Surface Science, 2006, vol. 252, p. 2770-2775.

[87] CLOUPEAU M., PRUNET-FOCH B., Electrostatic spraying of liquids: Main functioning modes. Journal of Electrostatics, 1990, vol. 25, p. 165-184.

[88] SCHOONMAN J., Nanostructured materials in solid state ionics. Solid State Ionics, 2000, vol. 135, p. 5-19.

[89] OZKAN E., LEE S.-H., LIU P. et al., Electrochromic and optical properties of mesoporous tungsten oxide films. Solid State Ionics, 2002, vol. 149, p. 139-146.

[90] BAKER A. P., HODGSON S. N. B., EDIRISINGHE M. J., Production of tungsten oxide coatings, via sol-gel processing of tungsten anion solutions. Surface and Coatings Technology, 2002, vol. 153, p. 184-193.

[91] ZAYIM E. O., LIU P., LEE S.-H. et al., Mesoporous sol-gel $WO_3$ thin films via poly(styrene-co-allyl-alcohol) copolymer templates. Solid State Ionics, 2003, vol. 165, p. 65-72.

[92] NISHIO K., TSUCHIYA T., Electrochromic thin films prepared by sol-gel process. Solar Energy Materials and Solar Cells, 2001, vol. 68, p. 279-293.

[93] AMELINCKS S., VAN DYCK D., VAN LANDUYT J., VAN TENDELOO G. Electron Microscopy: Principles and Fundamentals. VCH. Weinheim, 1997.

[94] TUNSTALL D. P., PATOU S., LIU R. S. et al., Size effects in the NMR of $SnO_2$ powders. Materials Research Bulletin, 1999, vol. 34, p. 1513-1520.

[95] PARK N.-G., KANG M. G., RYU S. et al., Photovoltaic Characteristics of Dye-Sensitized surface-modified nanocrystalline $SnO_2$ solar cells. Journal of Photochemistry and Photobiology A: Chemistry, 2004, vol. 161, p. 105-110.

[96] YADAVA Y. P., DENICOLÓ D., ARIAS A. C. et al., Preparation and Characterization of transparent conducting thin oxide thin film electrodes by chemical vapour deposition from reactive thermal evaporation of $SnCl_2$. Materials Chemistry and Physics, 1997, vol. 48, p. 263-267.

[97] CHI L.-L., CHOU J. K., CHUNG W.-Y. et al., Study on extended gate field effect transistor with tin oxide sensing membrane. Materials Chemistry and Physics, 2000, vol. 63, p. 19-23.

[98] CASSIA-SANTOS M. R., SOUSA V. C., OLIVEIR M. M. et al., Recent research developments in $SnO_2$ based varistors. Materials Chemistry and Physics, 2005, vol. 90, p. 1-9.

[99] BECK K., KUNZELMANN T., VON SCHICKFUS M. et al., Contactless surface acoustic wave gas sensor. Sensors and Actuators B: Chemical, 1999, vol. 76, p. 103-106.

[100] HONG H. S., KIM J. W., JUNG S. J. et al., Suppression of NO and $SO_2$ cross-sensitivity in electrochemical $CO_2$ sensors with filter layers. Sensors and Actuators B: Chemical, 2007, vol. 113, p. 71-79.

[101] MATSUURA Y., TAKAHATA K., IHOKURA K., Mechanism of gas sensitivity change with time of $SnO_2$ gas sensors. Sensors and Actuators B: Chemical, 1988, vol. 14, p. 223-232.

[102] ROSENTAL A., TARRE A., GERST A. et al., Atomic-layer chemical vapor deposition of $SnO_2$ for gas sensing applications. Sensors and Actuators B: Chemical, 2001, vol. 77, p. 297-300.

[103] SANTOS J., SERRINI P., O'BEIRN B. et al., A thin film $SnO_2$ gas sensor selective to ultra-low $NO_2$ concentrations in air. Sensors and Actuators B: Chemical, 1997, vol. 43, p. 154-160.

**Bibliographic references**

[104] SUPOTHINA S., Gas sensing properties of nanocrystalline SnO$_2$ thin films prepared by liquid flow deposition. Sensors and Actuators B: Chemical, 2003, vol. 93, p. 526-530.

[105] SHUKLA S., LUDWIG L., PARRISH C. et al., Inverse-catalyst-effect observed for nanocrystalline-doped tin oxide sensor at lower operating temperatures. Sensors and Actuators B: Chemical, 2005, vol. 104, p. 223-231.

[106] TIBURCIO-SILVER A., SANCHEZ-JUAREZ A., SnO$_2$ thin films as gas sensors. Materials Science and Engineering B, 2004, vol. 110, p. 268-271.

[107] TAMAKI J., MAEKAWA T., MIURA N. et al., CuO-SnO$_2$ element for highly sensitive and selective detection of H2S. Sensors and Actuators B: Chemical, 1992, vol. 9, p. 197-203.

[108] NIRANJAN R. S., PATIL K. R., SAINKAR R. S. et al., High H$_2$S-sensitive copper-doped tin oxide thin film. Materials Chemistry and Physics, 2002, vol. 80, p. 250-256.

[109] VASILIEV R. B., RUMYANTSEVA M. N., YAKOVLEV N. V. et al., CuO/SnO$_2$ thin film heterostructures as chemical sensors to H$_2$S. Sensors and Actuators B: Chemical, 1998, vol. 50, p. 186-193.

[110] KOROTCENKOV G., BRINZARI V., SCHWANK J. et al., Peculiarities of SnO$_2$ thin film deposition by spray pyrolysis for gas sensor application. Sensors and Actuators B: Chemical, 2001, vol. 77, p. 244-252.

[111] COBIANU C., SAVANIU C., SICILIANO P. et al., SnO$_2$ sol-gel derived thin films for integrated gas sensors. Sensors and Actuators B: Chemical, 2001, vol. 77, p. 496-500.

[112] RELLA R., SICILIANO P., CAPONE S. et al., Air quality monitoring by means of sol-gel integrated tin oxide thin films. Sensors and Actuators B: Chemical, 1999, vol. 58, p. 283-288.

[113] LARCIPRETE R., BORSELLA E., DE PADOVA P. et al., Organotin films deposited by laser-induced CVD as active layers in chemical gas sensors. Thin Solid Films, 1998, vol. 323, p. 291-295.

[114] SBERVEGLIERI G., FAGLIA G., GROPPELLI S. et al., Methods for the preparation of NO, NO$_2$ and H$_2$ sensors based on tin oxide thin films, grown by means of the r.f. magnetron sputtering technique. Sensors and Actuators B: Chemical, 1992, vol. 8, p. 79-88.

**Bibliographic references**

[115] DOLBEC R., EL KHAKANI M. A., SERVENTI A. M. et al., Influence of the nanostructural characteristics on the gas sensing properties of pulsed laser deposited tin oxide thin films. Sensors and Actuators B: Chemical, 2003, vol. 93, p. 566-571.

[116] LEE D.-S., KIM Y. T., HUH J.-S. et al., Fabrication and characteristics of $SnO_2$ gas sensor array for volatile organic compounds recognition. Thin Solid Films, 2002, vol. 416, p. 271-278.

[117] RUMYANTSEVA M., LABEAU M., DELABOUGLISE G. et al., Copper and nickel doping effect on interaction of $SnO_2$ films with $H_2S$. Journal of Materials Chemistry, 1997, vol. 7(9), p. 1785-1790.

[118] RUMYANTSEVA M. N., LABEAU M., SENATEUR J. P. et al., Influence of copper on sensor properties of tin dioxide films in $H_2S$. Materials Science and Engineering B, 1996, vol. 41, p. 228-234.

[119] CHEN C. H., KELDER E. M., JAK M. J. G. et al., Electrostatic spray deposition of thin layers of cathode materials for lithium battery. Solid State Ionics, 1996, vol. 86-88, p. 1301-1306.

[120] YU K. N., XIONG Y., LIU Y. et al., Microstructural change of nano-$SnO_2$ grain assemblages with the annealing temperature. Physical Review B, 1997, vol. 55, p. 2666-2671.

[121] ABELLO L., BOCHU B., GASKOV A. et al., Structural characterization of nanocrystalline $SnO_2$ by X-ray and Raman Spectroscopy. Journal of Solid State Chemistry, 1998, vol. 135, p. 78-85.

[122] SUN S. H., MENG G. W., ZHANG G. X. et al., Raman scattering study of rutile $SnO_2$ nanobelts synthesized by thermal evaporation of Sn powders. Chemical Physics Letters, 2003, vol. 376, p. 103-107.

[123] LIU Y., ZHENG C., WANG W. et al., Synthesis and characterization of rutile $SnO_2$ nanorods. Advanced Materials, 2001, vol. 13, p. 1883-1887.

[124] CHEN D., SHEN G., TANG K. et al., Large-scale synthesis of CuO shuttle-like crystals via a convenient hydrothermal decomposition route. Journal of Crystal Growth, 2003, vol. 254, p. 225-228.

[125] YU T., ZHAO X., SHEN Z. X. et al., Investigation of individual CuO nanorods by polarized micro-Raman scattering. Journal of Crystal Growth, 2004, vol. 268, p. 590-595.

[126] PAGNIER T., BOULOVA M., GALERIE A. et al., Reactivity of SnO$_2$-CuO nanocristalline materials with H$_2$S: a coupled electrical and Raman spectroscopic study. Sensors and Actuators B: Chemical, 2000, vol. 71, p. 134-139.

[127] KONG X., LI Y., High sensitivity of CuO modified SnO$_2$ nanoribbons to H$_2$S at room temperature. Sensors and Actuators B: Chemical, 2005, vol. 105, p. 449-453.

[128] CHOWDHURI A., SHARMA P., GUPTA V. et al., H$_2$S gas sensing mechanism of SnO$_2$ films with ultrathin CuO dotted islands. Journal of Applied Physics, 2002, vol. 92, p. 2172-2180.

[129] ZHOU X. Z., Study on sensing mechanism of CuO-SnO$_2$ gas sensor. Materials Science and Engineering B, 2003, vol. 99, p. 44-47.

[130] DEVI G. S., MANORAMA S., RAO V. J., High sensitivity and selectivity of an SnO$_2$ sensor to H$_2$S at around 100 °C. Sensors and Actuators B: Chemical, 1995, vol. 28, p. 31-37.

[131] LIU J., HUANG X., YE G. et al., H$_2$S detection sensing characteristic of CuO/SnO$_2$ sensor. Sensors, 2003, vol. 3, p. 110-118.

[132] ZHANG G., LIU M., Effect of particle size and dopant on properties of SnO$_2$-based gas sensors. Sensors and Actuators B: Chemical, 2000, vol. 69, p. 144-152.

[133] SHEN W., ZHAO Y., ZHANG C., The preparation of ZnO based gas-sensing thin films by ink-jet printing method. Thin Solid Films, 2005, vol. 483, p. 382-387.

[134] BAXTER J. B., AYDIL E. S., Dye-sensitized solar cells based on semiconductor morphologies with ZnO nanowires. Solar Energy Materials and Solar Cells, 2006, vol. 90, p. 607-622.

[135] ALTAMIRANO-JUÁREZ D. C., TORRES-DELGADO G., JIMÉNEZ-SANDOVAL S. et al., Low-resistivity ZnO:F:Al transparent thin films. Solar Energy Materials and Solar Cells, 2004, vol. 82, p. 35-43.

[136] IBANGA E. J., LE LUYER C., MUGNIER J., Zinc oxide waveguide produced by thermal oxidation of chemical bath deposited zinc sulphide thin films. Materials Chemistry and Physics, 2003, vol. 80, p. 490-495.

[137] CHIOU W.-T., WU W.-Y., TING J.-M., Growth of single crystal ZnO nanowires using sputter deposition. Diamond and Related Materials, 2003, vol. 12, p. 1841-1844.

[138] HEIGHT M. J., PRATSINIS S. E., MEKASUWANDUMRONG O. et al., Ag-ZnO catalysts for UV-photodegradation of methylene blue. Applied Catalysis B: Environmental, 2006, vol. 63, p. 305-312.

# Bibliographic references

[139] SHAN F. K., SHIN B. C., JANG S. W. et al., Substrate effects of ZnO thin films prepared by PLD technique. Journal of the European Ceramic Society, 2004, vol. 24, p. 1015-1018.

[140] RYU H.-W., PARK B.-S., AKBAR S. A. et al., ZnO sol-gel derived porous film for CO gas sensing. Sensors and Actuators B: Chemical, 2003, vol. 96, p. 717-722.

[141] SBERVEGLIERI G., GROPPELLI S., NELLI P. et al., A novel method for the preparation of $NH_3$ sensors based on ZnO-In thin films. Sensors and Actuators B: Chemical, 1995, vol. 25, p. 588-590.

[142] CHAABOUNI F., ABAAB M., REZIG B., Effect of the substrate temperature on the properties of ZnO films grown by RF magnetron sputtering. Materials Science and Engineering B, 2004, vol. 109, p. 236-240.

[143] PARAGUAY D. F., MIKI-YOSHIDA M., MORALES J. et al., Influence of Al, In, Cu, Fe and Sn dopants on the response of thin film ZnO gas sensor to ethanol vapour. Thin Solid Films, 2000, vol. 373, p. 137-140.

[144] MATEI GHIMBEU C., SCHOONMAN J., LUMBRERAS M. et al., Electrostatic spray deposited zinc oxide films for gas sensor applications. Applied Surface Science, 2007, vol. 253, p. 7483-7489.

[145] CHANG J. F., KUO H. H., LEU I. C. et al., The effects of thickness and operation temperature on ZnO:Al thin film CO gas sensor. Sensors and Actuators B: Chemical, 2002, vol. 84, p. 258-264.

[146] XIANGFENG C., DONGLI J., DJURISIC A. B. et al., Gas-sensing properties of thick film based on ZnO nano-tetrapods. Chemical Physics Letters, 2005, vol. 4001, p. 426-429.

[147] DAYAN N. J., SAINKAR S. R., KAREKAR R. N. et al., Formulation and characterization of ZnO: Sb thick-film gas sensors. Thin Solid Films, 1998, vol. 325, p. 254-258.

[148] BENDER M., GAGAOUDAKIS E., DOULOUFAKIS E. et al., Production and characterization of zinc oxide thin films for room temperature ozone sensing. Thin Solid Films, 2002, vol. 418, p. 45-50.

[149] SHISHIYANU S. T., SHISHIYANU T. S., LUPAN O. I., Sensing characteristics of tin-deoped ZnO thin films as $NO_2$ gas sensors. Sensors and Actuators B: Chemical, 2005, vol. 107, p. 379-386.

# Bibliographic references

[150] WANG C., CHU X., WU M., Detection of $H_2S$ down to ppb levels at room temperature using sensors based of ZnO nanorods. Sensors and Actuators B: Chemical, 2006, vol. 113, p. 320-323.

[151] HU Y., ZHOU W., HAN Q. et al., Sensing properties of CuO-ZnO heterojunction gas sensors. Materials Science and Engineering B, 2003, vol. 99, p. 41-43.

[152] ASHKENOV N., MBENKUM B. N., BUNDESMANN C. et al., Infrared dielectric function and phonon modes of high-quality ZnO films. Journal of Applied Physics, 2003, vol. 93, p. 126-133.

[153] LU H.-Y., CHU S.-Y., CHENG S.-H., The vibrational and photoluminescence properties of one-dimensional ZnO nanowires. Journal of Crystal Growth, 2005, vol. 274, p. 506-511.

[154] UMAR A., KIM S. H., LEE Y.-S. et al., Catalyst-free large-quantity synthesis of ZnO nanorods by vapour-solid growth mechanism: Structural and optical properties. Journal of Crystal Growth, 2005, vol. 282, p. 131-136.

[155] ZENG J. N., LOW J. K., REN Z. M. et al., Effect of deposition conditions on optical and electrical properties of ZnO films prepared by pulsed laser deposition. Applied Surface Science, 2006, vol. 197-198, p. 362-367.

[156] ROY C., BYRNE S., MCGLYNN E. et al., Correlation of Raman and X-ray diffraction measurements of annealed pulsed laser deposited ZnO thin films. Thin Solid Films, 2003, vol. 436, p. 273-276.

[157] ALIM K. A., FONOBEROV V. A., BALANDIN A. A., Origin of the optical phonon frequency shifts in ZnO quantum dots. Applied Physical Letters, 2005, vol. 86, p. 1-3.

[158] COMINI E., FERRONI M., GUIDI V. et al., Nanostructured mixed oxides compounds for gas sensing applications. Sensors and Actuators B: Chemical, 2002, vol. 84, p. 26-32.

[159] SAYAGO I., GUTIERREZ J., ARES L. et al., The interaction of different oxidising agents on the doped tin oxide. Sensors and Actuators B: Chemical, 1995, vol. 24-25, p. 512-515.

[160] SICILIANO P., Preparation, Characterization and applications of thin films for gas sensors prepared by cheap chemical method. Sensors and Actuators B: Chemical, 2000, vol. 70, p. 153-164.

[161] XU J., WANG X., SHEN J., Hydrothermal synthesis of $In_2O_3$ for detecting $H_2S$ in air. Sensors and Actuators B: Chemical, 2006, vol. 115, p. 642-646.

[162] HARA K., SAYAMA K., ARAKAWA H., Semiconductor-sensitized solar cells based on nanocrystalline $In_2S_3/In_2O_3$ thin films electrodes. Solar Energy Materials and Solar Cells, 2000, vol. 62, p. 441-447.

[163] SCHAFER D. E., Application of metal-organic chemical vapor deposition techniques to $CdTe/In_2O_3$: Sn thin films solar cells. Solar Cells, 1987, vol. 21, p. 454.

[164] MENG Y., YANG X. L., CHEN H. X. et al., A new transparent conductive thin film $In_2O_3$: Mo. Thin Solid Films, 2001, vol. 394, p. 218-222.

[165] SMITH J. F., ARONSON A. J., CHEN D. et al., Reactive magnetron deposition of transparent conductive films. Thin Solid Films, 1980, vol. 72, p. 469-474.

[166] GIRTAN M., FOLCHER G., Structural and optical properties of indium oxide thin films prepared by an ultrasonic spray CVD process. Surface and Coatings Technology, 2003, vol. 172, p. 242-250.

[167] TANAKA S., ESAKA T., High $NO_x$ sensitivity of oxide thin films prepared by RF sputtering. Materials Research Bulletin, 2000, vol. 35, p. 2491-2502.

[168] YEOM H. Y., POPOVICH N., CHASON E. et al., A study of the effect of process oxygen on stress evolution in d.c. magnetron-deposited tin-doped indium oxide. Thin Solid Films, 2002, vol. 411, p. 17-22.

[169] DAOUDI K., SANDU C. S., TEODORESCU V. S. et al., Rapid thermal annealing procedure for densification of sol-gel indium tin oxide thin films. Crystal Engineering, 2002, vol. 5, p. 187-193.

[170] SHUKLA S., SEAL S., LUDWIG L. et al., Nanocrystalline indium oxide-doped tin oxide thin film as low temperature hydrogen sensor. Sensors and Actuators B: Chemical, 2004, vol. 97, p. 256-265.

[171] PRINCE J. J., RAMAMURTHY S., SUBRAMANIAN B. et al., Spray pyrolysis growth and material properties of $In_2O_3$ films. Journal of Crystal Growth, 2002, vol. 240, p. 142-151.

[172] ROZATI S. M., GANJ T., Transparent conductive Sn-doped indium oxide thin films deposited by spray pyrolysis technique. Renewable Energy, 2004, vol. 29, p. 1671-1676.

[173] MATEI GHIMBEU C., SCHOONMAN J., LUMBRERAS M., Porous indium oxide films deposited by electrostatic spray deposition technique. Ceramics International, 2006.

[174] ATASHBAR M. Z., GONG B., SUN H. T. et al., Investigation on ozone-sensitive $In_2O_3$ thin films. Thin Solid Films, 1999, vol. 334, p. 222-226.

## Bibliographic references

[175] TAKADA T., SUZUKI K., NAKANE M., Highly sensitive ozone sensor. Sensors and Actuators B: Chemical, 1993, vol. 13, p. 404-407.

[176] YAMAURA H., JINKAWA T., TAMAKI J. et al., Indium oxide-based gas sensor for selective detection of CO. Sensors and Actuators B: Chemical, 1996, vol. 36, p. 325-332.

[177] EPIFANI M., CPONE S., RELLA R. et al., $In_2O_3$ thin films obtained through a chemical complexation based sol-gel process and their application as gas sensor devices. Journal of Sol-Gel Science technology, 2003, vol. 26, p. 741-744.

[178] IVANOVSKAYA M., GURLO A., BOGDANOV P., Mechanism of $O_3$ and $NO_2$ detection and selectivity of $In_2O_3$ sensors. Sensors and Actuators B, 2001, vol. 77, p. 264-267.

[179] STARKE T. K. H., COLES G. S. V., FERKEL H., High sensitivity $NO_2$ sensors for environmental monitoring produced using laser ablated nanocrystalline metal oxides. Sensors and Actuators B: Chemical, 2002, vol. 85, p. 238-245.

[180] NIU X., ZHONG H., WANG X. et al., Sensing properties of rare earth oxide doped $In_2O_3$ by sol-gel method. Sensors and Actuators B: Chemical, 2006, vol. 115, p. 434-438.

[181] FRANCIOSO L., FORLEO A., CAPONE S. et al., Nanostructured $In_2O_3$ sol-gel thin films as material for $NO_2$ detection. Sensors and Actuators B: Chemical, 2006, vol. 114, p. 646-655.

[182] CHUNG W.-Y., SAKAI G., SHIMANOE K. et al., Preparation of indium oxide thin film by spin-coating method and its gas-sensing properties. Sensors and Actuators B: Chemical, 1998, vol. 46, p. 139-145.

[183] DAOUDI K., CANUT B., BLANCHIN M. G. et al., Tin-doped indium oxide thin films deposited by sol-gel dip-coating technique. Materials Science and Engineering C, 2002, vol. 21, p. 313-317.

[184] CANTALINI C., WLODARSKI W., SUN H. T. et al., $NO_2$ response of $In_2O_3$ thin film gas sensors prepared by sol-gel and vacuum thermal evaporation techniques. Sensors and Actuators B, 2000, vol. 65, p. 101-104.

[185] DOLL T., FUCHS A., EISELE I. et al., Conductivity and work function ozone sensors based on indium oxide. Sensors and Actuators B: Chemical, 1998, vol. 49, p. 63-67.

[186] KOROTCENKOV G., BRINZARI V., CERNEAVSCHI A. et al., The influence of film structure on $In_2O_3$ gas response. Thin Solid Films, 2004, vol. 460, p. 315-323.

# Bibliographic references

[187] GURLO A., IVANOVSKAYA M., BARSAN N. et al., Grain size control in nanocrystalline $In_2O_3$ semiconductor gas sensor. Sensors and Actuators B: Chemical, 1997, vol. 44, p. 327-333.

[188] RAYLEIGH L. F., On instability of jets. Proc London Math Soc, 1878, vol. 11, p. 4-13.

[189] CHEN C. H., KELDER E. M., VAN DER PUT P. J. J. M. et al., Morphology control of thin $LiCoO_2$ films fabricated using electrostatic spray deposition (ESD) technique. Journal of Materials Chemistry, 1996, vol. 6(5), p. 765-771.

[190] CHAUDRA BOSE A., RAMAMOORTHY R., RAMASAMY S., Formability of metastable tetragonal solid solution in nanocrystalline $NiO-ZrO_2$ powders. Materials Letters, 2003, vol. 44, p. 203-207.

[191] WHITE W. B., KERAMIDAS V. G., Vibrational spectra of oxides with C-type rare earth oxide structure. Spectrochemica Acta, 1972, vol. 28A, p. 501-509.

[192] ROJAS-LOPEZ M., NIETO-NAVARRO J., ROSENDO E. et al., Raman scattering study of photoluminiscent spark-processed porous InP. Thin Solid Films, 2000, vol. 379, p. 1-6.

[193] VIGREUX C., BINET L., GOURIER D., Formation by laser impact of conducting - $Ga_2O_3$-$In_2O_3$ solid solution with composition gradients. Journal of Solid State Chemistry, 2001, vol. 157, p. 94-101.

[194] SHAVER P. J., Activated tungsten oxide gas detectors. Applied Physical Letters, 1967, vol. 11, p. 255-257.

[195] BLO M., CAROTTA M. C., GALLIERA S. et al., Synthesis of pure and loaded powders of $WO_3$ for $NO_2$ detection through thick film technology. Sensors and Actuators B: Chemical, 2004, vol. 103, p. 213-218.

[196] CHOI G.-Y., SAKAI G., SHIMANOE K. et al., Wet process-based fabrication of $WO_3$ thin film for $NO_2$ detection. Sensors and Actuators B: Chemical, 2004, vol. 101, p. 107-111.

[197] HE X., LI J., GAO X. et al., $NO_2$ sensing characteristics of $WO_3$ thin film microgas sensor. Sensors and Actuators B: Chemical, 2003, vol. 93, p. 463-467.

[198] SOLIS J. L., SAUKKO S., KISH L. B. et al., Nanocrystalline tungsten oxide thick-film with high sensitivity to $H_2S$ at room temperature. Sensors and Actuators B: Chemical, 2001, vol. 77, p. 316-321.

# Bibliographic references

[199] SHIMIZU Y., MATSUNAGA N., HYODO T. et al., Improvement of $SO_2$ sensing properties of $WO_3$ by noble metal loading. Sensors and Actuators B: Chemical, 2001, vol. 77, p. 35-40.

[200] NAKAGAWA H., YAMAMOTO N., OKAZARI S. et al., A room-temperature operated hydrogen leak sensor. Sensors and Actuators B: Chemical, 2003, vol. 93, p. 468-474.

[201] TÄGTSTRÖM P., JANSSON U., Chemical vapour deposition of epitaxial $WO_3$ films. Thin Solid Films, 1999, vol. 352, p. 107-113.

[202] PATRA A., AUDDY K., GANGULI D. et al., Sol–gel electrochromic $WO_3$ coatings on glass. Materials Letters, 2004, 1059-1063.

[203] LEMIRE C., LOLLMAN D. B. B., AL MOHAMMAD A. et al., Reactive R.F. magnetron sputtering deposition of $WO_3$ thin films. Sensors and Actuators B: Chemical, 2002, vol. 84, p. 43-4.

[204] STANKOVA M., VILANOVA X., LLOBET E. et al., Influence of the annealing and operating temperatures on the gas-sensing properties of rf. sputtered $WO_3$ thin-film sensors. Sensors and Actuators B: Chemical, 2005, vol. 105, p. 271-277.

[205] PATIL P. S., NIKAM S. B., KADAM L. D., Influence of substrate temperature on properties of sprayed $WO_3$ thin films. Materials Chemistry and Physics, 2001, vol. 69, p. 77-8.

[206] SIVAKUMAR R., MOSES EZHIL RAJ A., SUBRAMANIAN B. et al., Preparation and characterization of spray deposited n-type $WO_3$ thin films for electrochromic devices. Materials Research Bulletin, 2004, vol. 39, p. 1489.

[207] MATEI GHIMBEU C., VAN LANDSCHOOT R. C., SCHOONMAN J. et al., Tungsten trioxide thin films prepared by electrostatic spray deposition technique. Thin Solid Films, 2007, vol. 515, p. 5498-5504.

[208] MATEI GHIMBEU C., VAN LANDSCHOOT R. C., SCHOONMAN J. et al., Electrostatic spray deposition of tungsten oxide. International conference on materials science and engineering, Brasov-Romania, ISBN: 973-635-454-7, 2005.

[209] OKAMOTO H., YAMANAKA K., KUDO T., Protonic conduction and electrochromism of amorphous peroxopolytungstic acid. Material Research Bulletin, 1986, vol. 21, p. 551-557.

[210] PECQUENARD B., LECACHEAUX H., LIVAGE L. et al., Orthorhombic $WO_3$ formed via Ti-stabilized $WO_3 \cdot 1/3H_2O$ phase. Journal of Solid State Chemistry, 1998, vol. 135, p. 159-168.

# Bibliographic references

[211] MOULZOLF S. C., LEGORE L. J., LAD R. J., Heteroepitaxial growth of tungsten oxide films on sapphire for chemical gas sensors. Thin Solid Films, 2001, vol. 400, p. 56-63.

[212] HABAZAKI H., HAYASHI Y., KONNO H., Characterization of electrodeposited WO3 films and its application to electrochemical wastewater treatment. Electrochemica Acta, 2002, vol. 47, p. 4181-4188.

[213] BOULOVA M., LUCAZEAU G., Crystallite nanosize effect on the structural transitions of $WO_3$ studied by Raman Spectroscopy. Journal of Solid State Chemistry, 2002, vol. 167, p. 425-434.

[214] REYES L. F., HOEL A., SAUKKO S. et al., Gas sensor response of pure and activated $WO_3$ nanoparticle films made by advanced reactive gas deposition. Sensors and Actuators B: Chemical, 2006, vol. 117, p. 128-134.

[215] BARRET E. P. S., GEORGIADES G. C., SERMON P. A., The mechanism of operation of $WO_3$-based $H_2S$ sensors. Sensors and Actuators, 1990, vol. B1, p. 116-120.

[216] ARAI H., TOMINAGA H., An infrared study of nitric oxide adsorbed on rhodium-alumina catalyst. Journal of Catalysis, 1976, vol. 43, p. 131-142.

[217] KAWASAKI H., UEDA T., SUDA Y. et al., Properties of metal doped tungsten oxide thin films for $NO_x$ gas sensors grown by PLD method combined with sputtering process. Sensors and Actuators B: Chemical, 2004, vol. 100, p. 266-26.

**Preparation and Characterization of Metal Oxide Semiconductor Thin Films for the detection of pollutant atmospheric gases**

The demand of simple, small, low cost and performing gas sensors for the detection of pollutant gases is of great interest taking into consideration the health and environmental problems. For this purpose we decided to develop thin films of metal oxide semiconductors which present a good affinity to many pollutant gases, but which, however, present a problem of cross-sensitivity and, additionally, which must work at elevated temperatures. These thin films ($SnO_2$, Cu-doped $SnO_2$, $WO_3$, $In_2O_3$, Sn-doped $In_2O_3$ and ZnO) have been deposited on partially-Pt coated alumina using a novel innovative technique, i.e., Electrostatic Spray Deposition allowing easy deposition parameter (temperature, flow rate, time, etc.) variations. Homogeneous, nanostructured films with desired porous morphology have been obtained as revealed by Scanning Electron Microscopy and Transmission Electron Microscopy techniques. The microstructure studied using Energy Dispersive X-ray Analysis, X-ray Diffraction, respectively, Raman spectroscopy methods showed that we have successfully obtained the desired crystallinity and a good purity of the films for gas sensor use. The sensing performance of the films to different oxidizing and reducing pollutant gases ($H_2S$, $SO_2$, and $NO_2$) has been yet evaluated. From all the studied films, the 1% Cu-doped $SnO_2$ ones prove to be the most sensitive for the detection of $H_2S$ at low operating temperatures and furthermore present no cross-sensitivity for the two other gases. $WO_3$ films present the highest sensitivity to $NO_2$ at 150°C compared with all the other oxide films, but unfortunately the $NO_2$ response interferes with the $H_2S$ response. To avoid this ambiguity, we can use ZnO films, which present a very high sensitivity to $NO_2$ compared to $SO_2$ and $H_2S$ response. Additionally, all the films were almost insensitive to $SO_2$. On the base of these results we can propose the concept of a competitive miniaturized sensor array dedicated to detect and to quantify a $H_2S/NO_2$ mixture.

*Key words:* Gas Sensors, Electrostatic Spray Deposition, Thin films, Pollution, $H_2S$, $NO_2$, $SO_2$.

**Préparation et caractérisation de couches minces d'oxydes métalliques pour la détection de gaz polluants atmosphériques**

La demande de capteurs de gaz performants simples, petits, et de faible coût est d'un grand intérêt si l'on prend en considération les problèmes de santé et d'environnement. C'est pourquoi nous avons décidé de développer la fabrication de couches minces d'oxydes métalliques semiconducteurs, qui présentent une bonne affinité vis-à-vis de beaucoup de gaz polluants, mais qui, cependant, présentent un problème de sensibilité croisée et, qui, aussi, doivent fonctionner à températures élevées. Ces couches minces ($SnO_2$, $SnO_2$ dopé cuivre, $WO_3$, $In_2O_3$, $In_2O_3$ dopé étain, ZnO) ont été déposées sur des plaquettes d'alumine recouvertes partiellement de platine à l'aide d'une nouvelle technique de dépôt: le Spray Electrostatique assisté par pyrolyse, qui permet une grande flexibilité des paramètres (température, temps, vitesse du débit,…..). Les Microscopies Electroniques à Balayage et à Transmission ont révélé une nanostructure homogène dont la morphologie présente la porosité désirée. Les analyses par Dispersion et Diffraction de Rayons X, ainsi que la Spectroscopie Raman ont montré que ces couches minces ont obtenu la cristallinité désirée, ainsi qu'une bonne pureté, pour l'emploi en capteurs de gaz. Nous avons alors évalué les performances des couches minces pour la détection de différents gaz polluants de nature réductrice ou oxydante: $H_2S$, $SO_2$, $NO_2$. De toutes les compositions étudiées, c'est l'oxyde d'étain dopé de 1% de cuivre (Cu-$SnO_2$) qui s'est montré le plus sensible pour la détection de $H_2S$, à basse température, sans présenter de sensibilité croisée aux deux autres gaz. Les couches minces d'oxyde de tungstène ($WO_3$) présentent la meilleure sensibilité pour $NO_2$, à 150°C, de toutes les compositions. Malheureusement, la réponse à $NO_2$ interfère avec la réponse à $H_2S$. Pour lever cette ambiguïté, on peut utiliser des couches minces d'oxyde de zinc (ZnO), qui présentent une très grande sensibilité à $NO_2$, par rapport à $SO_2$ et $H_2S$. Enfin, nous avons trouvé que toutes les compositions de couches minces étaient pratiquement insensibles à $SO_2$. Sur la base de ces résultats, nous pouvons proposer la conception d'une matrice miniaturisée de capteurs permettant de détecter et de quantifier un mélange des gaz $H_2S/NO_2$.

*Mot clés:* Capteurs de gaz, Spray électrostatique, couches minces, Pollution, $H_2S$, $NO_2$, $SO_2$.